Dust in Large Optical Surveys

Professor Douglas P. Finkbeiner Edward Ford Schlafly

Dust in Large Optical Surveys

Abstract

We present results studying the distribution and properties of the diffuse dust in the Milky Way Galaxy using large optical surveys—specifically, the Sloan Digital Sky Survey (SDSS) and the Panoramic Survey Telescope and Rapid Response System 1 (Pan-STARRS1). This work has resulted in accurate measurements of dust reddening in regions of low extinction over large regions of sky. We present maps of reddening from dust covering the footprint of the SDSS, which covers one quarter of the sky. We present preliminary maps of dust covering the Pan-STARRS1 footprint, which covers three-quarters of the sky, including most of the plane of our Galaxy.

We use these maps of dust to decisively exclude some simple parameterizations of dust extinction (Cardelli et al., 1989) in favor of others (Fitzpatrick, 1999). We show that the extinction predicted by the widely-used far-infrared dust map of Schlegel et al. (1998) is overestimated by 18%, and recalibrate that map using our extinction measurements. We further map variation in the properties of the dust, as indicated by variation in the amount of extinction relative to the amout of far-infrared dust extinction, and by variation in the ratio of dust extinction at different frequencies. We confirm these results by measuring reddening using two independent techniques and data sets, the SDSS photometry and spectroscopy.

We further present the photometric calibration of the Pan-STARRS1 data—a necessary step to studying the dust with that ongoing survey. We achieve photometric precision unprecedented in a large optical survey, accurate to better than 1%. We additionally show the suitability of the calibrated photometry for studying

the distribution of dust.

Finally, we present preliminary three-dimensional maps of the dust in the Galaxy using our calibrated data from Pan-STARRS1. These maps will provide by far the most extensive information yet achieved about the three-dimensional distribution of extinction in the Galaxy.

Contents

Citations to Previously Published Work

The content of Chapter 2, apart from minor modifications, appeared in:

Schlafly, E. F., Finkbeiner, D. P., Schlegel, D. J., et al. 2010, ApJ, 725, 1175

The content of Chapter 3, apart from minor modifications, appeared in

Schlafly, E. F., & Finkbeiner, D. P. 2011, ApJ, 737, 103

The content of Chapter 4, apart from minor modifications, appeared in:

Schlafly, E. F., Finkbeiner, D. P., Juric, M., et al. 2012, ArXiv e-prints

Listing of figures

To my parents and siblings, for putting up with me. I love you.

Acknowledgments

Many thanks to Doug, for making this a productive and successful five years. I was lucky to have you as an advisor. I am indebted to Chris Stubbs and Alyssa Goodman, for much help and guidance over the years, and for being the easiest committee to assemble that I have ever heard of. I owe much to the hard work of the many scientists contributing to the Sloan Digital Sky Survey and to Pan-STARRS1, who have made this research possible.

Thanks to all of my friends. You have made the last several years what they were. Stay in touch!

Chapter 1

Introduction

This dissertation describes my efforts to map and study dust extinction using the Sloan Digital Sky Survey and PanSTARRS-1, two wide-field optical surveys. It is divided into six chapters. In this, the first chapter, we discuss in general terms the importance of dust in astronomy, and outline the history of dust research. The following three chapters are devoted to three papers published over the last three years. Chapter 2 presents Schlafly et al. (2010), an analysis of dust using photometry from the Sloan Digital Sky Survey (York et al., 2000, SDSS). This work exploited the uniformity of the distribution of stellar colors of halo stars to attribute variation in observed stellar colors to reddening from dust. In the next chapter, Chapter 3, we present Schlafly & Finkbeiner (2011), a complementary analysis using stellar spectra from the SDSS. This work confirmed the results of our photometric analysis, using a largely independent set of data with different systematic sources of uncertainty. In Chapter 4, we present Schlafly et al. (2012), a photometric calibration of the ongoing optical survey Pan-STARRS1 (Kaiser et al., 2002). That work has not yet been used to study the dust. However, it makes high-quality photometry of three-quarters of the sky available for use in studying the dust, including most of the Galactic plane. In Chapter 5 we discuss future work using this data to map the three-dimensional

structure of the Galaxy's dust. We then conclude briefly in Chapter 6.

1.1 Introduction to Dust

Interstellar dust is solid material residing in the vast reaches of space between the stars. It is composed of heavy elements fused from hydrogen and helium as as stars burn. These heavy elements are expelled into the interstellar medium in stellar winds and in more violent eruptions and explosions. The heavy elements are reprocessed in the interstellar medium forming dust grains (Draine, 2003; Li & Greenberg, 2003).

That said, dust is in some sense more an empirical fact than a theoretical entity. The chemical composition of dust remains unknown, and considerable uncertainty exists about where dust is created and how long it survives (Draine, 2011). There are a number of features in the emission and absorption spectra of dust that remain unexplained (Draine, 2011). Nevertheless, observationally the role of dust is well established. Dust is the material responsible for absorbing and scattering light, especially optical starlight, and for reradiating that light in the far-infrared. Dust is observed in many other ways as well; however, the direct interaction of dust with light provides the most obvious and most established evidence for the dust.

This chapter first describes the importance of dust in §1.2. We then outline the history of observations of the dust in §1.3. Finally, we briefly outline the remainder of this dissertation in §1.4.

1.2 Importance

Dust derives its importance in astronomical research primarily in two ways. The first way is through its role in the physics of the Galaxy, especially in the physics of the interstellar medium and of star formation. The second way is through the effect of

dust on essentially any optical, infrared, or microwave observation. Users of these observations must account for the effects of dust. These two topics are described in §1.2.1 and §1.2.2, respectively.

1.2.1 Dust and the Galaxy

The dust is crucially important to the physics of the Galaxy. By mass, dust plays an insignificant role in the galaxy; it makes up only one percent of the mass of the Galaxy's gas, which itself makes up only a small portion of the mass of the Galaxy. Still, were dust inert, like dark matter, the Galaxy would be a very different place—the dust plays an outsize role in the physics of the Galaxy. As a solid, dust has a broad range of energy levels and can interact with light over much of a star's spectrum, whereas atomic hydrogen gas, for instance, can interact with light primarily only within a few lines for all wavelengths longward of ionizing hydrogen. Because of this, about 30% of the light leaving the Galaxy was last emitted by dust, having been earlier absorbed from stars (Li & Greenberg, 2003).

Because dust is effective at emitting and absorbing light, dust plays a major role in determining the structure of the Galaxy. Dust provides a primary source of cooling in hot gas clouds, allowing a cloud to radiate away energy that would otherwise halt its collapse. Absent dust, the time required for a gas cloud to collapse would change drastically, inhibiting star formation. In a similar way, dust heats much of the interstellar medium by absorbing starlight which would otherwise pass straight through the interstellar medium. Dust also protects molecular hydrogen from dissociation by absorbing ultraviolet radiation from stars in molecular clouds. Molecular hydrogen is also crucial to cloud cooling and collapse, and without protection from dust it would rapidly dissociate (Li & Greenberg, 2003).

The dust also controls the chemistry of the Galaxy. Molecular hydrogen in the

interstellar medium forms primarily on the surface of dust grains. Neutral hydrogen encountering a dust grain sticks to the surface of the grain, and upon encountering more hydrogen atoms there, can be shed as molecular hydrogen. Moreover, many of the elements in the interstellar medium heavier than helium are substantially "depleted" onto dust grains—that is, these elements are removed from the gas of the interstellar medium and incorporated into the grains. The dust thereby alters the elemental composition of the gas phase of the interstellar medium (Pirronello et al., 2004).

1.2.2 Dust and Observations

In addition to affecting much of the physics of the Galaxy directly, dust also affects many areas of research indirectly. Because dust absorbs and scatters light, especially at ultra-violet through near-infrared wavelengths, dust affects most observations made at those frequencies. Dust also affects observations at longer wavelengths, primarily in the mid-infrared through microwave wavelengths, through its radiation. Accordingly, many observations contain signatures from dust, and science relying on these observations must account for them.

To be concrete, one might be interested in finding the temperature of a star for which one has photometry in g and i, two bands in the optical. Hot stars are blue and have small $g - i$, while cold stars are red and have large $g - i$. This allows the temperature of the star to be inferred from its color. However, dust can also affect the g and i photometry of the star. Dust absorbs and scatters light according to the dust extinction law. Because of the small size of dust grains, dust extinguishes more blue light than red light, reddening the observed colors of stars. For this reason the dust extinction law is often referred to as a reddening law, and objects seen through dust are called "reddened." Accordingly, unless one knows the dust reddening to the

star, one cannot infer the temperature of the star from its color. Absent other information, a red star may either be cold, or hot but reddened by dust.

This sort of concern is widespread. The distances to stars and galaxies are often inferred from their colors, which are affected by dust. This can confuse studies of the structure of the Galaxy and of the Universe. Even when redshifts are measured so that distance estimates do not depend on the dust, dust can still affect studies of the distribution of galaxies. This is because dust changes the colors and brightnesses of the observed galaxies, and so can affect which galaxies are targeted for spectra and how easily redshifts are obtained for those galaxies. Supernovae studies rely on the universality of the supernova explosion, making each explosion like every other. Because in principle the amount of dust, or, worse, the properties of dust around each supernova can vary, this universality can be broken by the dust. Accordingly, understanding the dust is a major part of supernova research.

Studies of the cosmic microwave background are likewise affected by the dust. Accurate measurement of the cosmic microwave background requires separating the cosmic microwave background light from other sources of microwave light. Those other sources include thermal emission from dust and microwave emission from spinning dust grains (Draine & Lazarian, 1998). Accordingly, cosmic microwave background measurements require detailed knowledge of the distribution and emission spectrum of the dust. Satellite missions to measure the cosmic microwave background have been careful to use an increasing number of frequencies, largely to allow the dust and other foregrounds to be removed (COBE DMR: 3, WMAP: 5, Planck: 10).

The dust has wide importance throughout astronomy, whether through its direct influence on the physics of the Galaxy or through its effect on observations of other phenomena. Unsurprisingly, then, dust has a long history of observations.

1.3 History

Toward the Galactic Center, even by eye one can tell that the distribution of stars is patchy. The dark patches are areas where intervening clouds of dust extinguish the light from the stars behind. The dust, then, is not a recent discovery. We briefly here describe some of the key discoveries in the history of the dust. Because, however, the dust affects so many phenomena in the Galaxy, we mention here only a select few of the major historical discoveries about dust extinction.

William Herschel first pointed out the dark patches in the Milky Way in 1785 (Herschel, 1785), but he did not associate these patches with any kind of obscuring material, and instead attributed them to areas where there were no stars. Edward Barnard and Max Wolf suspected that these dark patches were the result of obscuring clouds (Barnard, 1919; Wolf, 1923). The evidence supporting this suspicion, however, was missing until 1930, when Robert Trumpler discovered that the dark patches were associated with reddening (Trumpler, 1930). This indicated that stars in the dark patches were obscured by small grains that simultaneously extinguished and reddened light from the stars behind.

The earliest reddening law was proposed in 1936 by Rudnick, by comparing the colors of stars whose spectra showed similar lines, but were behind different amounts of dust (Rudnick, 1936). This technique is closely related to the method we present in Chapter 3. Since then, substantially more accurate measurements of the reddening law have been made, refining that early work. The most widely used reddening law today comes from the work of Cardelli et al. (1989). That work additionally showed that the reddening law varies in different parts of the sky largely as a one parameter family described by R_V, a parameter related to the grain size distribution. Our own work shows that the reddening law of Fitzpatrick (1999) is superior, albeit only by a

few percent in extinction, though more in reddening.

The most commonly used map of dust extinction today is that of Schlegel et al. (1998, SFD), which is based on thermal dust emission. Some of the earliest estimates of the temperature of dust grains and their implied emission spectrum were made as early as 1926 by Eddington (Eddington, 1926), by assuming that grain heating by starlight balanced thermal grain emission. Full-sky maps of this dust emission could not be made, however, until satellite observations by IRAS and COBE were performed (Neugebauer et al., 1984; Boggess et al., 1992). These two sets of observations were combined by Schlegel et al. (1998) to make the SFD map, the most widely used map of dust today.

1.4 Outline

Clearly, the dust is a major component of the Galaxy, and touches a tremendous variety of research topics. This introduction only briefly mentions some highlights of the field, and this dissertation will address only a small fraction of those highlights. Here we focus primarily on observations of reddening by dust, and the relation between reddening and dust emission. Our primary goal is to provide detailed maps of the dust to allow better correction for the effects of dust on observations, and to better understand the distribution of the dust.

Chapters 2 and 3 present accurate, high-resolution maps of reddening from dust. These maps can be used to correct the observed colors of stars, so that the true colors of stars, in the absence of dust, can be inferred. In Chapter 4, we present the photometric calibration of Pan-STARRS1, an ongoing survey of the sky that we wish to use to study the dust. In Chapter 5, we present preliminary work using Pan-STARRS1 data to create three-dimensional maps of the distribution of dust and

stars in the Galaxy. We conclude in Chapter 6.

Chapter 2

Measuring Reddening with the Blue Tip of the Stellar Locus

This chapter presents Schlafly et al. (2010), which studies the two-dimensional distribution of the dust using photometry from the Sloan Digital Sky Survey. This work provides a library of high-accuracy reddening measurements, which are used to study the reddening law and to map the dust.

2.1 Introduction

Most astronomical observations are affected by Galactic interstellar dust, whether as a source of foreground light in the microwave, far-infrared and gamma-ray wavelength regions or as a cause of extinction in the infrared through ultraviolet (Draine, 2003). Characterizing the properties of the dust and accounting for its effects on observations is then a central problem in astronomy.

Dust is formed as stars burn nuclear fuel to heavy elements and emit these elements in stellar winds or in more violent eruptions, and these elements are reprocessed in the interstellar medium (Draine, 2009). The distribution of dust is correspondingly correlated with the hydrogen in the interstellar medium (ISM), though the

dust-to-gas ratio varies. Burstein & Heiles (1978, BH) took advantage of the correlation between H I and dust column density to make the first widely used map of dust column density, combining H I emission and galaxy counts.

The BH dust map was superseded by the Schlegel et al. (1998, SFD) dust map, which took advantage of the full-sky far-infrared (FIR) data provided by *IRAS* and DIRBE, which are dominated by thermal emission from the Galactic dust at wavelengths of 100 μm and longer. After correction for dust temperature using FIR color ratios, these maps trace dust column density. Calibration of dust column density to color excess $E(B-V)$ was performed using the colors of a sample of 389 galaxies with Mg_2 indices (Faber et al., 1989), which were also used to test the performance of the resulting map.

The advent of large astronomical surveys permits stronger tests of the SFD dust map and the assumptions used to construct it. We test the SFD dust map using the colors of stars from the Sloan Digital Sky Survey (SDSS) (York et al., 2000), including the recently completed SDSS-III imaging (Weinberg et al., 2007), which covers about 2000 deg^2 in the southern Galactic sky. This allows us to more tightly constrain the SFD normalization and the dust extinction spectrum, or "reddening law," over the SDSS bands, as well as to provide a map of color residuals that point to problems with the SFD dust map, and particularly with the temperature correction.

Previous tests of SFD have usually found that SFD overpredicts extinction in high-extinction regions. Shortly after its introduction, Arce & Goodman (1999) found that SFD extinction was too high by 40% in Taurus, using star counts, colors, and FIR emission. Likewise, studies using globular cluster photometry, galaxy counts, and NIR colors have found that SFD overpredicts extinction by a similar fraction in other dusty regions (Stanek, 1998; Chen et al., 1999; Yasuda et al., 2007; Rowles & Froebrich, 2009). Cambrésy et al. (2001) explore the link between the SFD

overestimation and dust temperature using star counts in the Polaris Flare. At $|b| < 40°$, Dobashi et al. (2005) use optical star counts to conclude that SFD overpredicts extinction by a factor of two or more. We perform similar tests to these in regions of lower extinction than had been previously possible, taking advantage of the high quality and depth of the SDSS stellar photometry, and complementing the recent work of Peek & Graves (2010), who use SDSS galaxy spectra. In these regions, we do not find that SFD overpredicts reddening by a large factor; rather, we find that SFD overpredicts reddening by about 14% in $B - V$, though, because of the reddening law adopted by SFD, this varies from color to color.

The colors of stars vary substantially with stellar type, and with location in the Galaxy due to the effect of metallicity on color. Nevertheless, we find that the colors of the most blue main sequence stars in old populations—the main sequence turn-off (MSTO) stars—are remarkably stable over the sky, and that we can empirically model their slow spatial variation. We therefore present measurements of the colors of the "blue tip" of the stellar locus, and use them to constrain the SFD dust map. This work is akin to that of High et al. (2009), in which the color of stellar populations is also used as a sort of color standard.

In §2.2 we describe the data sets used in this work: the SDSS imaging data and the SFD dust map. In §2.3, we present our method for measuring the blue tip of the stellar locus, and the corresponding maps of blue tip colors on the sky. In §2.4, we present fits of the SFD dust map to the blue tip colors. In §2.5 and §2.6, we discuss these results and conclude. The blue tip maps and measurements can be found at the web site `skymaps.info/bluetip`.

2.2 Data

2.2.1 The SDSS

The SDSS is a digital spectroscopic and photometric survey, that, with the additional south Galactic cap (SGC) data provided by the SDSS-III, covers just over one third of the sky, mostly at high latitudes (Abazajian et al., 2009). The SDSS provides near-simultaneous imaging in five optical filters: u, g, r, i, and z (Gunn et al., 1998; Fukugita et al., 1996). The photometric pipeline has uniformly reduced data for about 10^8 stars. The SDSS is 95% complete up to magnitudes 22.1, 22.4, 22.1, 21.2, and 20.3 in u, g, r, i, and z. The SDSS imaging is performed in a drift-scanning mode in which the shutter is left open while the telescope moves at constant angular speed across the sky. The resulting imaging "runs" tend to cover strips of sky that are long in right ascension and narrow in declination. These runs are divided into fields, which are $13.5'$ by $9'$ in size. We use SDSS data that have been photometrically calibrated according to the "ubercalibration" procedure of Padmanabhan et al. (2008).

2.2.2 The SFD Dust Map

The SFD dust map is a map of thermal emission from dust based on the *IRAS* 100 μm maps. The *IRAS* 100 μm map underwent three major processing steps before being used in the SFD dust map: it was destriped, zodiacal-light subtracted, and calibrated to match COBE/DIRBE at degree scales. The first and third of these steps were necessary because the zero point of the *IRAS* 100 μm detector varied over time, imprinting the *IRAS* scan pattern on the data in the form of stripes, and making the overall zero point of the data uncertain. The zodiacal-light subtraction is needed to remove the signature of the hot, bright, local interplanetary dust from the *IRAS* and DIRBE data, which, though bright, contributes negligibly to the reddening. The

DIRBE 100 μm to 240 μm flux ratio is used to constrain the dust temperature and to transform the 100 μm flux map to a map proportional to dust column density. The destriped *IRAS* data have resolution of 6 arcminutes, while the temperature correction is smoothed to degree scales. The destriped, temperature-corrected *IRAS* 100 μm map is normalized to a map of $E(B-V)$ by using a sample of 389 galaxies with Mg_2 indices and $B-V$ colors, for use as color standards (Faber et al., 1989).

2.3 The Blue Tip of the Stellar Locus

Main sequence stars are confined to a tight locus in color-color space, as is apparent from a typical SDSS color-color diagram, as shown in Figure 2.1. The locus has a sharp blue edge at the color of the MSTO stars, blueward of which there are only rare blue stragglers, white dwarfs, and quasars. The intrinsic color of the MSTO is set by the properties of the stellar population: primarily, metallicity and age. The observed colors of the MSTO are the intrinsic colors, altered by reddening due to dust and by systematic color shifts due to imperfect calibration of the observations. Empirically, the intrinsic color of the MSTO is slowly varying in space; the observed color of MSTO stars is therefore a good probe of the reddening due to dust.

Population effects cause the color of main sequence stars to vary as a function of the magnitude of stars probed. At faint magnitudes and high latitudes, metal-poor halo stars dominate, rendering the MSTO stars bluer than at bright magnitudes and lower latitudes, where redder disk stars dominate, as is apparent in Figure 2.2. Moreover, the shape of the blue edge changes with magnitude: owing to photometric errors, the edge is sharp for bright stars and becomes blurred at fainter magnitudes. Accordingly, the typical color of MSTO stars depends on magnitude.

Stars of similar metallicities may clump together in the halo, changing the observed

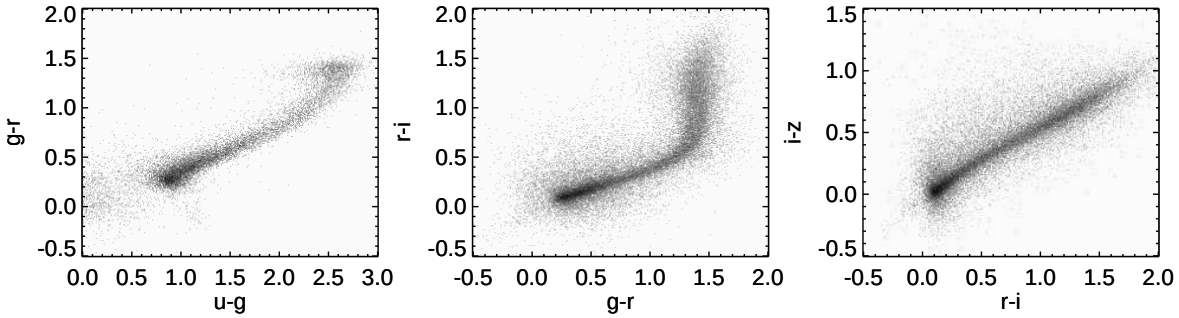

Figure 2.1 Color-color diagrams for point sources from the SDSS, within two degrees of the north Galactic pole. The sharp cutoff in stellar density blueward of the "blue tip" is prominent. In $u-g$, the points blueward of the blue tip are mostly quasars and white dwarfs. The blue tip is at about 0.8, 0.2, 0.1, and 0.0 mags in $u-g$, $g-r$, $r-i$, and $i-z$, respectively.

color of the blue tip. Because we do not have a good way to model such effects, we cannot distinguish such clumps from reddening due to dust in the blue tip maps.

2.3.1 Measuring the Blue Tip

We perform fits to the location of the blue tip of the stellar locus in each SDSS field (or group of SDSS fields). To avoid biasing the fits, we select stars in each field for analysis in a reddening-independent way, and then find the location of the blue tip in the resulting sample.

Care must be taken when imposing cuts on the stars in each field to avoid biasing the resulting blue tip color. Because extinction changes the observed magnitudes of stars, a flat cut on magnitude would bias the measurement, as the distance range probed would change with the dust column. Instead, we perform cuts on D, the g magnitude of a star projected along the reddening vector to zero color:

$$D = g - \frac{A_g}{A_g - A_r}(g - r). \tag{2.1}$$

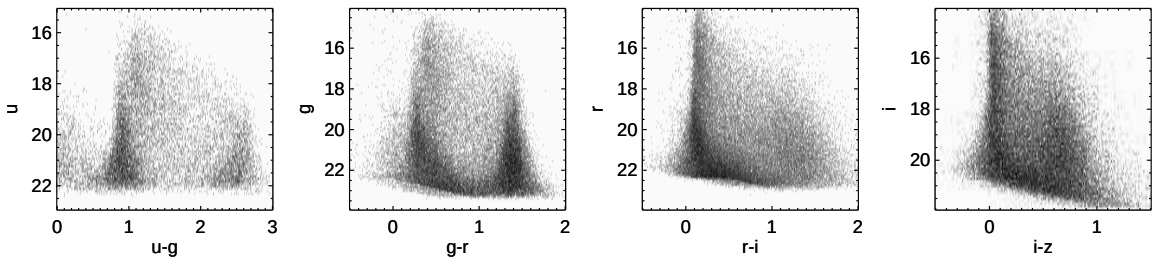

Figure 2.2 Color-magnitude diagrams from the SDSS, for the same stars as in Figure 2.1. The location of the blue edge of the stellar locus depends on magnitude, especially in the bluer bands, where bright, nearby, more metal-rich stars are redder than more distant halo stars. In $u - g$, blueward of the blue edge lie mostly quasars and white dwarfs. The location of the blue tip is as in Figure 2.1.

Provided $A_g/(A_g - A_r)$ is accurate, the set of stars in a particular range of D is independent of the dust column towards the stars. D is related to the distance modulus of the MSTO stars (though not redder stars). Using the Jurić et al. (2008) "bright" photometric parallax relation, MSTO stars with $r - i = 0.1$ and $g - r = 0.2$ have $M_g = 5.3$. Accounting for the projection from $g - r = 0.2$ to zero color along the reddening vector, $D \approx g - M_g + 4.6$. In this work, we frequently use the range $10 < D < 19$. Including the effect of saturation on the bright end, this restriction on D selects stars with distances between about 1 and 8 kpc.

With a reddening-independent population of stars in hand, we measure the color of the blue edge of these stars in each SDSS color. Figure 2.3 illustrates the process, which is described below. The stellar colors are modeled as drawn from a probability distribution $P(x)$, taken to be a step function convolved with a Gaussian to reflect the photometric uncertainty and the intrinsic width of the blue edge. The maximum-likelihood location for the step is denoted the "blue tip" of the locus. Specifically, the form of the probability distribution is taken to be

$$P = \frac{1}{2}\left[1 + \mathrm{erf}\left(\frac{x - x_0}{\sqrt{2}\sigma_P}\right)\right] + F, \tag{2.2}$$

where erf is the Gaussian error function, σ_P corresponds to the width of the edge and F sets a floor to the probability distribution, to render the fit insensitive to the occasional white dwarf or blue straggler. In this work we use $F = 0.05$. The variable x_0 is the only free parameter in the fits, and gives the color of the blue tip. The final results of this work are insensitive to substantial changes in the floor F, from 0.01 to 0.05. The formal statistical uncertainty in the blue tip color is computed for each measurement by fitting the likelihood near the maximum likelihood to a Gaussian.

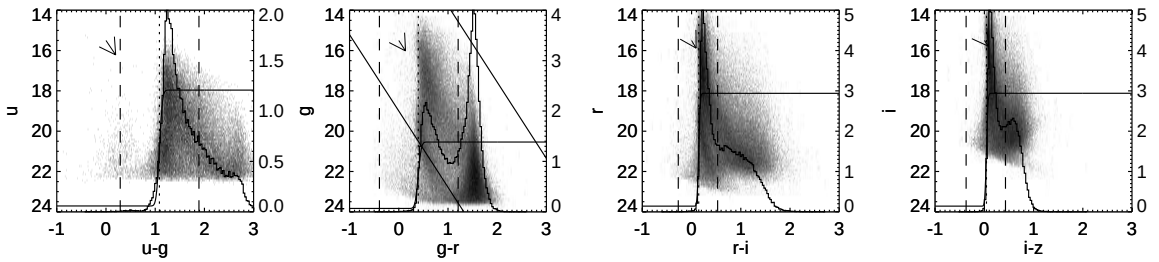

Figure 2.3 Example fits for the blue tip of the stellar locus in $u - g$, $g - r$, $r - i$, and $i - z$ for a one degree region around $l = 150°$ and $b = 20°$. A grayscale of the color-magnitude diagram is plotted, with features of the fit superimposed. The diagonal solid lines in the $g - r$ plot give the magnitude range within which stars are fitted, corresponding to $10 < D < 19$. The histograms give the distribution of stellar colors satisfying this cut. The solid error function gives the best fit to this histogram, within the gray dashed vertical lines. The black dotted vertical line gives the derived location of the blue tip. The arrow in the upper left of the diagram gives the magnitude and direction of the reddening vector in this field, according to SFD. Finally, the right hand axis gives the value of the pdf P; its integral between the outer dashed lines is unity.

The width of the blue edge is set by a combination of the intrinsic width of the edge and the typical measurement error in star colors in the SDSS. We adopt the values 0.05, 0.05, 0.025 and 0.025 for the width parameter σ_P in the colors $u - g$, $g - r$, $r - i$ and $i - z$, respectively. Because the photometric uncertainty becomes larger at faint magnitudes, at high extinctions the observed blue edge is expected to broaden. Despite this, σ_P is kept constant in the fits, introducing the possibility of bias in the measurements. Nevertheless, as we look only at relatively bright ranges of

D and low extinction, this is a minor effect. Simulations with a mock star catalog (§2.4.4) verify that for the range $10 < D < 19$ used in this work, the introduced bias in the recovered ratio of blue tip color to $E(B-V)$ is less than 2% in $u-g$ and smaller in the other colors.

The statistical uncertainty of the fit depends on the number of stars included in the fit, and so on the local stellar density, the sky area and range of D used. At high latitudes, binning together ten SDSS fields, for stars with $10 < D < 19$ mag, typical statistical uncertainties are 20, 15, 6 and 6 mmag for $u-g$, $g-r$, $r-i$, and $i-z$, respectively. Finding the standard deviations of measurements taken near the north Galactic pole, where the expected reddening is smooth and small, we find uncertainties of 24, 17, 10, and 12 mmag, similar to the fit results.

Figure 2.4 demonstrates how the presence of dust reddens stars, pushing the blue edge redward. In low-extinction regions where all of the dust is closer than about 1 kpc, the observed blue tip is uniformly shifted. It is this shift that we track in our measurements. In high-extinction regions or regions with dust beyond about 1 kpc, we can in principle learn about the change in dust column with distance by varying D, though we have not done so in this work (see §2.3.2).

The functional form $P(x, x_0)$ chosen to fit the blue edge of the distribution is usually a close fit only near the blue edge itself, and is rather bad over most of the color range. However, experiments with other functional forms and attempts to adaptively shrink the range over which the fit is performed to a narrow region around the edge tend to render the fit less robust. Moreover, because P is approximately constant away from the edge, the fit results are robust to outliers far from the edge. Alternative functional forms systematically shift the location of the edge around slightly (mmags), but not in a way that correlates with the dust.

The blue tip fit can occasionally fail to find the blue tip of the stellar locus when

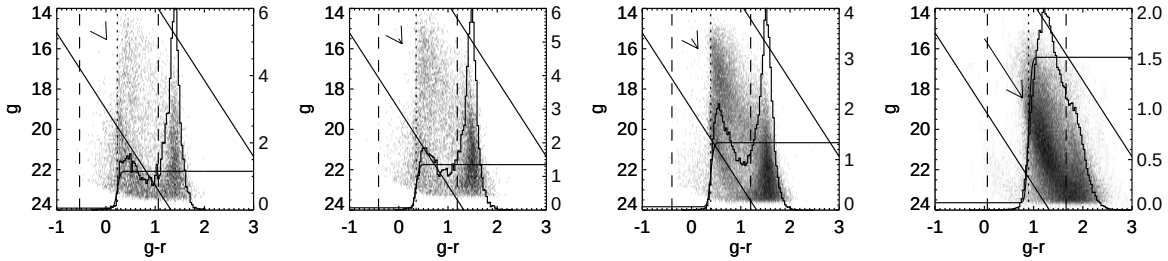

Figure 2.4 Example fits for the blue tip of the stellar locus in regions of increasing extinction, at $l = 150°$ and $b = 80°, 40°, 20°$ and $10°$, from left to right. The SFD extinction prediction is indicated by the length of the arrow in the upper left of the diagram. As we approach the plane, the stellar density increases. At $b = 10°$, the brightest stars are not behind all of the dust, and so the color of the blue tip becomes redder at fainter magnitudes.

too few stars are used. In such cases it might identify a single blue star or quasar as the blue tip, or latch on to the M-dwarf peak in color magnitude diagrams. In the maps we present, with $10 < D < 19$ and using 10 SDSS fields worth of stars for each blue tip fit, fewer than 1% of measurements are affected.

2.3.2 Changing Extinction with Distance

In this work we treat all MSTO stars observed by the SDSS with $10 < D < 19$ as behind all of the dust. In principle, however, by comparing the color of the blue tip for nearby stars and distant stars, distant clouds of dust could be detected. Such clouds certainly exist, as dust has been detected in the halos of other galaxies and in H I clouds outside the disk in our Galaxy (Ménard et al., 2010; Wakker et al., 1996). However, comparing blue tip maps made for nearby ranges of D and distant ranges of D reveal no readily identifiable structures larger than the noise in the halo. We note that if such structures vary slowly spatially, then they will be difficult to distinguish from variation in blue tip colors due to changing stellar populations. We defer to later work the attempt to identify such clouds.

On most sight lines the great majority of the dust column comes from the Galactic disk and is associated with the H I disk, which has a scale height of about 150 pc (Kalberla & Kerp, 2009). Accordingly, as the brightest unsaturated MSTO stars are approximately a kiloparsec away, at high Galactic latitudes even the nearest MSTO stars observed by the SDSS are behind this dust.

At low Galactic latitudes, extinction increases rapidly and the color of the blue tip of the stellar locus becomes dramatically redder as fainter magnitudes are probed. Figure 2.5 shows the blue tip along a particularly dusty sight line. In these dusty regions, reddened blue tip stars may be redder than intrinsically red foreground stars. Moreover, blue tip stars in these regions are spread out along the reddening vector, making it hard to isolate stars of a given reddening and distance using D. We attempt to identify and exclude such regions when analyzing blue tip maps.

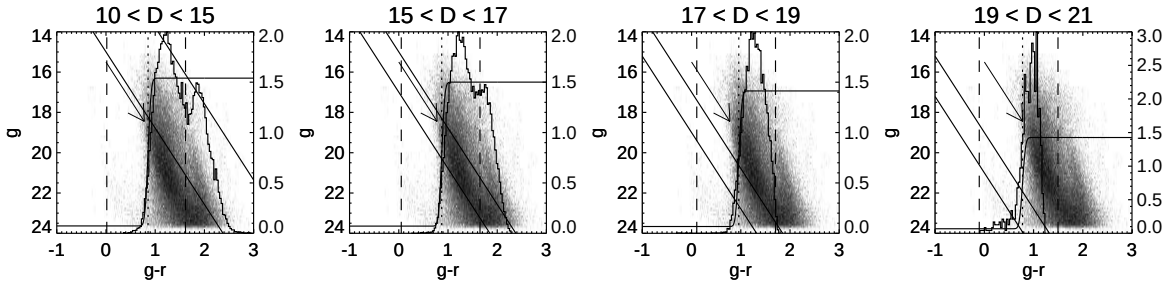

Figure 2.5 Example fits for the blue tip of the stellar locus for different magnitude ranges D at $l = 150°$ and $b = 10°$. The blue tip shifts redward as the range of D probed goes fainter, until we run out of stars. Additionally, intrinsically red foreground stars increasingly contaminate the blue tip as we go fainter in dusty regions.

2.3.3 Blue Tip Maps

We measure the blue tip color over the entire SDSS footprint, in each color and for a variety of ranges of D. Figure 2.6 shows the resulting maps of the color of the blue tip of the stellar locus. Here we present maps using blue tip fits to stars in a broad range of magnitudes: $10 < D < 19$ mag, using fits to the stars in 10 adjacent SDSS fields.

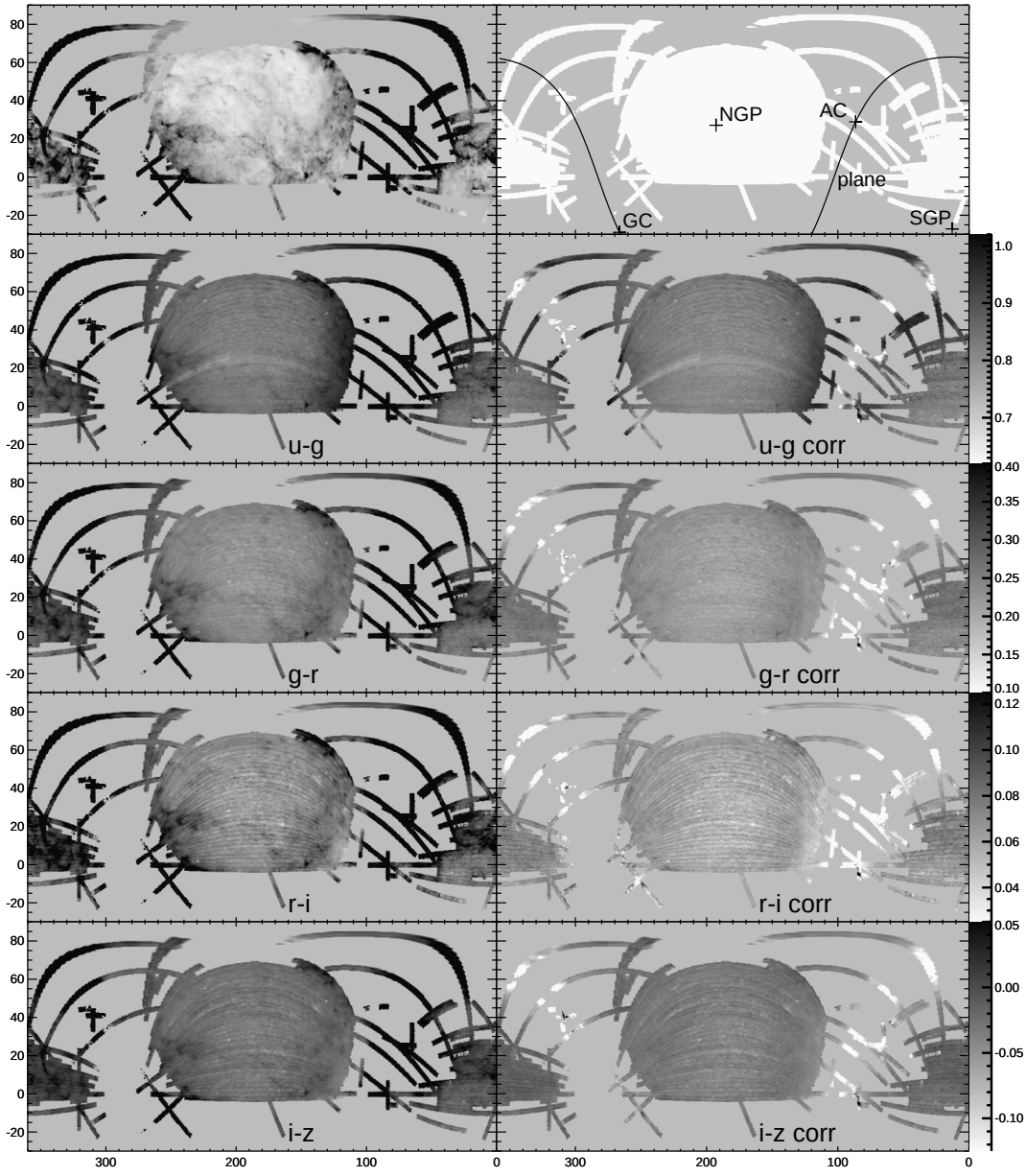

Figure 2.6 Blue tip colors over the SDSS footprint, for each SDSS color. The left hand panels give the observed blue tip color, while the right hand panels give blue tip colors after correction for dust extinction according to SFD and the coefficients $(A_a - A_b)/(\text{SFD } E(B-V))$ presented in this paper. The upper row of panels gives SFD and the locations of important points in the sky.

The maps show unmistakable signatures of dust (dark clouds in left panels of Figure 2.6) that are almost entirely removed when stellar colors are corrected

according to the SFD map. The residuals at high Galactic latitude after extinction correction are dominated by problems with the survey calibration—striping in the SDSS scan direction and a few runs with bad zero points in $u - g$. These artifacts are immediately apparent in Figure 2.7. There is also a slowly varying residual in which blue tip color becomes redder near the Galactic plane, until deep in the Galactic plane when the color shifts very blue.

The former effect is caused by the various stellar population sampled in different parts of the sky. In the plane, the higher metallicity, redder disk population becomes increasingly dominant over the halo population. The latter effect is a result of the violation of the assumption that all of the stars are behind all of the dust. Stars in front of the dust are dereddened with the full SFD dust column, and are therefore rendered extremely blue. These stars are then seen by the blue tip algorithm as the signature of the blue tip, resulting in a spuriously blue color. Even in less dusty regions where at least some MSTO stars are behind all of the dust, the method can fail if an insufficiently faint range of D is used. In this case, MSTO stars behind different amounts of dust are grouped together in finding the best fit, blurring the blue edge of the stellar locus. Because σ_P for the fit is fixed, this will result in a bluer than average blue tip color, while SFD would track the color of the MSTO stars behind all of the dust—the reddest stars in the group. These effects, however, are only noticeable in the dustiest region of the sky, where $|b| <\sim 15°$.

The Monoceros stream is clearly visible as a feature at $(\alpha, \delta) = (110°, -10°)$ – $(110°, 60°)$ in the blue tip maps, because its MSTO is bluer than that of the thick and thin disks (Newberg et al., 2002), except in $u - g$.

There are two types of survey-systematic induced residuals in the maps, both of which are seen as striping along the SDSS scan direction. The less important are the few, large, $\sim 3°$ wide stripes that are most noticeable on the eastern edge of the $u - g$

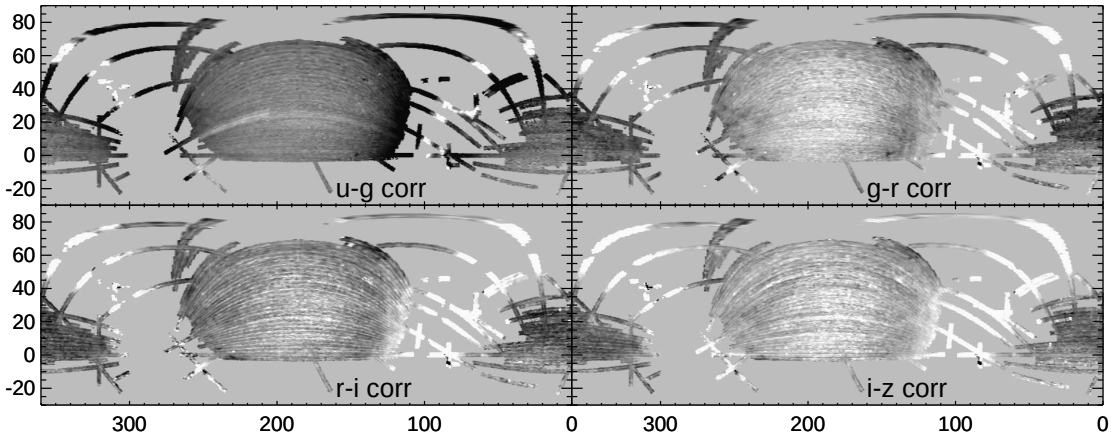

Figure 2.7 Stretched version of Figure 2.6, highlighting residuals. The Monoceros stream is prominent at the right hand side of the NGP region of the footprint. White to black spans 0.225, 0.11, 0.05, and 0.06 mag.

blue tip maps. These regions correspond to the footprints of SDSS runs that have slight zero point offsets from the rest of the survey. The more troubling residual is the universal small-scale striping along the scan direction. This corresponds to the 13 arcminute scale of the SDSS camera columns. We have not fully examined this residual, but attribute it to different filter responses between the 6 SDSS camera columns (Doi et al., 2010). The SDSS ubercalibration algorithm ties stars of some mean color together, but does not account for color terms between the SDSS camera columns (Padmanabhan et al., 2008). As the MSTO stars are substantially more blue than the typical SDSS star, they are particularly vulnerable to color terms. Complicating this explanation of the camera column striping is the observation that the best fit camera column offsets derived in §2.4.2 are different for the brightest range of D used than for fainter ranges of D, which are mutually compatible. We interpret this as a saturation or nonlinearity effect that depends on camera column, though we remove any stars flagged as saturated from the analysis. These systematics need to be addressed in fits to maps of the blue tip.

2.4 Fitting the Blue Tip Map

The sensitivity of the blue tip colors to dust reddening makes for a natural test of the SFD map. We carry out the simplest tests of SFD permitted by the blue tip maps here, checking the dust map normalization and the $R_V = 3.1$ reddening law assumed by SFD for extrapolating reddening to colors other than $B - V$. The reddening law used in SFD is from O'Donnell (1994), which is similar to the Cardelli et al. (1989, CCM) reddening law.

The SFD dust map is often used as a map of reddening $E(B - V)$, but is based fundamentally on thermal emission from dust. In SFD, the thermal emission is converted to reddening based on a single dust map normalization constant. This constant was derived by comparing the observed reddenings $E(B - V)$ of a sample of elliptical galaxies to the SFD temperature-corrected emission from dust at their locations (Faber et al., 1989).

We repeat this test, using the colors of the blue tip of the stellar locus in place of the $B - V$ color of galaxies. Because of the five band photometry provided by the SDSS, we are able to extend the SFD test by additionally checking the assumed O'Donnell $R_V = 3.1$ reddening law. Because of the number and accuracy of the blue tip color measurements, we are able to further look for spatial variation in the SFD normalization constant and the reddening law. The method is ultimately the same as in SFD, however: we find the best fit normalization constants that convert from dust emission (or $E(B - V)_{\rm SFD}$, as these are proportional) to reddening. We extend this test to multiple colors and check for variation over the sky.

To perform this test each blue tip map would be fit, ideally, as

$$(m_a - m_b)_{\rm bluetip} = R_{a-b} E(B - V)_{\rm SFD} + C, \tag{2.3}$$

over a part of the sky, where $(m_a - m_b)_{\rm bluetip}$ is the blue tip map for the color $a - b$, R_{a-b} is the normalization constant to be measured, and C is the intrinsic blue tip color. However, because the blue tip of the stellar locus is not a universal color standard, but rather varies with position in a way likely substantially covariant with the dust map, this fit is impractical. Moreover, the survey striping artifacts discussed in §2.3.3 could further throw off the fit. To account for these two effects, we instead fit

$$(m_a - m_b)_{\rm bluetip} = R_{a-b} E(B-V)_{\rm SFD} + Q_r(f) + C_i \tag{2.4}$$

where $Q_r(f)$ is a quadratic for run r in SDSS field number f and C_i is the camera column offset for camera column i. We fix C_1 to be zero to remove the degeneracy with the constant term in $Q_r(f)$. The quadratic $Q_r(f)$ simultaneously accounts for zero point errors in the SDSS calibration and slow intrinsic variation in blue tip color.

Because we bin 10 SDSS fields together for each blue tip measurement, variations in the dust map on scales much smaller than 1.5° in the scan direction will not be captured in the blue tip measurements. The blue tip method is not a linear operator on the underlying stellar colors, so the measured color of the blue tip is not linearly related to the mean of $E(B-V)_{\rm SFD}$ in the fields. In this work, for each set of fields contributing to a blue tip measurement, we use the median $E(B-V)_{\rm SFD}$ in those fields as proportional to the expected reddening of that measurement. This is not strictly correct, but insofar as the dust does not vary too quickly, this filtering seems to approximate the correct behavior.

After finding the best fit R_{a-b} in each color, we repeat the blue tip measurements on the SDSS stars, this time with individual stellar colors corrected according to the derived fit parameters R_{a-b}, at the full resolution of the dust map. This process converges in a few iterations. The iteration renders the final fits insensitive to the

details of the dust map filtering. We have verified the insensitivity to the filtering by noting that fits to the unbinned blue tip maps using an unfiltered SFD map give fit coefficients that are compatible with the fits to the binned blue tip maps.

We model the striping in camera columns by constant terms in the fit for each camera column. Empirically this correction is satisfactory, but we note that if our interpretation of the camera column offsets as derived from color terms is correct, the response of each camera column to dust is slightly biased. However, we detect camera column offsets of ~ 5 mmag over differences in stellar colors of a few tenths of magnitudes, implying that this bias is less than 1%. Figure 2.8 shows the derived offset in each SDSS camera column for stars in a variety of D. Furthemore, the bias will be different in each camera column and it must be, on average, zero. We have further confirmed that our results are unaffected by the color terms by separately fitting the dust map to each SDSS camera column individually, obtaining fits consistent with the global 6 camera column fit (§2.4.3).

2.4.1 Fits to Individual SDSS Runs

In some cases, a single run is long enough and dusty enough to individually constrain the dust reddening coefficients R_{a-b} in each color at the 10% level, even when fitting for camera column offsets and a quadratic. Figure 2.9 shows the fits for these runs. The fits show substantial variation in R_{a-b}. Most of this variation takes the form of an overall difference in dust absorption normalization, rather than as variation in the shape of the dust reddening spectrum. Some low, outlying values of R_{u-g} suggest that the run is so extinguished that substantial numbers of stars are not detected in the u band, ruining the fit. The fits remove nearly any trace of dust in these runs, as shown in Figure 2.10.

Fits to the runs individually well constrained by the dust map indicate significant

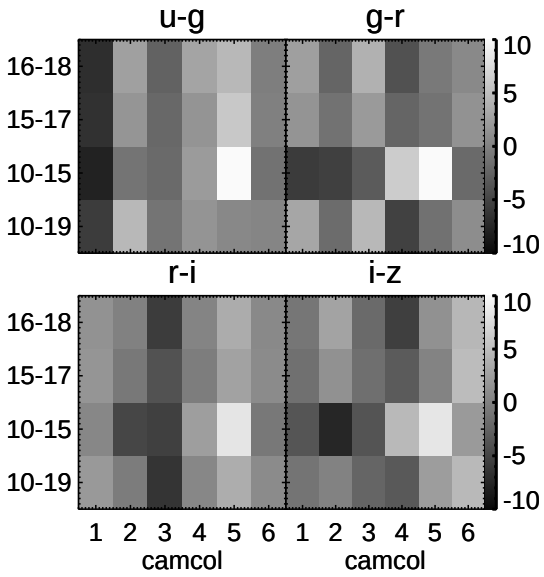

Figure 2.8 The camera column offsets used to destripe the SDSS blue tip maps, derived from the global blue tip map fits (§2.4.2). The left-hand axis labels give the range of D to which the offsets apply. The right hand labels give the value of the grayscale in mmag. The offsets are compatible for different ranges of D, except at the brightest magnitudes ($10 < D < 15$), where nonlinearity effects may be coming into play.

variation in normalization as well as, to a lesser extent, variation in dust extinction spectrum, especially as a $\sim 20\%$ effect in normalization. Accordingly, in finding a global fit to the dust properties, we remove from the fit regions that we deem discrepant from the "average" dust properties. To do this, first we individually fit each SDSS run. Runs with best fit R_{a-b} more than 5σ from the inverse variance weighted average of R_{a-b} for all the SDSS runs are excluded from the global fit. Additionally, the global fit is iterated and σ-clipped field-by-field at 5σ.

2.4.2 Global Fit to All SDSS Runs

We find the best fit (least squares sense) combination of the SFD dust map, constant offsets for each camera column other than the first, and quadratics in field number for each run to the blue tip map via singular value decomposition. We do not fit for the

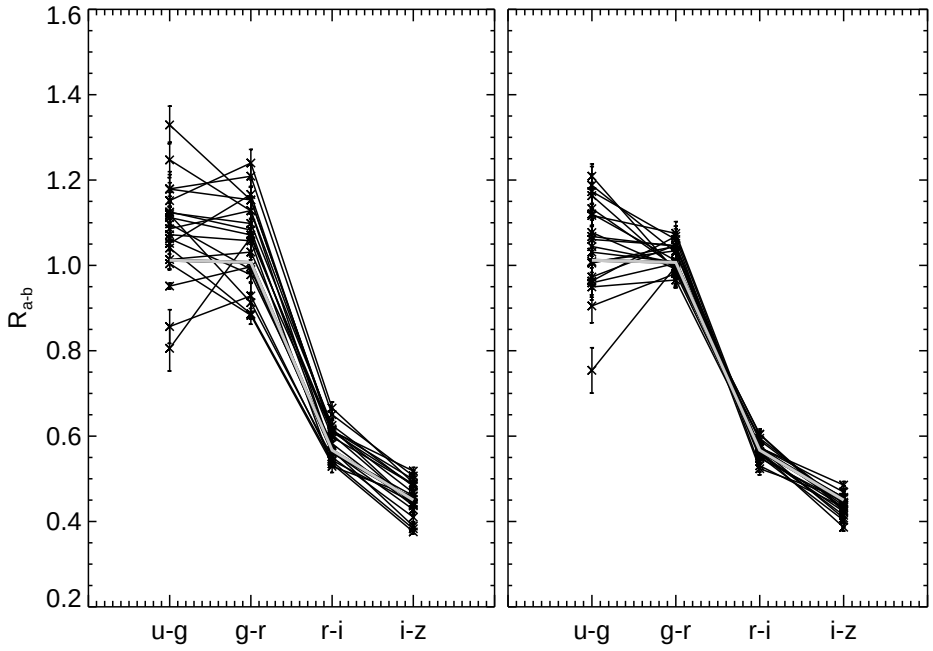

Figure 2.9 R_{a-b} for the four SDSS colors, for a selection of individually well constrained SDSS runs. The reddening spectrum has a similar shape among the different runs, but there is substantial scatter in the overall normalization (left). After forcing the mean of R_{g-r}, R_{r-i}, and R_{i-z} to match for each run, there is close agreement among the various dust extinction spectra (right). Error bars account only for the formal statistical uncertainties. The thick gray line in each plot gives the global best fit R_{a-b} derived in this work.

offset for the first camera column because changing the offsets for all of the camera columns is degenerate with changing the constant offsets in the quadratics for each run. Specifically, we find the parameters $\mathbf{x}$ satisfying

$$\mathbf{A}^\intercal \mathbf{C}^{-1} \mathbf{A} \mathbf{x} = \mathbf{A}^\intercal \mathbf{C}^{-1} \mathbf{b} \tag{2.5}$$

which provides the least squares solution to $\mathbf{A}\mathbf{x} = \mathbf{b}$. Here $\mathbf{C}$ is a diagonal covariance matrix, with the variances determined by the formal statistical uncertainties in the blue tip fit to each field (or binned fields). The blue tip color for each field (or binned fields) is in $\mathbf{b}$. The design matrix $\mathbf{A}$ has dimensions $n_{\rm field} \times n_{\rm param}$. It contains one

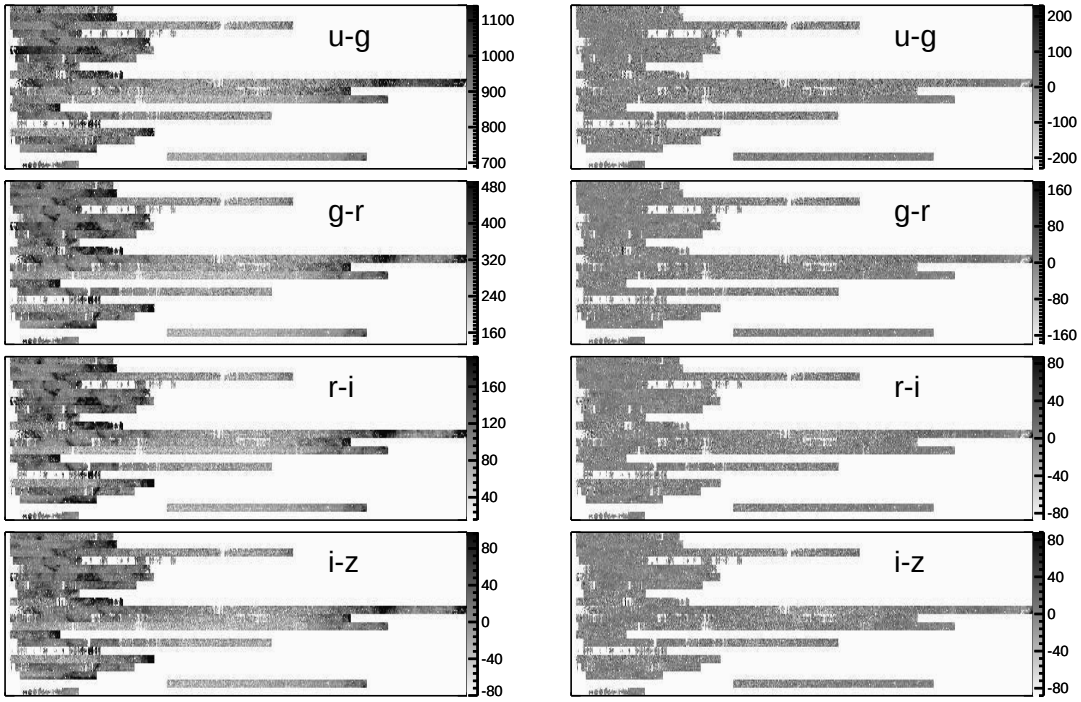

Figure 2.10 Blue tip colors (left) and residuals (right) for the runs in Figure 2.9, in mmag. Coherent signals from the dust are manifest (left). After fitting according to §2.4, the residuals show little structure (right).

column for the SFD dust map values in each field, five columns for the offsets for the SDSS camera columns two through six, and three columns for each of the 792 runs composing the SDSS-III, for the three terms in the quadratics for each run.

The SDSS-III contains imaging data on 1,147,506 fields. We require that the SDSS score[1] of each run be greater than 0.5 and the PSF FWHM be less than 1.8 arcseconds in r, which reduces the number of fields to 686,554. Excluded runs typically are unphotometric, have bad seeing or are Apache Wheel calibration runs. The blue tip method is run on all of the remaining fields, or binned sets of these fields. It occasionally fails, due to an insufficient number of stars or apparent

[1]The SDSS score of a field reflects sensitivity to point sources and is derived from sky brightness and seeing. It further is capped at 0.5 for fields deemed unphotometric or runs fields using binned pixels (i.e., Apache Wheel fields).

detection of the blue tip blueward of -0.75 mag or redward of 2.4, 2.4, 1.8, and 1.6 mag in $u-g$, $g-r$, $r-i$, and $i-z$, respectively. The number of binned fields that successfully make it through the blue tip fit depends on the range of D used and the color, but in the ranges of D examined here it ranges from 684,000 to 677,000. Unbinned fields fail for lack of stars at high Galactic latitudes, and so fewer fields are successful: in ranges of D of interest, between 683,000 and 620,000 fields pass. The median number of stars contributing to the fits in each unbinned field at $10 < D < 19$ is 100. About 10^8 stars enter into the fits.

The global fit produces the coefficients R_{a-b} in Table 2.1 and at high latitudes leaves few noticeable coherent residuals. Figure 2.11 shows a map of these residuals. Nevertheless, a few dust clouds clearly are imperfectly subtracted. Most prominently, in the north, a few undersubtracted clouds in $g-r$ stand out on the eastern side of the north Galactic cap (NGC). Undersubtracted clouds in the northwest and at (α, δ) = (145°, 0°) cause the runs including them to be excluded from the fit. The former feature is the largest residual in the Peek & Graves (2010) maps. Subtraction in the south is remarkably clean, though at right ascensions and declinations of (340°, 20°) and (60°, 0°) there are slightly oversubtracted clouds. A cloud at (45°, 20°) barely makes it into the SDSS footprint, and is badly oversubtracted, causing the exclusion of its run from the global fit. In $g-r$ especially, a residual associated with the Monoceros stream stands out at the western edge of the NGC. We have tried masking this region and repeating the fit, but as the Monoceros stream is not correlated with the dust, the fit results were unchanged.

Figure 2.12 shows the blue tip color residuals as a function of $E(B-V)_{\rm SFD}$. The residuals are generally flat with $E(B-V)_{\rm SFD}$. In $r-i$ and $i-z$, any trend with $E(B-V)$ is at less than the 2% level. In $u-g$ there is no discernible trend, though the scatter is large. In $g-r$ there seem to be disturbing 5-10% trends with $E(B-V)$

Table 2.1. R_{a-b} for the SDSS colors

SDSS color	SFD	$R_V = 3.1$ O'Donnell	blue tip
$u-g$	1.362	1.138	1.01 ± 0.10
$g-r$	1.042	1.141	1.01 ± 0.08
$r-i$	0.665	0.616	0.57 ± 0.05
$i-z$	0.607	0.624	0.45 ± 0.05

Note. — R_{a-b} according to the original SFD prescription, an $R_V = 3.1$ O'Donnell prescription with updated SDSS filter definitions, and the best blue tip global fit coefficients. The formal statistical error bars are negligible; those presented here are based on the empirical field-to-field variation in best fit extinction law as discussed in §2.5. This gives highly covariant uncertainties because the field-to-field variations are dominated by changes in best fit dust map normalization (see the covariance matrix in Table 2.3).

but they may stabilize around $E(B-V) = 0.4$ mag, with reddenings off by only 15 mmag there.

The blue tip maps have residuals with distributions given in Figure 2.13. The core of the distribution is Gaussian, but the wings are non-Gaussian, falling off more slowly than would be expected. The blue tip method gives median estimated uncertainties as 17.5, 12.5, 5.7, and 5.8 mmag, closely reproducing the Gaussian fits to the residual distribution, which give 18.1, 12.3, 6.9, and 7.8 mmag in $u-g$, $g-r$, $r-i$, and $i-z$, respectively.

The polynomial terms from the global fit are intended to model the slow, intrinsic variation in the blue tip color and per-run calibration offsets, and so are of independent interest. Figure 2.14 shows that these maps are heavily striped. Some of this striping is clearly removing calibration problems with the SDSS, as in the eastern

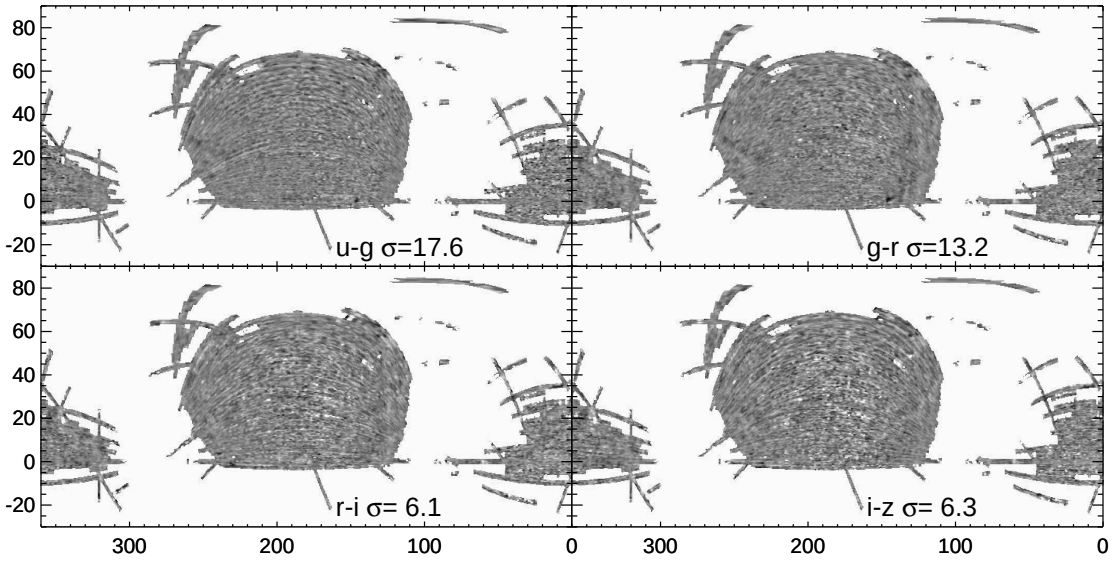

Figure 2.11 Blue tip color residuals after removing best fit linear combination of dust map and polynomials, as described in §2.4.2. White corresponds to $+3\sigma$, while black corresponds to -3σ.

side of the NGC in $u - g$. The striping at high latitudes in the north in other colors is probably substantially an artifact of the low signal in these regions, but the typical stripe-to-stripe difference there is only ~ 5 mmag, and at worst 10 mmag.

The SDSS imaging contains a number of runs crossing the Galactic plane, as part of SEGUE (Yanny et al., 2009). All of these runs and a few other low Galactic latitude runs get identified as discrepant by the fitting algorithm and discarded from the final fit. In a run-by-run treatment, this is inevitable, as at very high extinction the blue tip method will fail because the stars are not behind all the dust. However, for $|b| > 10°$, inspection of the blue tip residual maps suggests that the SEGUE runs could be well fit also, although we have not tried that here. The signal from the dust in the SEGUE runs is sufficiently rich to merit treatment separate from the bulk of the high Galactic latitude sky, as is done in Berry et al. (2011).

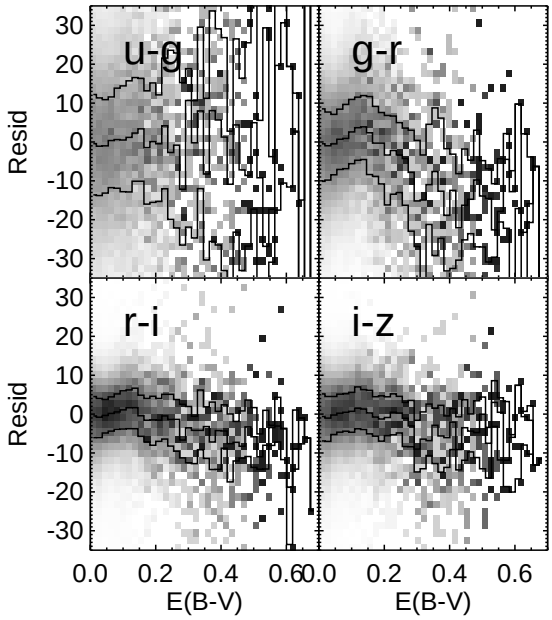

Figure 2.12 Blue tip color residuals with $E(B-V)_{\rm SFD}$. The residuals in $u-g$, $r-i$, and $i-z$ reassuringly show no trend with $E(B-V)$. In $g-r$, the residuals have some structure, but the positive slope at $E(B-V)<0.2$ and the negative one around $0.2<E(B-V)<0.4$ are only 5% effects—the residuals are largely uncorrelated with $E(B-V)$.

2.4.3 Fits to different sky regions

Given the presence of dust-correlated residuals in different parts of the sky, one wonders whether the fit is actually "global" in a useful sense, or is primarily a product of the footprint we have decided to look at. Accordingly, we have cut the sky into a number of subregions and separately found the best fit R_{a-b} in each. To test for large scale variations in R_{a-b}, we divide the sky into northern ($b>25^\circ$) and southern ($b<-25^\circ$) Galactic regions, as well as octants of the sky divided by lines of constant Galactic longitude. To try to test variation in dust properties as a function of extinction or temperature, we divide the sky into regions of dust of different extinctions and temperatures. Finally, to verify that we have satisfactorily accounted

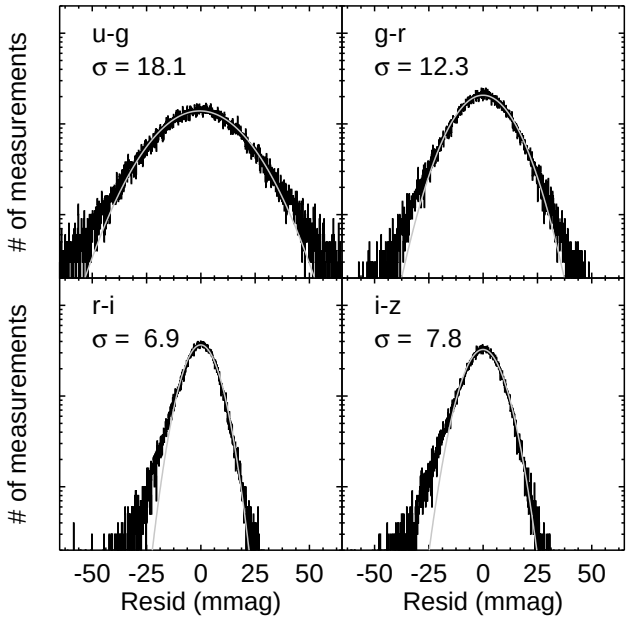

Figure 2.13 Fit residuals, in mmag. The core of the distribution is well fit by a Gaussian, but the wings fall off more slowly than in a Gaussian. The colors $r - i$ and $i - z$ have the tightest distributions, likely because the blue tip is less dependent on metallicity in these colors.

for the camera column offsets, we divide the SDSS survey into its six camera columns. Figure 2.15 shows the results of the fits to each of these different sky regions.

We restrict to the main global fit region and apply the globally derived camera column offsets to the blue tip colors. We remove best fit polynomials from the filtered SFD dust map and from the blue tip colors, as in §2.4, using the global fit region. We then find the best fit of the filtered, polynomial-subtracted dust map to the polynomial-subtracted blue tip map, restricted to various subsets of the full region.

The results are encouragingly consistent, given that we have already seen that dust reddening normalization can vary substantially, along with, to a lesser extent, its spectrum, as seen in Figure 2.9. We find the dust extinction normalization and spectrum to be consistent at the 10% level. The north/south normalization

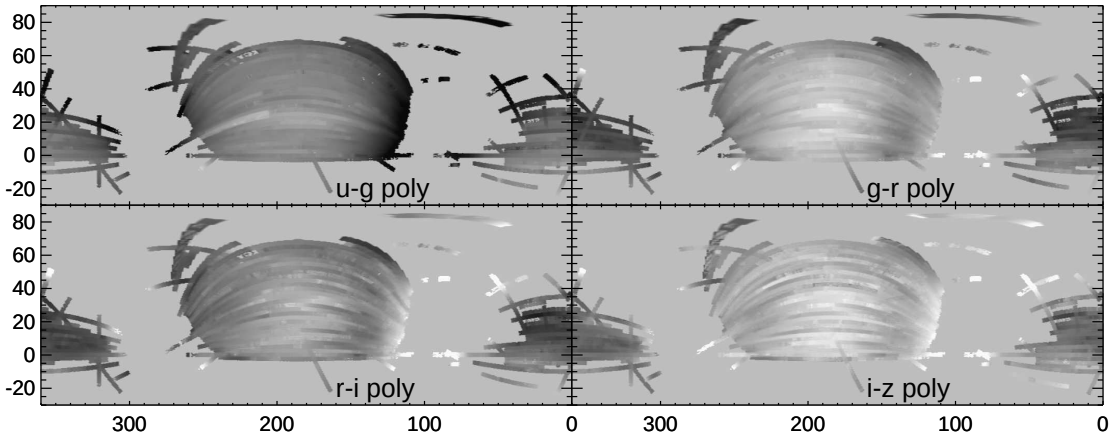

Figure 2.14 Map of the polynomial terms from the global fits. The scale is the same as in Figure 2.7. These maps model the intrinsic variation of the blue tip color on the sky as well as per-run SDSS calibration offsets.

discrepancy is the most surprising, with the north preferring a normalization about 15% larger. We also find that dust with $0.6 < E(B-V) < 1.0$ mag prefers a $\sim 15\%$ smaller normalization than dust with $0 < E(B-V) < 0.05$ mag. Dust at different temperatures likewise has similar extinction normalizations and spectra.

2.4.4 Fits to a Mock Star Catalog

The reliability of the fitting procedure can be tested by running the fit on a star catalog from a mock galaxy model. The mock catalog was generated with the *galfast* catalog generation code (Jurić, in prep). Given a model of stellar number density, metallicity, a 3D extinction map, the photometric system, and instrumental errors, *galfast* generates realistic mock photometric survey catalogs.

As inputs, we used the number density distribution parameters from Jurić et al. (2008) and the metallicity distribution from Ivezić et al. (2008). The three-dimensional dust distribution map was generated using the model of Amôres & Lépine (2005). The generated u, g, r, i, and z magnitudes were convolved

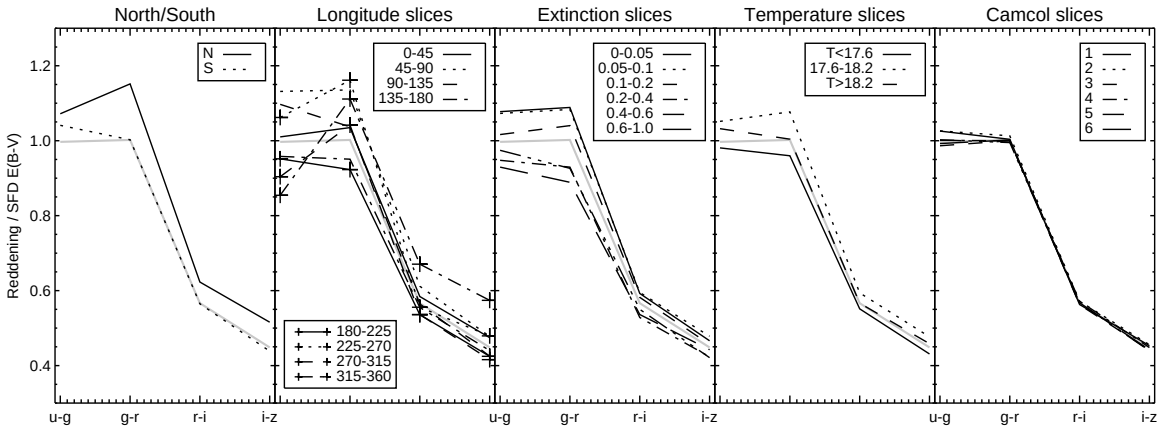

Figure 2.15 R_{a-b} for the SDSS colors over different subsets of the SDSS footprint. The first panel gives the coefficients for the north ($b > 25°$) and south ($b < -25°$). The next panel gives the best fit coefficients for eight slices in Galactic longitude. The third panel gives coefficients in regions of sky with increasing extinction. The fourth panel divides the sky into regions of three different temperatures, and the fifth panel divides the survey by SDSS camera column. The thick gray line in each panel gives the global best fit R_{a-b} derived in this work.

with magnitude-dependent errors representative of SDSS, and the final catalog was flux limited at $r < 22.5$.

The three-dimensional dust map was modified from Amôres & Lépine (2005) to contain the small-scale clouds seen in SFD. This was performed by scaling each line of sight from the model by the ratio $E(B-V)_{\rm SFD}/E(B-V)_{\rm model,100kpc}$, so that the model matches SFD at 100 kpc. The resulting map contains the expected average three dimensional distribution of the dust combined with the angular structures present in SFD.

We construct a mock galaxy using *galfast* and then construct catalogs of observations of these stars for each SDSS run. The resulting catalogs are proccesed by the blue tip analysis code in exactly the way that the actual SDSS catalogs are processed. As for the actual catalogs, the median number of stars per field is ~ 100.

Blue tip fits performed on the mock galaxy recover the R_{a-b} used to within 3%.

This verifies that we properly account for shifts in the blue tip color due to metallicity. However, for these tests we have assumed that SFD correctly predicts the line of sight column density and that the reddening law is the same everywhere on the sky, at least at high Galactic latitudes and in the optical. Insofar as the final fit residuals are largely flat (Figure 2.11), this assumption seems justified. Moreover we can verify that the ratios of the R_{a-b} derived independently from SFD agree with the ratios of the R_{a-b} derived here.

2.4.5 Fitting Ratios of R_{a-b} without SFD

The preceding analysis has assumed that SFD is a good template for the dust. However, we can relax our dependence on SFD if we restrict our attention to ratios between different R_{a-b}.

In the absence of changing stellar populations and calibration errors, blue tip colors will fall along a single line given by the reddening vector. By removing a quadratic in field number and accounting for camera column offsets as in §2.4.2, we remove variations in blue tip color not associated with reddening. By fitting a line to the resulting polynomial-subtracted blue tip color-color diagrams, we measure the ratio of the R_{a-b}. Some striping along the SDSS scan direction is evident in the blue tip residuals despite our attempts to remove it, and this striping will be deleterious to the fit results because we cannot rely on its being uncorrelated with the dust template we fit. Accordingly, we fit lines for each camera column, eliminating the effect of striping, and average the results. The results are shown in Figure 2.16.

These color-color fit results are in good agreement with the results of §2.4.2 (Table 2.2). The results agree to about 1σ with the SFD fit results, where the uncertainties σ are given by the standard deviations of the fit results between the camera columns. The original SFD prescription is seen to clearly overestimate

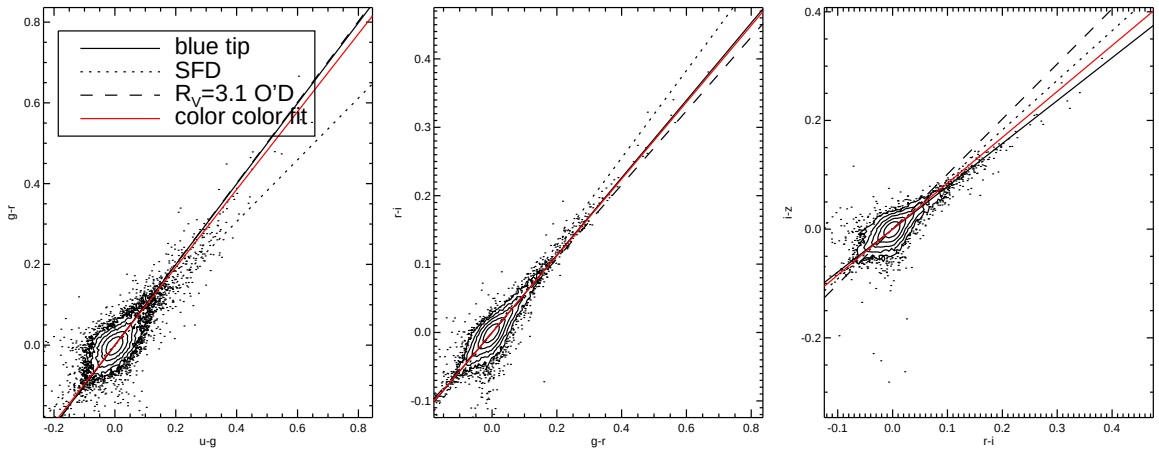

Figure 2.16 Plots of the colors of the blue tip in different colors, for camera column one. Spatially slowly varying terms have been removed, so points should fall along the line R_{a-b}/R_{c-d}. The reddening coefficients presented here best trace the distribution of points.

R_{u-g}/R_{g-r} (see §2.5.1), while both the original SFD prescription and the updated $R_V = 3.1$ O'Donnell reddening law are found to underestimate R_{r-i}/R_{i-z}.

2.5 Discussion

In this section, we use the blue tip fits presented above to constrain reddening laws and to test the SFD normalization and temperature correction. We then briefly point out a discrepancy in the color of the dereddened blue tip between the north and south, which is plausibly a consequence of a different stellar population in the north than in the south.

2.5.1 Constraining Reddening Laws

Connecting Reddening Laws to R_{a-b}

A reddening law gives the extinction $A(\lambda)$ over a range of wavelengths λ and so makes a prediction for the R_{a-b} that we have fit. The extinction in band b, in the

Table 2.2. Blue Tip Color-Color Fit Results

Color ratio	SFD	O'Donnell	blue tip	color color
A_{u-g}/A_{g-r}	1.307	0.997	1.005	1.019 ± 0.025
A_{g-r}/A_{r-i}	1.567	1.852	1.776	1.728 ± 0.038
A_{r-i}/A_{i-z}	1.096	0.987	1.260	1.237 ± 0.042

Note. — Blue tip color-color fit results. The results are in close agreement with the global blue tip fits, while excluding the original SFD reddening law and an $R_V = 3.1$ O'Donnell reddening law. These fits do not use SFD as a template and so test the shape of the reddening law without reference to SFD.

limit that the variation in the extinction over that band in small, is given by $\Delta m_b = A(\lambda_{\mathrm{eff},b,S})E(B-V)$, with

$$\lambda_{\mathrm{eff},b,S} = \frac{\int d\lambda \lambda S(\lambda) W_b(\lambda)}{\int d\lambda S(\lambda) W_b(\lambda)} \tag{2.6}$$

Here the system response for band b is given by $W_b(\lambda)$, $S(\lambda)$ is the source spectrum in photons/s/Å, and $A(\lambda)$ is the reddening law, normalized to give $A(\lambda_{\mathrm{eff},B,S}) - A(\lambda_{\mathrm{eff},V,S}) = 1$. The reddening in the color $a-b$ is then given by $(A(\lambda_{\mathrm{eff},a,S}) - A(\lambda_{\mathrm{eff},b,S}))E(B-V)$, from which it follows that $R_{a-b} = (A(\lambda_{\mathrm{eff},a,S}) - A(\lambda_{\mathrm{eff},b,S}))E(B-V)/E(B-V)_{\mathrm{SFD}}$. Here we have assumed that the variation in the extinction over the band pass is small; for $E(B-V) < 1$, this assumption changes the predicted R_{a-b} by less than 1% in $r-i$ and $i-z$, and less than 5% in $g-r$ and $u-g$.

Accordingly, we evaluate the extinctions in each SDSS pass band using the SDSS system throughputs and a MSTO source spectrum from a Kurucz model with

$T_{\rm eff} = 7000$K, for a variety of reddening laws (Gunn et al., 1998; Kurucz, 1993). We examine in particular the CCM, O'Donnell, and Fitzpatrick (1999, F99) reddening laws, which are parameterized by $R_V = A_V/E(B-V)$. We find the best fit factors R_V to our measured R_{a-b} for each of these reddening laws.

The other free parameter in these fits is the best fit normalization $N' = E(B-V)/E(B-V)_{\rm SFD}$. We do not report this parameter directly. The SFD dust map is based on a map of thermal emission from dust and is correspondingly proportional to $\tau_{100\ \mu{\rm m}}$, the optical depth of dust at 100 μm. Empirically, the ratio between $\tau_{100\ \mu{\rm m}}$ and $E(B-V)$ is itself a function of R_V, and so N' is covariant with R_V. However, the ratio between $\tau_{1\ \mu{\rm m}}$ and $\tau_{100\ \mu{\rm m}}$ depends less on R_V, so we report $N = A_{1\ \mu{\rm m,\ predicted}}/A_{1\ \mu{\rm m,\ SFD}}$. Here $A_{1\ \mu{\rm m,\ predicted}}$ is the extinction at 1 μm implied by the best fit reddening law and $A_{1\ \mu{\rm m,\ SFD}}$ is the SFD-predicted extinction, extrapolated to 1 μm following the $R_V = 3.1$ O'Donnell reddening law assumed by SFD. The quantity $A_{1\ \mu{\rm m,\ SFD}}$ is simply $1.32 \cdot E(B-V)_{\rm SFD}$. We find that the F99 reddening law provides the best fit to the R_{a-b} we measure, so we additionally mention for reference that the F99 reddening law ratio $E(B-V)/A_{1\ \mu{\rm m}}$ is 11% larger than the O'Donnell ratio $E(B-V)/A_{1\ \mu{\rm m}}$, though this depends on the adopted R_V and source spectrum.

R_V and N for Individual Runs

We have found that the dust extinction spectrum normalization and shape vary over the sky (Figure 2.9). We can quantify this effect in terms of variation in N and R_V by fitting reddening laws to the runs that individually well constrain R_{a-b} (§2.4.1). We use the F99 reddening law here rather than the traditional CCM or O'Donnell reddening law because the latter two reddening laws (especially the O'Donnell reddening law) predict that $R_{r-i} \approx R_{i-z}$, which is a poor fit to the data. Figure 2.17

shows that the derived N and R_V vary from run to run, especially as a $\sim 20\%$ scatter in normalization. Almost all of the runs are consistent with $2.8 < R_V < 3.2$. The distribution of R_V and N validates our use of 1 μm as a refererence wavelength for N, as the two parameters appear uncorrelated.

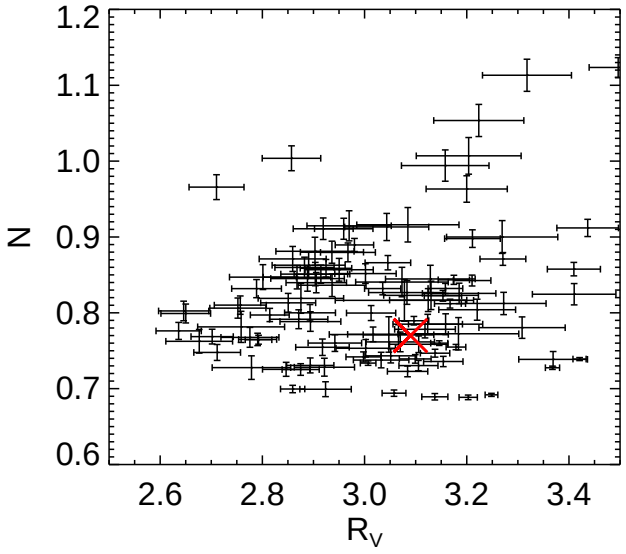

Figure 2.17 Best fit R_V and dust map normalization N for SDSS runs that individually well constrain R_{a-b}, examples of which are in Figure 2.9. Dust map normalizations vary by as much as a factor of two, though most are consistent at the 20% level. The large red "X" indicates the location of the best fit R_V and normalization to the global fit R_{a-b}. Error bars account only for the formal statistical uncertainties.

R_V and N for the Global Fit

In order to compute best-fit reddening laws for the global fit R_{a-b}, we need to account for the covariance in the R_{a-b} over the sky in addition to the formal statistical uncertainties in the fit. These uncertainties are about a part in one thousand. However, the best fit normalization can vary at the 10% level from field to field, and the part in a thousand uncertainty reflects averaging these fluctuations over many fields. While the dust extinction spectrum seems relatively constant, it would

be surprising if the average reddening reflected the reddening of any particular dust cloud at the part in a thousand level, so another method for estimating the uncertainties is needed. The uncertainties reported in Table 2.1 are the standard deviations in R_{a-b} for 8 octants in Galactic longitude, and do not account for the covariance of the measurements in the different colors owing to the changing best fit normalization.

The consequence of adopting uncertainties based on the field-to-field variation in the dust extinction spectrum is that the resulting uncertainties on N and R_V will describe the range of N and R_V among the clouds within the footprint we analyze. They do not give the uncertainties on the best fit N and R_V within our sample, which are more tightly constrained. As mentioned, the formal statistical uncertainties are about one part in a thousand. Uncertainties estimated from using different ranges of D for selecting the stars give uncertainties of 2%, 2%, 1%, and 2% in R_{a-b} for the colors $u-g$, $g-r$, $r-i$, $i-z$, respectively.

The field-to-field variation in R_{a-b} can be estimated from the sample covariance matrix of best fit R_{a-b} in different sky regions. We find the best fit R_{a-b} at each point in the footprint. Because over most of the footprint the signal-to-noise in the filtered blue tip maps is too low to make a reliable determination of R_{a-b}, we include nearby pixels in the fit with weights given by a 7° smoothed Gaussian. The best fit R_{a-b} is then given by

$$R_{a-b,n} = \frac{\sum_i D_i C_i^{-1} W_{i,n} b_i}{\sum_i D_i^2 C_i^{-1} W_{i,n}} \tag{2.7}$$

where n is the pixel on the sky, i indexes over blue tip measurements, D gives the filtered dust map, b and C^{-1} give the blue tip measurement and its inverse variance, and $W_{i,n}$ is the weight matrix, corresponding to Gaussian smoothing with a FWHM of 7°.

Table 2.3. Eigenvalues and eigenvectors of the reddening covariance matrix

$\sqrt{\lambda}$	v_{u-g}	v_{g-r}	v_{r-i}	v_{i-z}
0.155	0.88	1.21	0.45	0.36
0.079	1.23	−0.51	−0.41	−0.79
0.031	0.51	−0.91	0.61	1.05
0.016	−0.15	−0.15	1.35	−0.83

Note. — Eigenvalues λ and eigenvectors $\mathbf{v}$ for the sample covariance matrix. Eigenvectors are normalized so that $|\mathbf{v}| = |\mathbf{R}_{\text{global fit}}|$, to facilitate comparison between R_{a-b} and the first, least well constrained eigenvector, which is roughly parallel to R_{a-b}.

The sample covariance matrix of the resulting maps of R_{a-b} is used as the covariance matrix for fits of reddening laws to R_{a-b} (Table 2.3). Only pixels with estimated uncertainty in R_{i-z} less than 0.01 are used for computing the sample covariance matrix, to avoid overestimating the intrinsic variance due to the uncertainty in the estimates. The largest eigenvalue of the covariance matrix ($2.4 \cdot 10^{-2}$) is 94 times larger than the smallest eigenvalue ($2.6 \cdot 10^{-4}$). The eigenvector with the largest eigenvalue is roughly parallel to a vector corresponding to changing the normalization of the spectrum, and that with the smallest eigenvalue corresponds to changing the relative amount of reddening in $r - i$ to $i - z$. This quantitatively agrees with our claim that the normalization of the reddening law is poorly constrained relative to its shape.

With this covariance matrix, the best fit reddening laws have $R_V = 3.9 \pm 0.4$, $N = 0.98 \pm 0.10$ for the O'Donnell reddening law, $R_V = 3.0 \pm 0.4$, $N = 0.75 \pm 0.10$ for

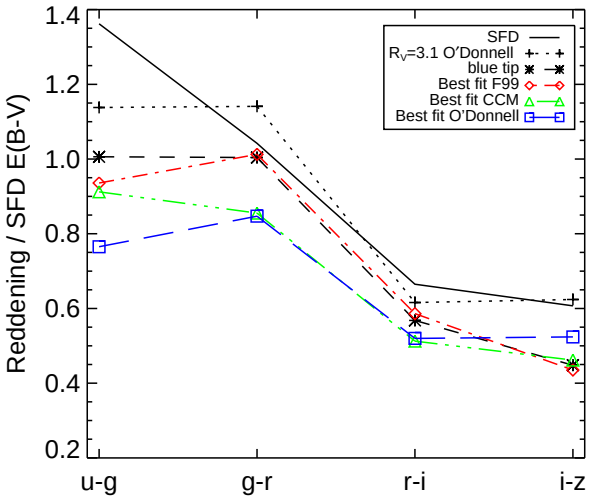

Figure 2.18 The original SFD reddening coefficients (solid line), updated coefficients according to the actual SDSS filters (crosses), and the best fit global coefficients found in this work (stars). We fit our best fit coefficients with reddening laws according to F99 (diamonds), CCM (triangles) and O'Donnell (squares). The F99 reddening law seems a good fit to each SDSS band (§2.5.1).

the CCM reddening law, and $R_V = 3.1 \pm 0.2$, $N = 0.78 \pm 0.06$ for the F99 reddening law. Figure 2.18 shows the resulting fits. The χ^2/dof of the O'Donnell, CCM, and F99 reddening laws are 7.8, 3.5, and 2.1 respectively. The O'Donnell and CCM reddening laws are disfavored because they predict smaller reddening differences between $r - i$ and $i - z$ relative to the data and the F99 reddening law. The F99 reddening law fits all of the points reasonably well.

The O'Donnell reddening law in particular and CCM reddening law to a lesser extent provide poor fits to the blue tip data, and the best-fit parameters are seriously driven by the poorly-matching $r - i$ and $i - z$ data. Accordingly, the derived R_V and N for these reddening laws are unphysical.

All of the fits give R_{u-g} substantially less than the value given in SFD (Figure 2.18). The values given in the SFD appendix were based on preliminary

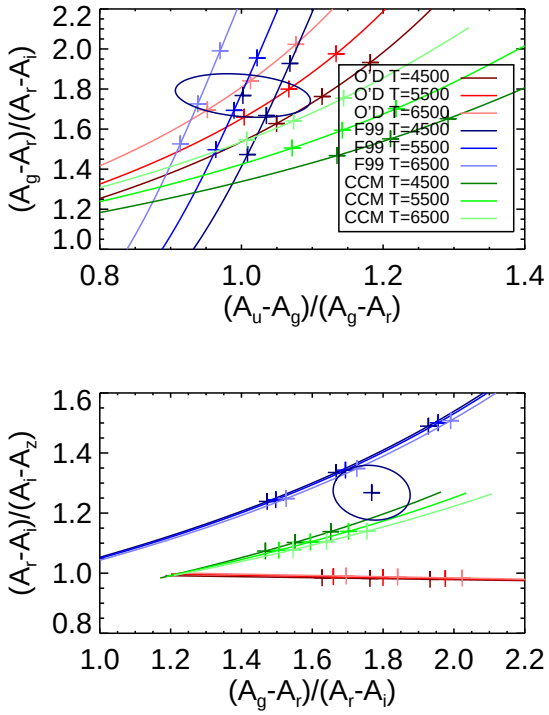

Figure 2.19 O'Donnell, CCM, and F99 reddening laws for different stars of different temperatures. $R_V = 2.6$, 3.1, and 3.6 are marked with crosses. R_V increases to the left. Ellipses are for the best fit blue tip values, with uncertainties computed from the covariance matrix of Table 2.3.

estimates of the system response of the SDSS, which varied somewhat from the actual system response. Using the SDSS system response from Gunn et al. (1998) for the $R_V = 3.1$ O'Donnell reddening law gives values different from those in SFD by 20% in $u - g$ and 10% in $g - r$ and $i - z$.

The predicted R_{a-b} depend somewhat on the source spectrum used. Figure 2.19 illustrates the effect of changing the source spectrum by plotting the derived reddening laws for the O'Donnell, CCM, and F99 reddening laws for Kurucz models (Kurucz, 1993) with $T = 6500$, 5500, and 4500 from the stellar spectra grid of Munari et al. (2005). The blue tip best fit reddening law is relatively insensitive to T over this range.

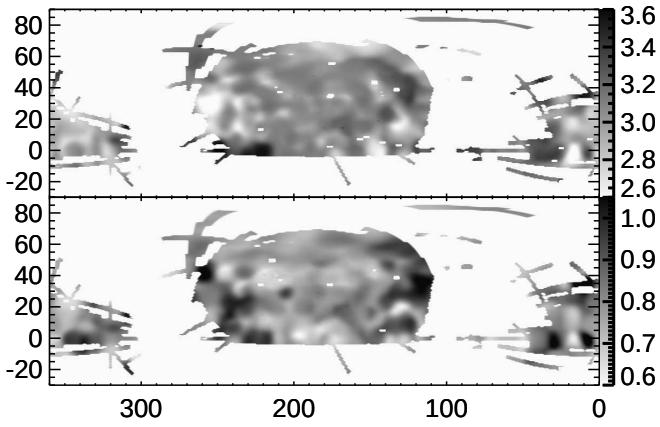

Figure 2.20 Maps of R_V (top) and dust map normalization (bottom) over the SDSS footprint. The map has been combined with a prior (§2.5.1) to reduce the scatter in regions of low signal-to-noise.

The maps of R_{a-b} over the sky can be combined to make maps of R_V and reddening law normalization over the sky. These maps are shown in Figure 2.20. To suppress noise in the measurement, we have combined the measured values with a prior of $R_V = 3.1 \pm 0.2$ and $N = 0.78 \pm 0.06$ to reduce the scatter in regions of low signal-to-noise. One feature of the maps of R_V and N is that the two maps are substantially uncorrelated. This again confirms the expectation that the ratio of $\tau_{1\ \mu\mathrm{m}}/\tau_{100\ \mu\mathrm{m}}$ does not depend on R_V.

2.5.2 Comparison with SFD Normalization

We can directly compare our predicted $E(B-V)$ with $E(B-V)_{\mathrm{SFD}}$ by using our best fit reddening law and accounting for the difference in source spectrum between the galaxies that SFD analyzed and the MSTO stars we analyze. We get $E(B-V)_{\mathrm{blue\ tip}} = 0.86 \cdot E(B-V)_{\mathrm{SFD}}$, suggesting SFD overpredicts reddening by about 14%. The estimated normalization uncertainty in SFD was 4%, while we claim 8%. However, the estimated fractional uncertainty of SFD was 16%, and we are now

in a position to attribute most of this uncertainty to varying best-fit normalization. Accordingly, it is unsurprising that the SFD normalization differs from ours by 14%, particularly given that the footprint we analyze is different from that used in SFD, and that we have found north/south normalization differences of about 15%.

2.5.3 The SFD Temperature Correction

The final $E(B-V)_{\rm SFD}$ takes the form $E(B-V)_{\rm SFD} = p\mathbf{I}_{corr}\mathbf{X}$, where p represents a normalization coefficient, $\mathbf{I}_{corr}$ represents the destriped, zodiacal-light subtracted *IRAS* 100 μm flux and $\mathbf{X}$ represents a temperature correction factor. An error in determining the temperature correction factor will lead to dust with a different best fit normalization, but with the same reddening spectrum, very much like what we see in the blue tip maps.

Accordingly, the blue tip fit residuals can plausibly be attributed to errors in the SFD temperature correction factor. In §2.4.3, we attempted to test the temperature correction by verifying that the best fit dust normalization was consistent for regions of different temperature according to SFD. However, this procedure assumes that the SFD temperature correction adequately distinguishes hot and cold dust. At high latitudes, the signal to noise of the DIRBE 100 μm and especially the 240 μm map are too low to construct a 100 μm/240 μm ratio map without substantial filtering. The SFD ratio map was constructed by first smoothing the 100 μm and 240 μm maps to 1° and then further weighting low S/N pixels to a high $|b|$ average ratio. Insofar as this procedure mixes dust of different temperatures together to a single reported SFD average temperature, it makes it difficult for us to test the SFD temperature correction using the SFD temperature map in this way.

One way to test the accuracy of the temperature correction at high $|b|$ is to compare the SFD temperature correction with the temperature correction used for

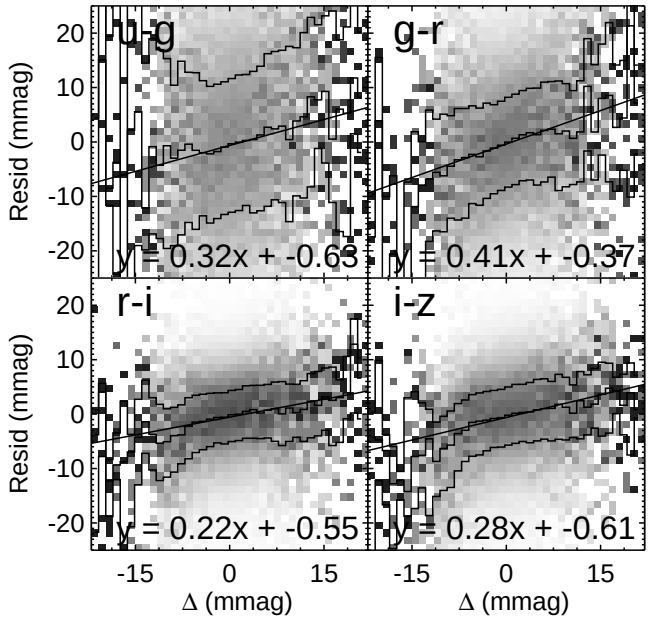

Figure 2.21 Blue tip color residuals versus change in filtered dust map $E(B-V)$ from using the FIRAS temperature correction rather than the SFD temperature correction (both in mmag). The linear trend suggests that the temperature correction may be at fault.

the FIRAS dust fits (Finkbeiner et al., 1999). The SFD temperature correction is weighted to constants in the north and south in regions of low signal to noise, while the FIRAS temperature correction is weighted to a 7° smoothed map in these regions. In high signal-to-noise regions the two corrections agree. Letting $\mathbf{X}_{\rm SFD}$ be the SFD temperature correction and $\mathbf{X}_{\rm FIRAS}$ be the FIRAS temperature correction, we can plot blue tip color residuals versus the change in predicted dust column density from switching from the SFD to the FIRAS temperature correction:
$\Delta = E(B-V)_{\rm SFD}(\mathbf{X}_{\rm FIRAS}/\mathbf{X}_{\rm SFD} - 1)$. Figure 2.21 gives the result.

Were the FIRAS temperature correction a much better predictor of dust temperature than SFD, we would hope for a linear trend between dust correction and blue tip residual, with slope equal to the best fit dust coefficients. Instead we find

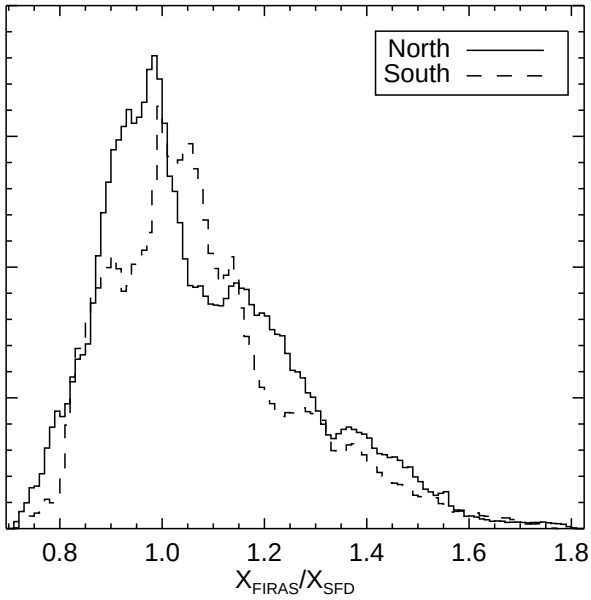

Figure 2.22 The ratio $\mathbf{X}_{\rm FIRAS}/\mathbf{X}_{\rm SFD}$ in the north (solid) and in the south (dashed). The temperature correction is systematically higher in the south than in the north by $\sim 10\%$, about compatible with the difference in best fit normalization between the north and south found in §2.4.3.

slopes of approximately half the best fit coefficients, suggesting that the true temperature map is between the SFD and F99 temperature maps. The specific values of the coefficients of the linear fits shown are not reliable because we have not accounted for the uncertainties in Δ in performing the fit, and so the slopes may be underestimated. Regardless, the fact that a clear linear trend with significant slope exists provides strong evidence that the temperature correction at high $|b|$ is unreliable.

The FIRAS temperature correction may also explain the $\sim 15\%$ normalization difference in best fit dust extinction spectrum observed between the north and the south in §2.4.3. Figure 2.22 shows that the ratio $\mathbf{X}_{\rm FIRAS}/\mathbf{X}_{\rm SFD}$ in regions with $E(B-V) < .05$ is about 10% higher in the south than in the north.

Table 2.4. North/South color asymmetry

Region	$u-g$	$g-r$	$r-i$	$i-z$
North (mag)	0.817	0.228	0.064	-0.033
South (mag)	0.824	0.250	0.071	-0.020
Difference (mmag)	7.6	21.8	7.2	12.4

Note. — Median blue tip color in the north and south, with $40 < |b| < 70$. The south is systematically redder than the north. This may be a sign of an interesting stellar structure in the south, or a calibration problem or SFD error.

2.5.4 The Dereddened Blue Tip in the North and South

The color of the blue tip changes because of both dust and because of changing stellar populations. If we deredden the blue tip according to SFD and the best fit R_{a-b} of this work, we expect the remaining variation in blue tip color to be due to changing stellar populations (Figure 2.7).

A surprising feature of the dereddened blue tip maps is that the SGC appears redder than the NGC in $g-r$, $r-i$, and $i-z$, especially outside a region in the southeast of the SGC (Table 2.4). This may be a genuine structure in the stellar population in the south, but we are unable to distinguish that possibility from calibration errors or errors in the dust map. However, because the south tends to prefer a smaller SFD normalization than the north, the dereddened south would have been expected to be too blue rather than too red (Figure 2.15). Moreover, the shape of the extra reddening in the different SDSS bands does not look like any plausible reddening law.

2.6 Conclusion

The blue tip of the stellar locus provides a viable color standard for testing reddening. It is also a sensitive probe of systematics in survey photometry: we detect striping artifacts from the SDSS camera columns as well as occasional runs with bad zero points. Reddening measurements based on the stellar locus are limited because the stellar locus varies with position on the sky, due to changing stellar populations. However, we find that we are able to overcome this limitation by looking for small-scale fluctuations that correlate with those in the SFD dust map. By removing the best fit quadratic from the blue tip colors in each SDSS run, both survey systematics and sky-varying stellar populations seem adequately accounted for: Gaussian fits to the blue tip residuals have σ of 18.1, 12.3, 6.9, and 7.8 mmag, compared with the median formal statistical uncertainties σ of 17.5, 12.5, 5.7, and 5.8 mmag in $u-g$, $g-r$, $r-i$, and $i-z$, respectively. Because our errors are not Gaussian, in terms of χ^2/dof we do worse; the fits have χ^2/dof of 1.49, 1.30, 2.16, and 2.28 in the four colors.

Using these reddening measurements over the SDSS footprint, including, especially, the new, dustier, southern data, we can sensitively constrain the SFD dust map normalization in each SDSS color. The original SFD values for $A_b/E(B-V)$ were in error because the filter responses used in the SFD appendix did not match the eventual filter responses used in the SDSS. After taking this into account, our measurements and an $R_V = 3.1$ O'Donnell reddening law match closely, except in $i-z$, where the O'Donnell reddening law overpredicts reddening dramatically. We find an F99 reddening law provides a good fit to the data, with $R_V = 3.1$ and $N = 0.78$. We recommend the use of this reddening law and normalization for use with SFD and dereddening optical data, or, for SDSS data, the use of the constants

R_{a-b} presented in Table 2.1.

This result largely vindicates the SFD normalization at high Galactic latitudes and low column densities, which had been called into question by earlier studies in dustier regions. Except in $u-g$, where the SDSS system response assumed by SFD was in error, we do not find that SFD overpredicts extinction by 40%. In $g-r$, the closest band to the SFD $B-V$ calibration, our normalization agrees with the SFD normalization within 4%. Extrapolating from the SDSS bands to $B-V$, we find that SFD overpredicts $E(B-V)$ by 14%. However, because the best fit normalization varies over the sky, this result depends on the footprint that we have analyzed, and will be different in other areas. The fit results indicate that the normalization varies between clouds by 10%.

We have also made maps of the R_V and N over the SDSS footprint. However, we do not yet recommend the use of these maps except in regions where the signal-to-noise is high, where we use these values to compute the R_{a-b} covariance matrix. We are actively investigating incorporating similar maps of R_V and N into future dust extinction maps, properly combining them with the available FIR data.

The fact that the best fit normalization of the dust map varies over the sky points to problems with the SFD temperature correction. However, the dust extinction spectrum is relatively stable, indicating that at least in regions with $E(B-V) \lesssim 0.5$, objects can be dereddened in the optical assuming a universal extinction law to within a few percent accuracy.

The blue tip colors, dereddened according to the SFD dust map with the coefficients from this work, show no coherent residuals greater than about 30, 30, 10, and 10 mmag in the footprint we analyze, which covers most of the high-latitude sky. Over much of the sky, residuals are within the statistical uncertainties.

These reddening measurements permit detailed tests of dust maps over a large sky

area and over a range of dust temperatures and column densities. We have been able to find clear signs of shortcomings in the SFD temperature correction. In future work, we plan to construct new dust maps based on dust emission, constrained to best fit these measurements. Future surveys like Pan-STARRS (Kaiser et al., 2002), the Dark Energy Survey (Flaugher, 2005), and the Large Synoptic Survey Telescope (Tyson, 2002) will permit this technique to be used in other bands and to fainter magnitudes with better accuracy, allowing extended wavelength coverage and admitting dustier regions near the Galactic plane to be studied.

2.A Using SFD to Predict Extinction in Specific Clouds

Frequently it is useful to estimate the reddening through a particular cloud for which the reddening law is expected to be different from the Galactic average, as when the cloud has R_V substantially different from three. The correct procedure in such cases is not to use $A_V = R_V E(B-V)_{\rm SFD}$, because in such clouds $E(B-V) \neq E(B-V)_{\rm SFD}$, as SFD is ultimately a map of optical depth at 100 μm, and the ratio of the 100 μm optical depth to $E(B-V)$ is itself a function of R_V.

If the cloud in question has SDSS coverage, the surest footing is to use the measured blue tip colors for that cloud to derive the extinction law in that cloud. If SDSS coverage is not available, extrapolation from SFD or some alternative method is required.

In order to extrapolate from SFD, we have found that the best procedure is to take the SFD prediction for $E(B-V)$ and transform this to a prediction for extinction at 1 μm. This gives $A_{1\ \mu{\rm m}} = 0.78/1.32 \cdot E(B-V)_{\rm SFD}$, where 0.78 is our best fit value for $A_{\rm bluetip,\ F99}/A_{\rm SFD,\ O'D}$ at 1 μm and 1.32 is the ratio $E(B-V)/A_{1\ \mu{\rm m}}$ for an O'Donnell $R_V = 3.1$ reddening law. Next, reddening in any other band can be estimated by

extrapolating from $A_{1\ \mu\mathrm{m}}$ according to an F99 reddening law. Other reddening laws can be used, though they will require constants other than 0.78 in the above equation.

Chapter 3

Measuring Reddening Using the SDSS Spectroscopy

This chapter presents Schlafly & Finkbeiner (2011), which studies the two-dimensional distribution of dust using spectroscopy from the Sloan Digital Sky Survey. It confirms the results of Schlafly et al. (2010) (§2) with an independent data set.

3.1 Introduction

Dust is composed of heavy elements produced by the nuclear burning of stars. These heavy elements are blown out of the stars in winds and explosions, and are reprocessed in the interstellar medium to eventually form dust grains (Draine, 2003). The dust scatters and absorbs light, especially in the ultraviolet through infrared, according to the dust reddening law. The dust also emits photons thermally in the far-infrared. Accordingly, mapping the dust is a central problem in astronomy.

In previous work with the blue tip of the stellar locus (Schlafly et al., 2010, S10), we examined the reddening law and the accuracy of the Schlegel et al. (1998, SFD) dust map using photometry from the Sloan Digital Sky Survey (York et al., 2000, SDSS) and the uniformity of the color of the blue tip of the stellar locus over the sky.

This blue tip work recommended a 14% recalibration of the SFD dust map in the sense that $E(B-V) = 0.86 \cdot E(B-V)_{\rm SFD}$, and a preference for a Fitzpatrick (1999, F99) reddening law over other reddening laws. In this work we set out to test that result using an independent set of data.

The SDSS stellar spectra provide an independent test of reddening. Stellar spectra sensitively test reddening because the broadband photometry of a star is almost completely determined by three parameters: temperature, metallicity, and gravity. These paramaters can be determined using only line information in the spectra, allowing the intrinsic broadband colors of the star to be predicted independently from the observed colors of the star. Dust intervening between us and the star, however, will shift the observed colors relative to the intrinsic colors. The difference between the predicted intrinsic colors and measured colors constitutes a measurement of the reddening to that star. This method is broadly similar to that of Peek & Graves (2010) and Jones et al. (2011), which use SDSS galaxy and M-dwarf spectra, respectively, to similar effect.

The eighth data release of the SDSS has spectra for about 500,000 stars (Aihara et al., 2011). The SEGUE Stellar Parameter Pipeline (Lee et al., 2008a, SSPP) has uniformly processed these spectra to measure the temperature, metallicity, and gravity of each of these stars using a variety of methods, including ones that are independent of the observed colors of the star. We use one such method to predict the intrinsic colors of each star. The difference between the observed colors and intrinsic colors is used as a measurement of reddening to each star. These reddening measurements are then used to test the calibration of SFD and the reddening law.

We test the calibration of SFD and the reddening law by comparing our reddening measurements with the predictions from SFD and a reddening law. A reddening law predicts, in each color $a-b$, the reddening $E(a-b)$ relative to the reddening in some

reference color, usually $B-V$. The SFD dust map predicts $E(B-V)$, effectively giving the normalization of the reddening law in any direction on the sky. We use our reddening measurements to find $R_{a-b} = E(a-b)/E(B-V)_{\rm SFD}$ for each of the SDSS colors, testing both the reddening law and the SFD normalization. We also find the ratios of the R_{a-b}, which test the reddening law without using SFD as a reference.

This work additionally lays the foundation for future investigations of the three-dimensional distribution of dust. Because we have stellar parameters for each of the stars, we can obtain accurate absolute magnitudes and distances. The SDSS targets both blue-horizontal-branch (BHB) stars and M-dwarf stars, in principle permitting the dust to be studied over a wide range of distances. In this work, however, we have focused on the two-dimensional distribution of the dust.

The paper is organized as follows: in §3.2, we present the data sets used in this work. In §3.3, we describe our method for transforming SSPP stellar parameters and SDSS photometry into reddening measurements. In §3.4, the reddening measurements are presented, calibrated, and mapped. In §3.5 and §3.6, we discuss the implications of these results, especially for the reddening law, and conclude.

3.2 Data

To measure the reddening to a star, we require its observed colors and a prediction for its intrinsic colors, as derived from stellar parameters for that star. The SDSS provides all of this information. In this section, we first describe the SDSS imaging, which provides the observed colors, and the SDSS spectroscopy and SSPP, which provide the stellar parameters. We then present the MARCS grid of model atmospheres (Gustafsson et al., 2008), which is used to connect the stellar parameters to colors. Finally, we describe the cuts we perform on the full set of SDSS stars with

spectra to get the sample of stars used in this work.

3.2.1 The SDSS

The eighth data release of the SDSS provides uniform, contiguous imaging of about one third of the sky, mostly at high Galactic latitudes (Aihara et al., 2011). The SDSS imaging is performed nearly simultaneously in five optical filters: u, g, r, i, and z (Gunn et al., 1998; Fukugita et al., 1996). The photometric pipeline has uniformly reduced data for about 10^8 stars. The SDSS is 95% complete up to magnitudes 22.1, 22.4, 22.1, 21.2, and 20.3 in the bandpasses u, g, r, i, and z, which have central wavelengths of about 3600, 4700, 6200, 7500, and 8900 Å. We use SDSS data that have been photometrically calibrated according to the "ubercalibration" procedure of Padmanabhan et al. (2008).

The technique presented here is sensitive to the SDSS photometric calibration, and so we briefly describe the basic units in which the SDSS data is calibrated: the run and camera column ("camcol"). The SDSS takes imaging data in runs that usually last for several hours. These runs observe regions of sky that are long in right ascension and narrow in declination. Each run is composed of observations from six camcols: the six sets of five CCDs (one for each of the photometric bands) that fill the SDSS focal plane.

The SDSS photometry is used to select targets for follow-up SDSS spectroscopy. Spectroscopy is performed with two multiobject double spectrographs, which are fed by 640 fibers. The spectra cover a wavelength range of $3800 - 9200$Å at a resolution of $\lambda/\Delta\lambda \simeq 2000$. The stars used in this work were targeted for spectroscopy either as part of the main SDSS survey or as part of the Sloan Extension for Galactic Understanding and Exploration (Yanny et al., 2009, SEGUE) and its successor, SEGUE-2. Targets from the main survey are observed until they reach a target signal

to noise (S/N) of about $(S/N)^2 > 15$/pix for stars with magnitudes $g = 20.2$, $r = 20.25$, $i = 19.9$. SEGUE targets are exposed long enough to achieve $(S/N)^2 > 100$ at the same depth, so that stellar parameters can be measured (Abazajian et al., 2009).

The SDSS has a number of programs targeting different stellar types for spectra. Figure 3.1 shows a *ugr* color-color plot of the different types of stars used in this work, together with the overall stellar locus. Yanny et al. (2009) gives a detailed description of the criteria that define these targets. The stars used in this work cover most of the stellar locus, except for the reddest stars, for which stellar parameters are poorly measured. Table 3.1 gives the names of each of the programs targeting stars used in this analysis, as well as the number of stars used. In addition to stars targeted for specific science goals, we also use the reddening and spectrophotometric standard star target types. These stars are F stars used for calibration purposes in the SDSS spectroscopic pipeline.

3.2.2 The SSPP

The Sloan Extension for Galactic Understanding and Exploration is a spectroscopic and photometric extension to the SDSS designed to provide insight into the structure and history of the Galaxy (Yanny et al., 2009). As part of this program, the SSPP was developed to uniformly process the stellar spectra from the SDSS (Lee et al., 2008a). This work uses the eighth data release of the SDSS, which includes an updated version of the SSPP, and spectra from SEGUE-2 in addition to SEGUE. The SSPP provides multiple estimates of the spectral type, metallicity, gravity, and radial velocity for all of the stars with SDSS spectra. The accuracy of these parameters has been repeatedly tested by comparison with high resolution spectroscopy and by using measurements from globular and open clusters (Lee et al., 2008b;

Table 3.1. SDSS spectral targets

Target type	# of stars	Description
PHO	15894	Spectrophotometric standards
RED	14353	Reddening standards
SEGUE1_BHB	12603	BHB stars
SEGUE1_FG	5065	FG stars
SEGUE1_GD	44495	G dwarfs
SEGUE1_KD	13459	K dwarfs
SEGUE1_KG	16012	K giants
SEGUE1_LM	22273	low metallicity stars
SEGUE1_LOW_KG	2606	low-latitude K giants
SEGUE1_LOW_TO	6432	low-latitude turn-off stars
SEGUE1_MPMSTO	26885	metal-poor F stars
SEGUE2_LKG	19634	K giants
SEGUE2_LM	13785	low metallicity stars
SEGUE2_MSTO	31767	main sequence turn-off stars
SEGUE2_PMKG	10566	K giants
STAR_BHB	5667	Main survey BHB stars
Total	261496	

Note. — The target types and the number of stars used for stars considered in this work. The low-latitude targets are selected according to targeting algorithms designed to select stars in highly-reddened low Galactic latitude regions. SEGUE-1 (Yanny et al., 2009) and SEGUE-2 provide most of the targets for this work. The main survey, however, provides the STAR_BHB targets, as well as most of the spectrophometric and reddening standards.

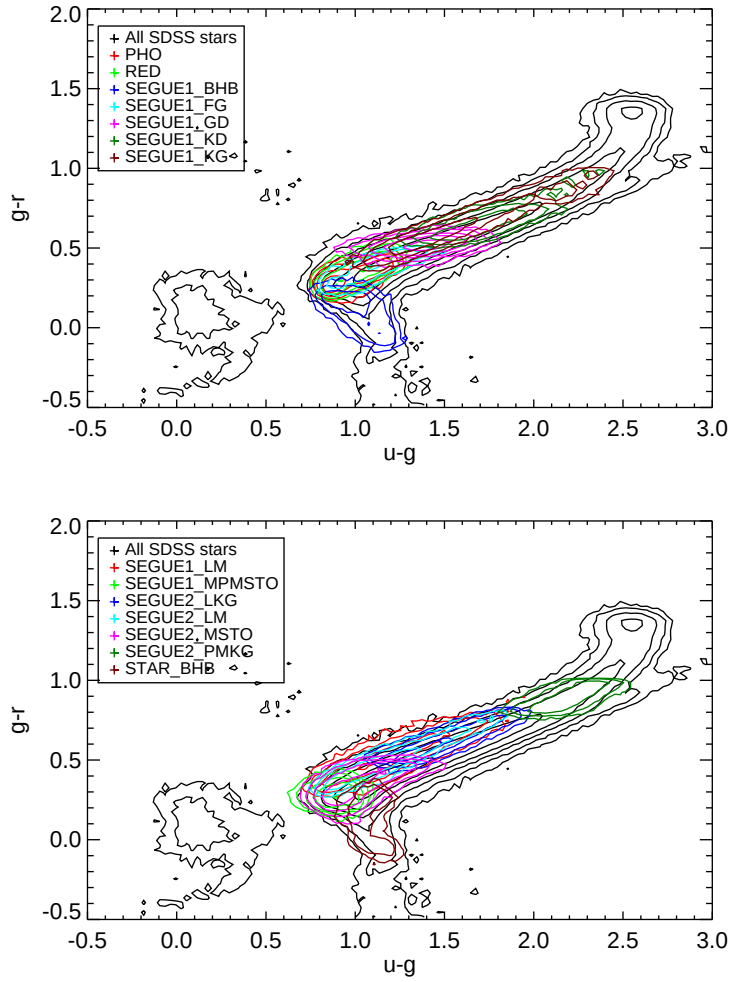

Figure 3.1 Colors of stars with SDSS spectra used in this work. The black contours give the number density of all point sources detected by the SDSS at greater than 20σ confidence in the *ugri* bands. The colored contours give the number densities of stars with SDSS spectra, targeted according to the program labeled in the legend. In each panel the horizontal axis gives $u - g$ and the vertical axis gives $g - r$, in mags; the figure is split to make the contours more legible.

Allende Prieto et al., 2008; Smolinski et al., 2010).

The SSPP provides a number of different estimates for the temperature, metallicity, and gravity of each star, and a single composite estimate. We cannot use the composite estimates produced by the SSPP because some of the SSPP parameter

estimates rely on the photometry of the stars, which is affected by the dust. Instead we rely only on methods that do not make use of any photometry. These are the `NGS1`, `ki13`, `ANNRR`, and `ANNSR` methods (Lee et al., 2008a). For this work we have used the `ANNRR` estimator (Re Fiorentin et al., 2007), which uses a neural net trained on continuum-normalized SDSS spectra to make parameter estimates. However, the four methods produce compatible stellar parameters and the results of this work are insensitive to the method used.

3.2.3 MARCS Model Atmospheres

The stellar parameters derived from the SSPP are transformed into predicted *ugriz* colors using the MARCS grid of model atmospheres (Gustafsson et al., 2008). Each model includes estimates of the surface flux at a resolution of $\lambda/\Delta\lambda$ of 20,000, and covers the range 1,300–200,000 Å. The grid covers an extensive range of stellar parameters: 2500 K $\leq T_{\rm eff} \leq$ 8000 K, $-5 \leq$ [Fe/H] ≤ 1, and $-1 \leq \log g \leq 5.5$, as well as additional parameter combinations involving α-enhancement and microturbulence. Edvardsson (2008) and Plez (2008) have verified the accuracy of synthetic broadband colors predicted from this grid. For $\log g < 3$, we use the MARCS spherical stellar atmosphere models, while for $\log g \geq 3$, we use the plane parallel models. We have experimented with using other grids: the Munari et al. (2005) grid, the Castelli & Kurucz (2004) grid, and the NGS1 grid used internally in the SSPP. The Munari et al. (2005) grid predicts bluer colors than the other grids owing to the grid's not including "predicted lines," faint lines which have not been individually detected (Munari et al., 2005). Nevertheless, because we calibrate the predicted colors to match the observed colors (§3.4.2), our final results are insensitive to the choice of grid, even when the raw predicted colors are substantially discrepant from the observed colors.

3.2.4 Selection Cuts

The SDSS targets a wide variety of stars for spectroscopy, including exotic types for which the spectral parameters are difficult to measure. We are interested in the dust, and so want to select stars for which the stellar parameters are well understood and accurately measured. Accordingly, we exclude from this analysis stars targeted to have unusual colors and very red stars with dereddened $g - r > 1$ mag. Likewise, we exclude any white dwarf targets. Finally, we exclude any objects with stellar parameters marked as unreliable by the SSPP (according the parameters' indicator variables).

The remaining target types and number of stars used in each type are listed in Table 3.1. We find it convenient to occasionally divide these target types into five classes. These classes are the standard stars, which were targeted as reddening standards or spectrophotometric standards; the FG stars, targeted to have spectral types F or G; the BHB stars; the K stars, targeted to have spectral near K; and the other stars, which include the low-metallicity and low-latitude targets.

We have chosen not to impose a cut on the S/N of the spectra. We have varied cuts on S/N from 0 to 50; the resulting best fit reddening coefficients presented in this work vary by only 0.5% in that range.

The total number of stars used following these cuts is 261,496.

3.3 Methods

We predict the colors of stars using the stellar parameters from the SSPP and the MARCS grid. We compare these predicted colors to the measured colors from the SDSS imaging to derive the reddening to each star.

The predicted broadband magnitudes m_b are given by integrating each synthetic

spectrum over the SDSS system throughput for each of the five bands b (Gunn et al., 1998), according to

$$m_b = -2.5 \log \frac{\int d\lambda S(\lambda) W_b(\lambda)}{\int d\lambda Z(\lambda) W_b(\lambda)} \tag{3.1}$$

Here the source spectrum S has units photons/s/Å, the system throughput W_b is unitless, and the AB magnitude reference spectrum Z has the same units as S. The AB magnitude reference spectrum Z is simply a flat spectrum with $F_\nu = 3631$ Jy (Oke & Gunn, 1983).

The magnitude of a source in a single band predicted in this way is not useful because it depends on the unknown radius and distance of the source. However, in this work we consider only colors, for which the distance and radius dependence cancels. We could in principle use the stellar parameters and stellar evolutionary tracks to determine the radius of the star, and so derive distances in conjunction with reddenings, but we defer this to future work.

By computing the magnitudes corresponding to each synthetic spectrum, we construct a synthetic grid of magnitudes. The magnitudes for each star are then predicted by linearly interpolating off this grid. The differences between the measured colors and predicted colors give reddening estimates. We define this reddening measurement in the color $a - b$ to be $\Delta_{a-b} = (a-b)_{\rm obs} - (a-b)_{\rm pre}$.

3.4 Results

The reddening estimates Δ_{a-b} are used to measure the dust reddening law and test dust properties. In this section, we describe the performance of these reddening measurements at high Galactic latitudes (§3.4.1), demonstrating the need for an empirical calibration to improve the measurements. We then perform that calibration (§3.4.2). Finally, we present maps of the calibrated reddening measurements (§3.4.3).

3.4.1 Performance at High Galactic Latitudes

We test the quality of the Δ by restricting to the region of sky with $|b| > 50^\circ$ and $E(B-V)_{\rm SFD} < 0.04$. In this region of low extinction, excursions of Δ from zero should be due primarily to the statistical uncertainties in the photometry and stellar parameters. However, additional systematic effects can cause $\Delta \neq 0$. These include any mismatch between the synthetic spectra and the real spectra and biases in the SSPP-derived stellar parameters.

The performance of Δ for this sample of stars is given in Table 3.2, for several classes of star. The rows marked "raw" give the means and standard deviations of the uncalibrated Δ relevant here. In all colors, the mean Δ is within about 30 mmag of 0, comparable with the 10–20 mmag uncertainty in the SDSS zero points (Abazajian et al., 2004). In $r-i$ and $i-z$, the scatter in Δ is 20–30 mmag, comparable to the SDSS photometric uncertainty.

However, in the colors $u-g$ and $g-r$, the scatter in Δ is somewhat larger than expected. The expected uncertainty in Δ_{u-g} and Δ_{g-r} is about 40 and 30 mmag, respectively, including both the photometric uncertainty and the uncertainty in the stellar parameters. However, the scatter in Δ in this sample of stars is 92 and 51 mmag in the colors $u-g$ and $g-r$. Figure 3.2 (left panels) shows that additionally there are trends in Δ with temperature, metallicity, and gravity, especially in the color $u-g$. Because we expect that typical stellar metallicity is correlated with the dust column to that star, these trends could bias this analysis and must be removed. Moreover, these trends contribute to the scatter in Δ_{u-g} and Δ_{g-r}.

We do not fully understand the source of these trends. The two most likely candidates are mismatches between the synthetic stellar spectra and real stellar spectra, and biases in the SSPP stellar parameters. We have tested for mismatch

Table 3.2. Bias in Predicted Magnitudes

Target class	$\overline{\Delta_{u-g}}$	σ_{u-g}	$\overline{\Delta_{g-r}}$	σ_{g-r}	$\overline{\Delta_{r-i}}$	σ_{r-i}	$\overline{\Delta_{i-z}}$	σ_{i-z}
Standards (raw)	22	51	3	33	28	22	17	25
Standards (cal)	-3	46	-2	31	-1	22	-1	24
FG (raw)	0	82	-2	42	30	28	20	35
FG (cal)	1	72	-2	37	0	27	0	34
BHB (raw)	64	83	-1	50	36	32	33	42
BHB (cal)	24	90	-13	46	0	31	-2	40
K (raw)	10	114	-24	57	29	32	14	32
K (cal)	5	73	4	35	0	27	0	28
Other (raw)	13	88	20	47	34	28	18	31
Other (cal)	-16	68	8	38	3	27	0	30
All (raw)	12	92	-6	51	30	29	18	33
All (cal)	1	71	0	37	0	27	0	31

Note. — The mean ($\overline{\Delta}$) and standard deviation (σ) of Δ in mmag for different types of stars (§3.2.2), before and after calibration (§3.4.2), in each of the SDSS colors. Rows marked "(raw)" or "(cal)" indicate whether the means and standard deviations are given before or after calibration, respectively. After calibration, the mean of Δ is close to zero, and the scatter in Δ is reduced, especially in the color $u - g$.

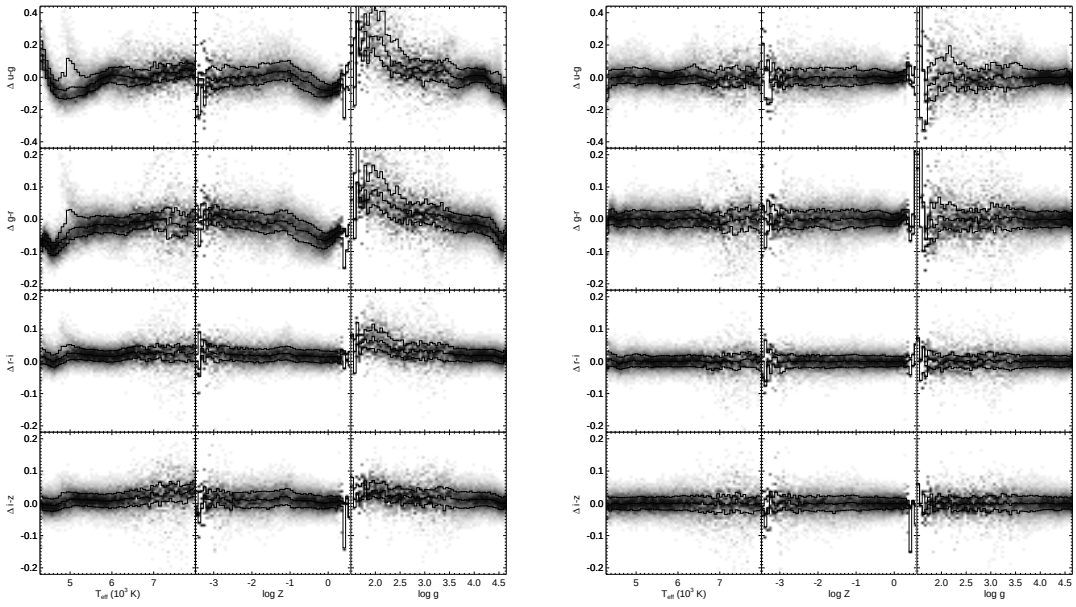

Figure 3.2 Color difference Δ in mags with temperature $T_{\rm eff}$, metallicity $\log Z$, and gravity $\log g$ for the colors $u-g$, $g-r$, $r-i$, and $i-z$. The left hand panels show Δ before calibration, while the right hand panels show Δ after calibration. Before calibration, the $u-g$ color is worst predicted, and small but easily detectable trends with temperature exist for all of the colors. Note the different scale for $u-g$.

between the synthetic and observed spectra by comparing with other synthetic grids. Comparing the grids of Gustafsson et al. (2008), Castelli & Kurucz (2004), and Lee et al. (2008a) indicates that the grids can disagree with one another by about 50 mmag in $u-g$ and $g-r$. The larger effect, however, is probably due to biases in the SSPP stellar parameters. The data release 8 version of the SSPP introduced substantial changes to metallicity estimates for stars around solar metallicity, by about 0.4 dex (Smolinski et al., 2010). Colors predicted using parameters from the data release 7 version of the SSPP were too blue by as much as 200 mmag in $u-g$.

However, we calibrate the predicted colors to remove the trends and to render our results insensitive to these sources of systematic errors. We have repeated the full analysis using four different grids (Gustafsson et al., 2008; Castelli & Kurucz, 2004; Lee et al., 2008a; Munari et al., 2005). The final results of this work were unchanged

at the 1% level. We have also repeated the analysis using the data release 7 and 8 versions of the SSPP, which changed the final results by at most 2%.

3.4.2 Calibration

We remove these trends by calibrating the synthetic photometry so that $\Delta \approx 0$ on the high-latitude sample of stars where reddening is unimportant. This procedure has been done before; for instance, Fitzpatrick & Massa (2005) also calibrate synthetic photometry to match observed photometry. In this work, we perform the calibration by fitting an empirical curve to Δ as a function of temperature, metallicity, and gravity, and adjusting the synthetic photometry to remove this curve from Δ.

To properly model the trends in Δ, we should find the function f of temperature $T_{\rm eff}$, metallicity $\log Z$, and gravity $\log g$ that most accurately predicts the colors. To be more precise, f should be chosen to minimize the distance between Δ and f in color space, considering the covariance matrix for the observed colors and for the predicted colors. We however deemed this computationally intractable and unnecessary, given the wide range of temperatures ($4000\ \ {\rm K} < T_{\rm eff} < 8000\ \ {\rm K}$), metallicities ($-3 < \log Z < 0$), and gravities ($2 < \log g < 5$) available and the small estimated uncertainties in the stellar parameters for the objects we look at ($\sigma_T \lesssim 150$ K, $\sigma_{\log Z} \lesssim 0.1$ dex, $\sigma_{\log g} \lesssim 0.1$ dex). We therefore ignore the covariance between the stellar parameters and Δ, and rely on the fact that the stars cover a broad range of parameters (much broader than the uncertainties in those parameters) to guarantee that the bias introduced by this is small.

To maximize the effective range of stellar parameters, we need to a set of stars for calibration that cover parameter space evenly without overweighting stars of a particular type. Accordingly we choose stars from the *ugr* color plane, capping the maximum number of stars chosen from any location in the plane. This guarantees

that all of the available stars are used in areas of color space where few stars were targeted, but limits the number of stars used in areas where many stars were targeted. The primary consequence of this selection is to reduce the importance of the many SEGUE1_GD targets chosen from a narrow range in temperature.

With this set of stars in hand, we find the function f that minimizes

$$\sum_i \left(\frac{\Delta_{c,i} - f_c(x_i)}{\sigma_{c,i}} \right)^2 \tag{3.2}$$

for each color c, where i indexes over stars, Δ gives the measured color minus the predicted color, and x gives the stellar parameters for the stars. The uncertainty σ is computed from the photometric uncertainty and the uncertainty in the predicted colors derived from the uncertainty in the stellar parameters. The values Δ here are corrected for reddening according to S10, though as $E(B-V)_{\rm SFD}$ is less than 0.04 for this sample this is of little importance. We use for f a fifth order polynomial, though we have also used a second order polynomial with negligible effect on the final results of this work.

Figure 3.2 (right panels) shows that the remaining trends in Δ are small. The rows in Table 3.2 marked "cal" show the means and standard deviations of Δ after calibration for several classes of star. The calibration brings the mean of Δ to zero. The calibration has the additional benefit of reducing the scatter in Δ to be much closer to the expected statistical uncertainty of about 40, 30, 25 and 30 mmag in $u-g$, $g-r$, $r-i$, and $i-z$.

To verify that the final results are insensitive to the details of the calibration, we have varied the order of the polynomial used and the sampling method used to select calibration objects. As long as the order of the polynomial is at least two, we achieve consistent results at the 1% level. The sampling method is similarly unimportant

except in extreme cases where the calibration stars do not cover a satisfactory range of stellar parameters.

3.4.3 Reddening Map

The calibrated measurements of Δ immediately permit the construction of a reddening map, which is shown in Figure 3.3 (left panels). The right panels show the map after correction for dust according to SFD, using the prescription of S10. The derived reddening map agrees well with that found in S10, clearly identifying the same runs with bad zero points in $u - g$ and the SFD-underpredicted region in the northwest of the north Galactic cap. In the Galactic plane, the stars used for the reddening measurements may not be behind the entire dust column, and so it is unsurprising that their reddening is less than that predicted by SFD. Over most of the observed sky, however, the residuals after correction for dust are within the uncertainties.

As pointed out in S10, we again find that the dereddened south is somewhat redder than the dereddened north (§3.5.5). Apart from this trend and the cloud in the northwest, the residual maps are reassuringly flat and reveal no trends in color with Galactic latitude or longitude.

Figure 3.4 shows the residual $g - r$ map of Peek & Graves (2010). This map is compared with our residual $g - r$ map, smoothed to match the 4.5 degree resolution of the Peek & Graves (2010) map. The two maps show several consistent large scale features. Both maps detect the SFD underprediction in the northwest, and additionally find that the southwest of the North Galactic Cap is somewhat redder than the southeast, by about 10 mmags.

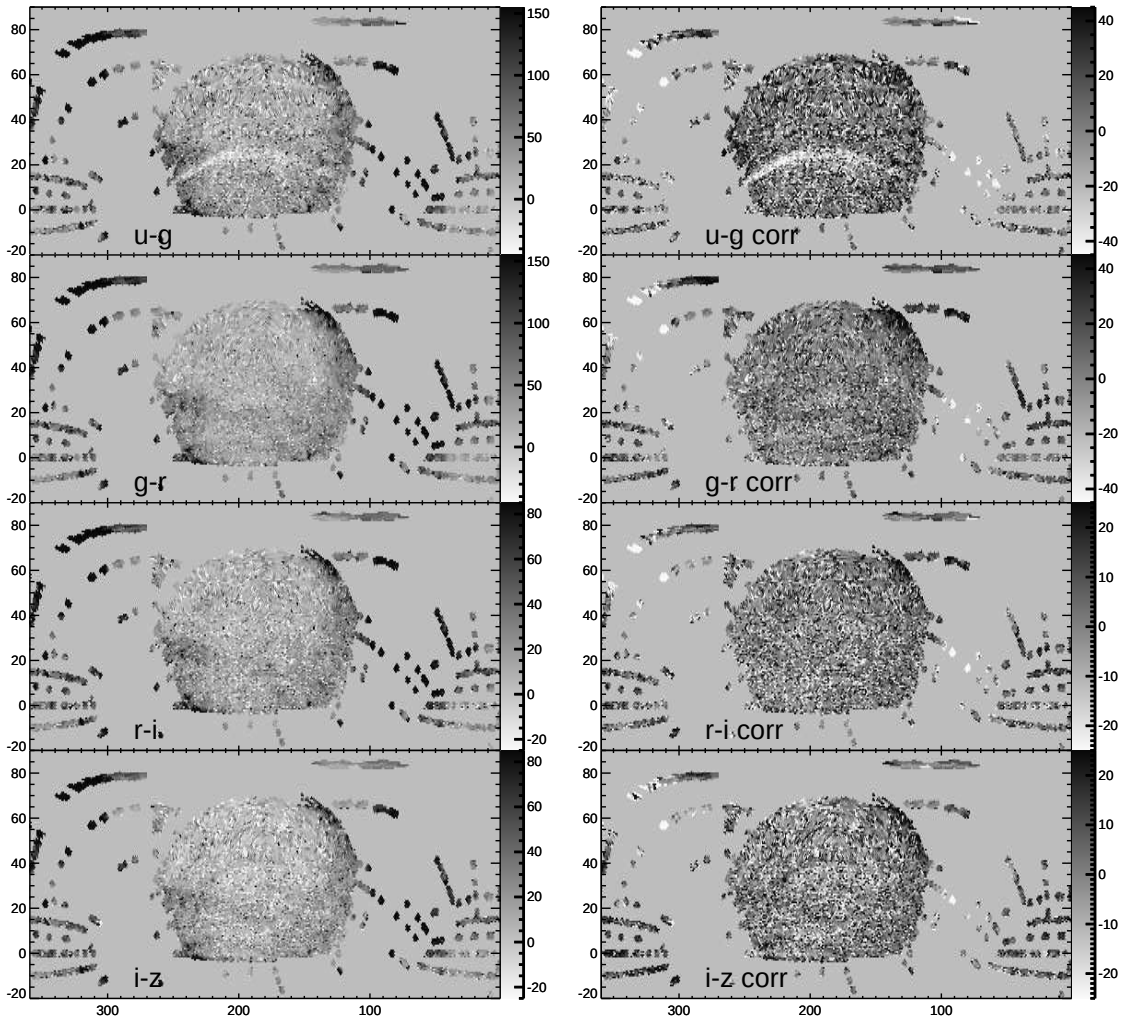

Figure 3.3 Map of Δ in $u-g$, $g-r$, $r-i$, and $i-z$ (left panels), giving the derived reddening to each star targeted by the SDSS. The right hand panels (marked "corr") give the same maps, after correction for the dust according to SFD and the coefficients R_{a-b} from Schlafly et al. (2010). The color bars give the range of Δ in mmag corresponding to the grayscale figure. The horizontal axis is right ascension and the vertical axis is declination, both in degrees.

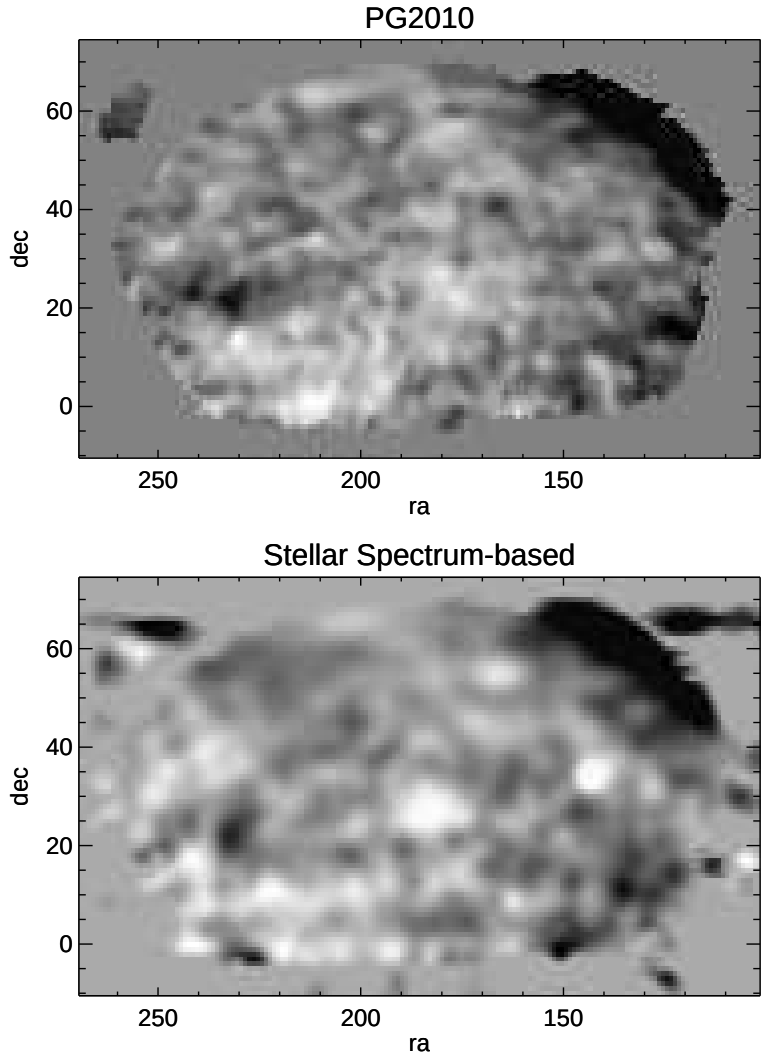

Figure 3.4 Color maps of the North Galactic Cap in $g - r$ after dereddening, from Peek & Graves (2010) and the stellar spectrum-based measurements of this work, smoothed to 4.5°. Some of the same structures are visible. The SFD underpredicted region in the northwest is obvious, but likewise in both sets of reddening measurements the southwest and northeast are redder than the southeast. Both maps are scaled so that black is −10 mmag and white is 10 mmag. Axes give coordinates in right ascension and declination, in degrees.

3.5 Discussion

The reddening measurements Δ permit tests of the reddening law and of the normalization of SFD. In this section we use Δ to measure reddening in the SDSS

colors, simultaneously constraining the normalization of SFD and the reddening law, using two methods. In §3.5.1, we find the best fit values of R_{a-b}, the reddening per unit $E(B-V)_{\rm SFD}$ in each of the SDSS colors. In §3.5.2, we find the best fit values of the ratios of the R_{a-b}, without using SFD. In §3.5.3, we discuss two possible sources of systematic error in the measurements: photometric bias from target selection and the bias introduced by including stars at different distances. In §3.5.4 and §3.5.5, we examine the variation of reddening in different regions of the sky and a curious difference in residuals between the Galactic north and south.

3.5.1 Fitting the Reddening in the SDSS Colors

We use the reddenings Δ to constrain R_{a-b}, the reddening in the color $a-b$ divided by $E(B-V)_{\rm SFD}$. We measure the R_{a-b} by fitting Δ as a linear function of $E(B-V)_{\rm SFD}$, the slope of which gives R_{a-b}. We find that we can detect calibration errors in the SDSS using this technique. Accordingly, we perform a second similar linear fit, where additionally a constant zero point offset in each SDSS run is also fit.

The R_{a-b} are given by the equation

$$\Delta_{a-b} = R_{a-b}E(B-V)_{\rm SFD} + C \tag{3.3}$$

where C gives a constant offset which should give zero if the calibration of the reddening values in the high-Galactic-latitude, low-reddening is accurate when extended over the entire footprint. We find R_{a-b} through least-squares minimization of

$$\chi^2 = \sum_i \left(\frac{\Delta_{a-b,i} - R_{a-b}E(B-V)_{{\rm SFD},i} - C}{\sigma_i} \right)^2 \tag{3.4}$$

where i indexes over stars, R_{a-b} and C are the fit parameters, $E(B-V)_{{\rm SFD},i}$ is $E(B-V)_{\rm SFD}$ in the direction of star i, and σ_i is the uncertainty in $\Delta_{a-b,i}$, considering

both the uncertainty in the measured color and the uncertainty in the predicted color, propagated from the uncertainty in the stellar parameters.

To render the fit insensitive to calibration errors in the SDSS, we also fit

$$\Delta_{a-b} = R_{a-b} E(B-V)_{\rm SFD} + C_r \tag{3.5}$$

in an analogous least-squares sense, where r indexes over SDSS run number, which absorbs any zero point calibration errors in the SDSS runs. We call this the fit with zero point offsets. The results of this fit are similar to those given by Equation 3.3. Each fit is iterated and clipped at 3σ in each color, until finally all clipped points are removed and the fit is repeated with the same clipped set of stars in each color.

The results from the fits are given in Table 3.3. The fits with and without zero point offsets agree to within 4%. Both sets of fits give values consistently slightly smaller than the S10 values ($\sim 4\%$). In S10, we found that the best fit normalization of SFD varied over the sky by about 10%, and so this 4% normalization difference may be due to the different sky footprint available to the S10 and spectrum-based analyses. However, when we tested this at high Galactic latitudes in the north where the two footprints overlapped, the results were inconclusive because the uncertainties were similar in size to the 4% effect we observe. The χ^2 per degree of freedom (χ^2/dof) for the fits are quite good, especially in the redder colors; without including zero point offsets, we achieve 1.45, 1.19, 1.04, and 1.02 χ^2/dof in the colors $u-g$, $g-r$, $r-i$, and $i-z$, respectively.

These results confirm the preference for an $R_V = 3.1$ F99 reddening law and a 14% recalibration of SFD, first reported in S10. The predicted R_{a-b} according to SFD and an O'Donnell (1994) reddening law are in disagreement with the measurements.

Figure 3.5 shows the residuals to the fit without zero point offsets. The residuals

Table 3.3. R_{a-b} derived by fitting SFD

Color	R_{a-b}	χ^2/N	R_{a-b} (zp)	$\chi^2_{\rm zp}/N$	S10	SFD
$u-g$	0.94 ± 0.02	1.45	0.98 ± 0.01	1.41	1.01	1.36
$g-r$	0.98 ± 0.02	1.19	0.94 ± 0.01	1.12	1.00	1.04
$r-i$	0.55 ± 0.01	1.04	0.56 ± 0.01	1.01	0.57	0.66
$i-z$	0.44 ± 0.01	1.02	0.42 ± 0.01	0.97	0.45	0.61

Note. — R_{a-b} derived from fitting SFD. The column R_{a-b} gives the fit results without zero point offsets, while the column R_{a-b} (zp) gives the fit results with zero point offsets. The χ^2 per degree of freedom (χ^2/N) is close to unity in the redder bands, and improves when zero points are fit ($\chi^2_{\rm zp}/N$). The predictions for R_{a-b} according to Schlafly et al. (2010, S10) and the combination of SFD and O'Donnell (1994) are also given. The spectrum-based R_{a-b} are seen to closely match one another and the S10 values, while disagreeing with the prediction according to SFD and O'Donnell (1994).

are largely Gaussian, with σ of 56, 34, 25, and 29 mmag in $u-g$, $g-r$, $r-i$, and $i-z$. This scatter is substantially better than the scatter we achieved in the calibration sample of stars (Table 3.2), because those stars were chosen to be widely distributed over the *ugr* color-color plane and therefore many of those stars had outlying photometry.

The residuals as a function of $E(B-V)_{\rm SFD}$ display a striking trend, shown in Figure 3.6. The residuals increase with $E(B-V)$ for $E(B-V) \lesssim 0.2$, and then decrease thereafter. This result is consistent with the S10 result that the best fit normalization of the dust was larger for $E(B-V) < 0.2$ than it was for $E(B-V) > 0.2$ by about 15%, which is about the size of the trend seen here. That said, the entire $E(B-V) \gtrsim 0.3$ footprint for this analysis occurs in a relatively small area near the Galactic anticenter and a few SEGUE low latitude fields, and may not apply more generally.

The formal statistical uncertainties in the fit results are small (~ 2 parts in a

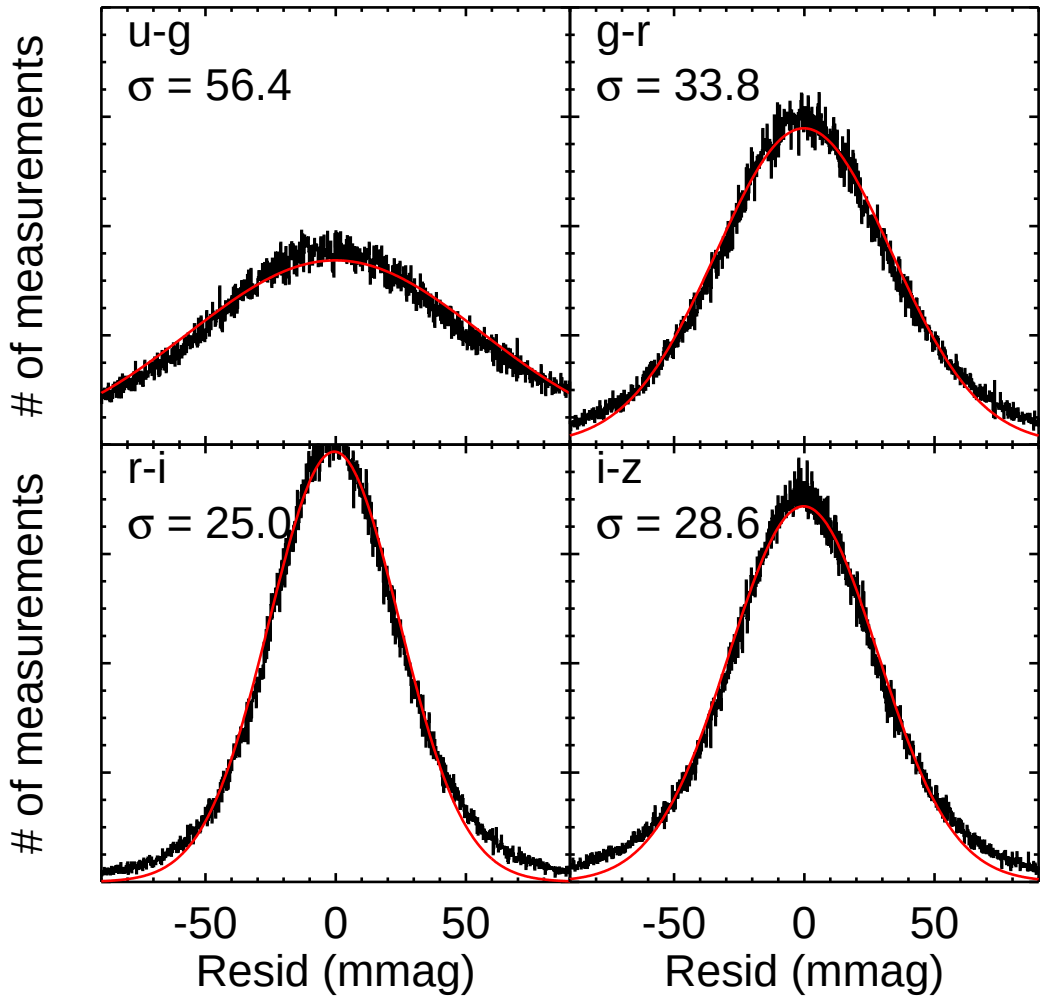

Figure 3.5 The distribution of residuals χ (Equation 3.4) in mmag for the fit without zero point offsets. The residuals are largely Gaussian, though the wings are non-Gaussian and are probably caused by errors in SFD and the changing best-fit dust normalization. A Gaussian fit is overplotted, with standard deviation given by σ in each panel.

thousand). These uncertainties dramatically underestimate the true uncertainty in the fit, stemming from biases in the photometry (§3.5.3), unmodeled calibration errors in the SDSS, and problems with using SFD as a template (S10). The reported

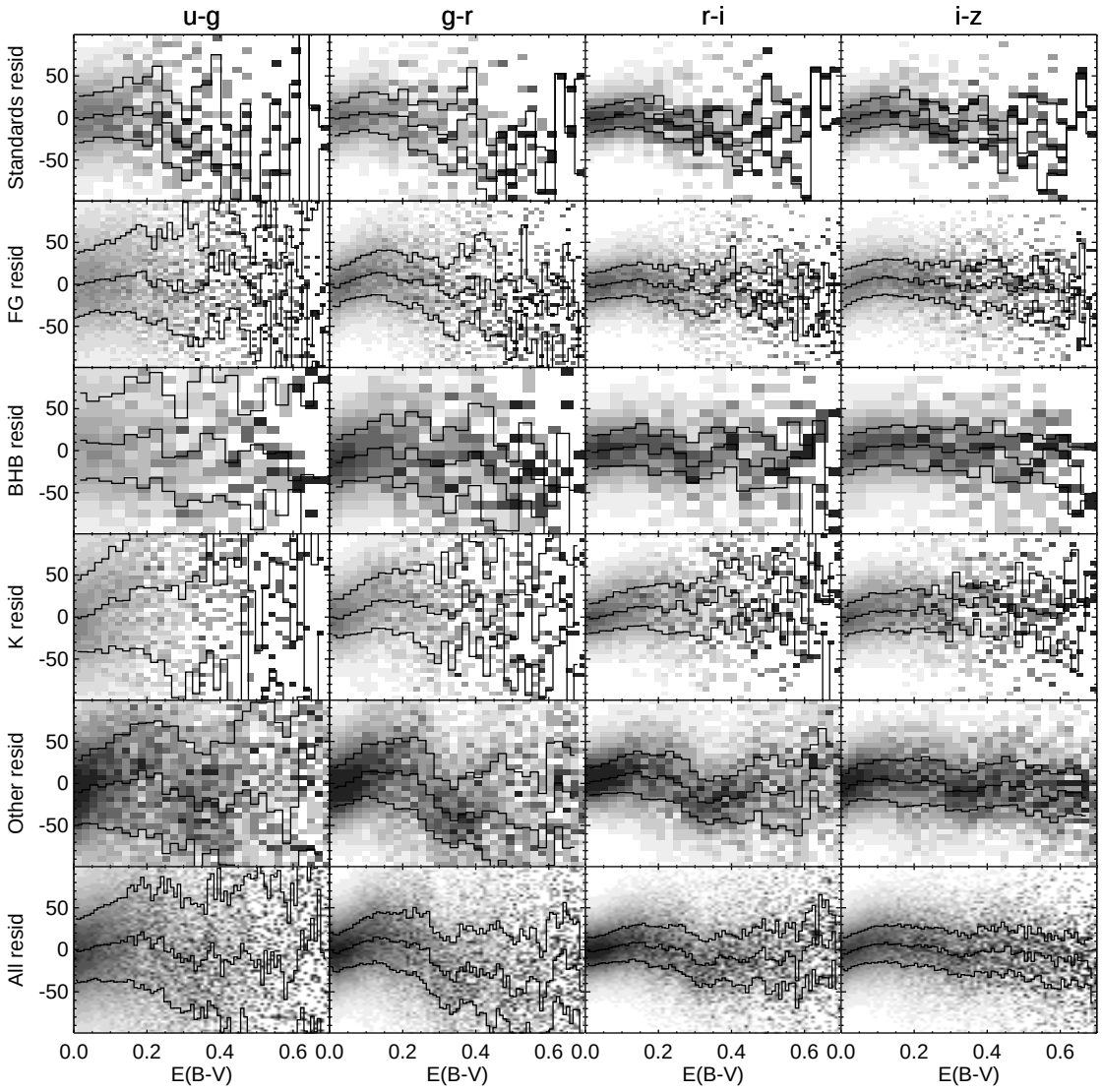

Figure 3.6 Residuals χ (Equation 3.4) in mmag for the fit without run offsets, as a function of $E(B-V)$ in mag. The four columns give the colors $u-g$, $g-r$, $r-i$, and $i-z$. The rows show the residuals for different types of stars: the standard stars, FG-type stars, BHB-type stars, K-type stars, other stars, and all of the stars used in this work. There is a consistent trend in the residuals to increase when $E(B-V) \lesssim 0.2$, and to decrease thereafter.

uncertainties in Table 3.3 are derived by a Monte Carlo simulation with simple models for the calibration errors and SFD template errors. Calibration errors in the SDSS are modeled as normally distributed run zero point errors, with standard

deviations of 20 mmags in u and 10 mmags in g, r, i, and z, according to the estimated calibration uncertainties of Padmanabhan et al. (2008). We additionally allow the true zero point to change by $\dot{a}t$ over the course of the night, where $\dot{a}$ gives the rate of change of zero point and t is the time of night. We choose $\dot{a}$ to be normally distributed with standard deviations of 20 mmags per 6 hours in u and 10 mmags per 6 hours in g, r, i, and z. For the SFD template errors, we multiply SFD by a normalization which varies over the sky on 1 degree scales, with a mean of 1 and standard deviation of 0.1. This is very roughly intended to simulate the uncertainty in the SFD dust temperature correction, but does not include the covariance between temperature and extinction that may be important.

The resulting uncertainties are dominated by uncertainties coming from the calibration effects, with the zero point and change in zero point with time effects contributing similarly.

3.5.2 Fitting Ratios of R_{a-b} using Δ Color-Color Diagrams

We can free the analysis from a dependence on SFD and its normalization by looking only at ratios of R_{a-b}. If Δ has been appropriately calibrated, then in the absence of dust Δ should be consistent with zero. The presence of dust will spread Δ along a line in color-color space. The slope of this line in a pair of colors $a-b$ and $c-d$ gives the ratio R_{a-b}/R_{c-d} and is determined by the reddening law.

We find the best-fit the slope of the line in Δ in color space in a least-squares sense, considering the covariance between the Δ_{a-b} induced by the photometry and the color predictions from the stellar parameters. Figure 3.7 shows the result of this fit, together with the predicted line from S10 and from an O'Donnell (1994) reddening law. Table 3.4 tabulates the best fit parameters for the ratios of R_{a-b}. The fits do a good job at reproducing the S10 ratios for R_{a-b}, but disagree with the O'Donnell

(1994) reddening law predictions. We achieve χ^2/dof of 1.4 on average over all the stars we fit. On the more limited subset of standard stars we get χ^2/dof of 1.1.

An important caveat applies to this analysis. The Δ_{a-b} for a star are correlated. We track the correlation induced by the uncertainty in the photometry and the uncertainty in the stellar parameters. However, any unknown effect that changes the predicted or measured colors of stars will additionally spread out Δ in color-color space, and there is a danger of interpreting that signal as signal from the dust. When instead we fit Δ as a function of $E(B-V)_{\rm SFD}$, we have the advantage of using a template that is uncorrelated with the uncertainties in Δ and that is known to be tightly correlated with the dust.

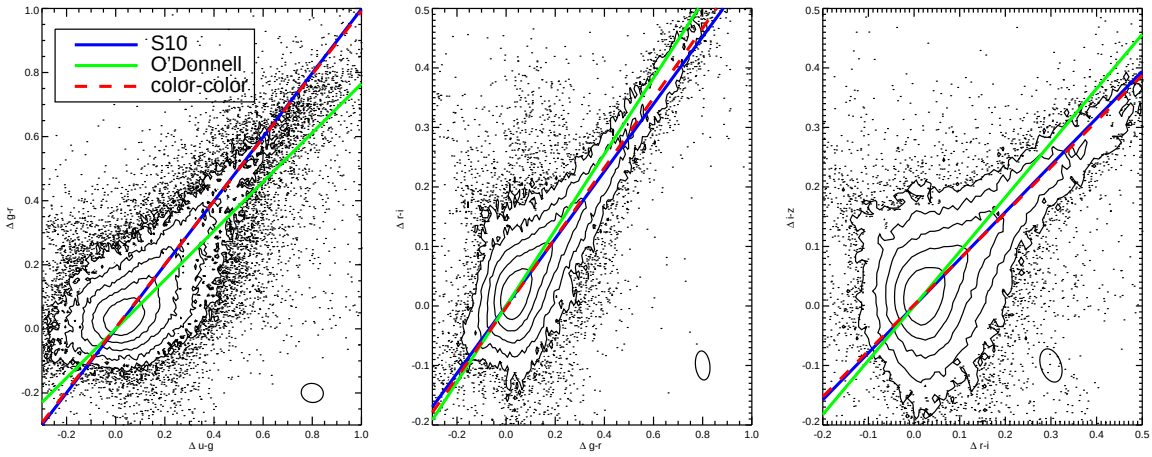

Figure 3.7 Color-color plots of Δ in mag. The data should have Δ consistent with zero in the absence of dust. Reddening from dust spreads Δ along a line given by the reddening law. The predictions for this line for the Schlafly et al. (2010, S10) measurements and for an O'Donnell (1994) reddening law are given by the blue and green lines. The red line is the best fit to the data, and is consistent with the S10 measurements but not with the O'Donnell (1994) prediction. The oval in the lower right of the panels gives a typical uncertainty covariance ellipse for a point on the diagram.

To verify the robustness of these results we have separately fit the standard stars, the F and G stars, the BHB stars, the K stars, and all of the target types we look at.

Table 3.4. Color-color Fit Results

Color	Color-color fit	S10	O'Donnell
R_{g-r}/R_{u-g}	0.99 ± 0.02	1.00	0.77
R_{r-i}/R_{g-r}	0.59 ± 0.02	0.57	0.64
R_{i-z}/R_{r-i}	0.77 ± 0.02	0.79	0.91

Note. — Ratios of R_{a-b} derived from fitting Δ color-color diagrams. The spectrum-based R_{a-b} are seen to closely match the Schlafly et al. (2010, S10) measurement, while disagreeing with the O'Donnell prediction.

The results were consistent at the 3% level.

3.5.3 Sources of Systematic Error

The Photometric Bias

Most SDSS stars are targeted for spectra on the basis of their photometry. Usually stars are targeted for spectra if they fall within a specific box in color space. Photometric uncertainty may scatter stars into the color box preferentially from one side if the box is placed in a region of color space where the gradient in stellar number density with color is different on one side of the box than the other. This effect will lead to a bias in the photometry.

Were this bias a constant for the entire survey it would be taken out by the calibration of Δ. However, most of the SDSS and SEGUE color boxes select stars on the basis of their SFD-dereddened colors. Thus, errors in SFD and its normalization can essentially shift the color box relative to the stellar locus and introduce a bias that changes systematically with $E(B-V)_{\rm SFD}$.

We have analyzed the magnitude of the bias introduced by this effect by simulating

the photometric bias for each of the SDSS and SEGUE target types. We take the SDSS stellar locus at high Galactic latitudes as a proxy for the true stellar locus. Errors are artificially added to the stars' magnitudes consistent with the SDSS estimates for the uncertainties to create a new observed stellar locus. The mean error of a star making it into a color box gives the photometric bias. The change in the photometric bias with $E(B-V)_{\rm SFD}$ can be investigated by shifting the colors of the stars according to the error in $E(B-V)_{\rm SFD}$.

For the target types considered in this work, the photometric bias is less than 0.02 mags, though for very red or unusual types it can be much larger. The potential bias introduced in the derived R_{a-b} is 2%.

The Three Dimensional Footprint

The stars targeted by the SDSS for spectra probe a range of distances. For the dwarf stars in the survey, we use the Jurić et al. (2008) "bright" photometric parallax relation to get approximate distances to stars from their colors. We find that the stars we analyze have distances from 1–6 kpc, with a long tail to greater distances.

The SFD dust map was calibrated to match the reddening of galaxies, which will be behind any dust in the Galaxy. If substantial dust exists beyond the distances probed by the stars in our data, the R_{a-b} found in this work will be less than the true values. However, we find compatible R_{a-b} for the K stars ($\sim$ 1 kpc away) as for the standard stars in the sample ($\sim$ 4 kpc away), indicating that the dust is confined to within 1 kpc over most of the SDSS footprint. In future work we intend to study the three-dimensional distribution of the dust by probing nearer distances with redder stars and by focusing on regions of lower Galactic latitude.

3.5.4 Fits to Different Sky Regions

The Δ are sufficiently numerous and cover a sufficiently large region of the sky that they can be usefully cut into different subsets to study the variation in R_{a-b} over the sky. Figure 3.8 shows the results of such an analysis. The panels show R_{a-b} for different ranges in Galactic latitude, longitude, $E(B-V)_{\rm SFD}$, and dust temperature according to SFD. The rightmost panel shows R_{a-b} as derived for stars observed with each of the SDSS camcols. All R_{a-b} are fit with zero point offsets to minimize sensitivity to calibration errors in the SDSS.

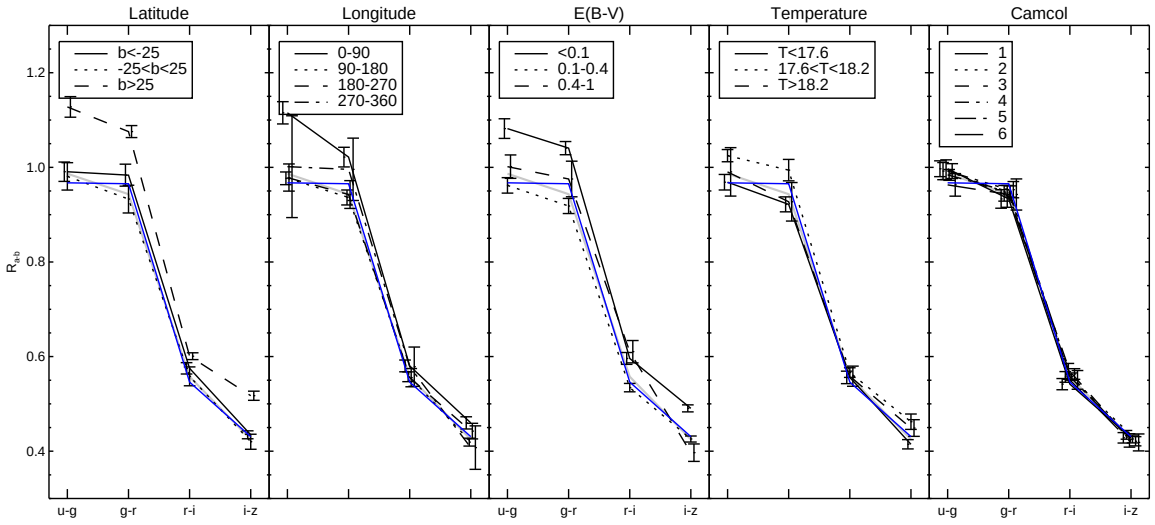

Figure 3.8 R_{a-b} for various subsets of the full data for each of the SDSS colors, using fits with run offsets. Shown are R_{a-b} for the north ($b > 25°$), south ($b < -25°$), and plane ($|b| < 25°$); R_{a-b} for four ranges of Galactic longitude; R_{a-b} for regions of increasing $E(B-V)_{\rm SFD}$; R_{a-b} for regions of different temperature; and finally R_{a-b} for the 6 SDSS camera columns. Overplotted in blue are the Schlafly et al. (2010) values divided by 1.04 (§3.5.1); the thick gray line gives the fit over all the data. Error bars are slightly offset horizontally for legibility. The fitted R_{a-b} are reasonably uniform over the sky, except most noticeably for a 10% normalization difference between the fit results in the Galactic north and south.

The fits results show smaller scatter between the various sky regions. We recover the S10 result that stars with $E(B-V)_{\rm SFD} < 0.1$ prefer a larger normalization than

other stars by $\sim 10\%$; likewise in the north relative to the south, and possibly for the same reason, as the north has less dust than the south. Fits to the dust in different ranges of Galactic longitude and at different temperatures according to SFD are reasonably consistent.

We can get some idea as to whether or not the filter differences between the SDSS camcols are important to this analysis by splitting the survey by camera column. We find very close (2%) agreement between the various camcols. This also serves to place an upper bound on the statistical uncertainty in the measurements.

These results on the universality of the R_{a-b} are consistent with those found in S10. In that work, we did a more detailed analysis of the variation in R_{a-b} over the sky and found the dominant mode of variation in R_{a-b} took the form of an overall 10% variation in the overall normalization of the R_{a-b}. We have not repeated that analysis here, but we try to account for the effects of a 10% normalization variation in our uncertainties (§3.5.1).

3.5.5 North/South Color Asymmetry

In S10, we noted an asymmetry between the north and south in the dereddened color of the main-sequence turn-off, which we called the blue tip color. We were unable to tell whether this color difference was a calibration effect or a result of the south having an intrinsically different blue tip color than the north. Because the spectrum-based reddening measurements are sensitive to calibration problems and not to the intrinsic color of the blue tip, we can use them to break this degeneracy.

Table 3.5 shows the differences in Δ between the Galactic north and south, compared with the blue tip color differences found in S10. We find the offset in Δ for each target class, and report the mean of these offsets in Table 3.5. For the uncertainty in the means, we report the standard deviation of the offsets. The color

Table 3.5. Color difference between North and South

Method	$u-g$	$g-r$	$r-i$	$i-z$
Spectrum	2.3 ± 7.2	8.8 ± 1.5	3.4 ± 1.9	9.3 ± 1.6
Blue tip	7.6	21.8	7.2	12.4

Note. — Median color difference in mmag between the north and south, for $40 < |b| < 70$, using the spectrum-based and blue tip methods for measuring colors. A calibration or dust effect will create a color difference in both sets of measurements, while the presence of a stellar structure in the south would create a color difference only in the blue tip measurements. The blue tip offsets in $r-i$ and $i-z$ are similar to those in the spectrum-based measurements, suggesting that these color differences do not come from a stellar structure. However, in $g-r$, the color difference could indicate different stellar populations in the north and south. In $u-g$, systematic uncertainty in the offsets prevent determination of whether the offset comes from calibration or is astronomical.

differences are comparable in $r-i$ and $i-z$, suggesting that calibration errors in the SDSS are the source of the discrepancy in these colors. In $g-r$, however, the blue tip color differences are larger than the spectrum-based differences. In $u-g$, the uncertainty is too large to make any definitive statement. The difference in these colors could then be caused by a fundamentally different blue tip color in the north than in the south. This result is heartening because the color of the blue tip varies due to age and metallicity changes in stellar populations, which should primarily affect the $u-g$ and $g-r$ colors while leaving the $r-i$ and $i-z$ colors unchanged.

3.6 Conclusion

The SDSS provides a wealth of information for testing reddening. Using the SSPP stellar parameters, our spectrum-based technique achieves reddening measurements

with empirical uncertainties of 56, 34, 25, and 29 mmag in the colors $u-g$, $g-r$, $r-i$, and $i-z$, comparable with the expected uncertainties from the photometry and stellar parameters. Spectra of a few blue stars on a sight line are sufficient to tightly constrain reddening provided that well-calibrated photometry is available and that enough spectra are available to calibrate the predicted colors to the measured colors.

The use of individual stars with spectra additionally allows extinction to be studied as a function of distance. Stellar spectra permit good estimates of the intrinsic luminosity of a star in addition to its reddening, making three-dimensional studies of the dust feasible. The wide range of SEGUE target types—M and K dwarfs through BHB stars—will likely make such analyses especially fruitful, at least at low Galactic latitudes where all of the stars are not behind the entire dust column. At high Galactic latitudes, we could in principle use large numbers of stars to test for reddening through intermediate and high-velocity clouds. We defer to later work the attempt to extend this analysis into the third dimension, having established the feasibility and accuracy of the method in two dimensions. The combination of large photometric and spectroscopic surveys like Pan-STARRS (Kaiser et al., 2002) and LAMOST (Su et al., 1998) seems particularly promising.

These tests should also provide useful feedback to models of synthetic spectra and to stellar parameter estimates. We look forward to incorporating the DR8 version of the SSPP into this analysis, and potentially pairing it with alternative synthetic spectral grids. However, we note that while this analysis provides an effective test of the colors predicted by synthetic spectral grids, nevertheless it does not depend on the accuracy of these colors. The wide range of spectral types targeted by the SDSS permits the predicted colors to be well calibrated to the observed colors, rendering the final results independent of the color accuracy of the synthetic spectra.

The spectrum-based reddening measurements give best-fit R_{a-b} that closely agree

with the S10 values. Accordingly, we have gained confidence in the F99 reddening law with $R_V = 3.1$ and normalization $N = 0.78$ proposed in S10. The variation in the best-fit normalization of the reddening law seen in that analysis remains a problem. The spectrum-based reddening tests permit the variation in best-fit normalization with extinction to be seen more clearly; when $E(B-V)_{\rm SFD} \lesssim 0.2$, the best-fit normalization is about 15% higher than when $E(B-V) \gtrsim 0.2$, though this conclusion relies on the relatively small fraction of the sky where $E(B-V) \gtrsim 0.3$ and SDSS data is available.

Nevertheless, the agreement of the S10 and spectrum-based reddening measurements demands that the F99 reddening law be used to predict reddening over Cardelli et al. (1989) or O'Donnell (1994) reddening laws. Appendix 3.6 gives the extinction per unit $E(B-V)_{\rm SFD}$ predicted by these sets of measurements in 88 bandpasses for 4 values of R_V. We have focused on high Galactic latitudes where we observe $R_V = 3.1$; other values of R_V are provided only for convenience. Because we have seen that the best fit reddening law normalization varies over the sky and as a function of $E(B-V)_{\rm SFD}$, it is possible that outside the SDSS footprint a different normalization might be preferable. However, the shape of the reddening law seems constant over the SDSS footprint, and the normalization we suggest is unambiguously the best choice over the large area of sky covered by the SDSS. Therefore we propose that this reddening law and normalization become the default choice to be used in the absence of other information.

Multiple sensitive, mutually consistent measurements of reddening over the SDSS footprint are now available. Extension of this work to larger areas of sky seems readily possible as Pan-STARRS and LAMOST data become available. These measurements will permit a next generation dust map to be constructed and tested. We defer to future work the construction of a new dust map that incorporates the

insight gained from these measurements.

David Schlegel suggested using SDSS stellar spectra to measure reddening several years ago, and his encouragement and advice were invaluable at the inception of this project.

3.A Extinction in Different Bandpasses

The spectrum-based reddening measurements, in concert with these and the Schlafly et al. (2010, S10) reddening measurements, demand that the colors of high latitude stars with $E(B-V) < 1$ be dereddened with an $R_V = 3.1$ F99 reddening law rather than an O'Donnell (1994) reddening law. The F99 predictions for R_{a-b} agree with the blue tip values to within 3% in $g-r$, $r-i$, and $i-z$, and are off by 6% in $u-g$. This agreement is sufficiently good that we have confidence that reddening in non-SDSS bands can reliably be predicted according to the F99 reddening law. Accordingly, we have tabulated the reddening per unit $E(B-V)_{\rm SFD}$ for a large number of commonly used bandpasses (Table 3.6).

For this computation, following the notation of SFD, we compute

$$\Delta m_b = -2.5 \log \left[\frac{\int d\lambda W_b(\lambda) S(\lambda) 10^{-A(\lambda) \Delta m_{1\mu\rm m}/2.5}}{\int d\lambda W_b(\lambda) S(\lambda)} \right] \tag{3.6}$$

where W is the system throughput for the band b, the source spectrum is S in photons/Å/s, A is the extinction law, normalized so $A_{1\ \mu\rm m} = 1$, and $\Delta m_{1\ \mu\rm m}$ is N times the extinction at 1 μm according to SFD, following the $R_V = 3.1$ O'Donnell extinction law assumed by SFD. The factor N here serves as a normalization factor; we use $N = 0.78$ following the results of S10.

The extinction law is parameterized by $R_V = A_V / E(B-V)$. We have tabulated

$\Delta m_b/E(B-V)_{\rm SFD}$ for $R_V = 2.1$, 3.1, 4.1, and 5.1, in the limit that $E(B-V)_{\rm SFD}$ is small. The traditional value of R_V in the diffuse interstellar medium is 3.1 (Cardelli et al., 1989), which is also what we observe in this work. Values of R_V other than 3.1 are included in the table only for convenience.

For the source spectrum, we use for $S(\lambda)$ a synthetic spectrum from Munari et al. (2005), with $T_{\rm eff} = 7000$ K, $\log Z = -1$, and $\log g = 4.5$.

We tabulate values of $\Delta m_b/E(B-V)_{\rm SFD}$ for the filters considered by SFD, using the F99 reddening law. For the Landolt $UBVR_{KC}I_{KC}$, CTIO $UBVR_{KC}I_{KC}$, Strömgren $ubv\beta y$, Gunn $griz$, Spinrad R_S, UKIRT $JHKL'$, and HST WFPC2 bandpasses we follow the procedure detailed in the SFD appendix, combining the filter response with the optical and detector throughput as well as the atmospheric transparency at the usual site. The SFD appendix used estimated filters for the SDSS from 1994; we now use updated curves taken in June 2001.

The values of $\Delta m_b/E(B-V)_{\rm SFD}$ incorporate a few other changes relative to those in SFD. The CTIO atmosphere model SFD used cut off at 3200Å, slightly affecting the predicted $\Delta m_b/E(B-V)_{\rm SFD}$ in blue bands using that model. The source spectrum was also spuriously multiplied by a factor of λ, for W_b for which SFD did not use a separate detector efficiency curve (UKIRT, Gunn, SDSS, WFPC2, and DSS filter systems). These shortcomings have been corrected.

We additionally tabulate $\Delta m_b/E(B-V)_{\rm SFD}$ for new filter sets that have come to prominence since 1998. We have added values of $\Delta m_b/E(B-V)_{\rm SFD}$ for the PS1 filter complement, using the throughput measurements from Stubbs et al. (2010a), and for the LSST target filter complement, using the "baseline" expected throughput, downloaded from the LSST public SVN repository (Tyson, 2002). Finally, we have computed $\Delta m_b/E(B-V)_{\rm SFD}$ for the wide pass filters available to the Hubble Space Telescope's WFC3 and ACS detectors, using the STSDAS package. STSDAS is a

product of the Space Telescope Science Institute, which is operated by AURA for NASA.

The Munari et al. (2005) synthetic spectra cover the wavelength range 2500Å $-$ 10500Å. This means that values of $\Delta m_b/E(B-V)_{\rm SFD}$ for bandpasses that cover regions outside this range use extrapolated source spectra. We extrapolate into the infrared following a blackbody spectrum ($S(\lambda) \propto \lambda^{-3}$), which is more blue than the typical spectrum and so biases the $\Delta m_b/E(B-V)_{\rm SFD}$ somewhat high. This affects the UKIRT $JHKL'$ and HST F105W, F110W, F125W, F140W, and F160W filters. The effect is small, however: compared to an $S(\lambda) \propto \lambda^{-1}$ spectrum, $\Delta m_b/E(B-V)_{\rm SFD}$ is about 1% larger for the UKIRT filters.

The CTIO atmospheric transparency spectrum used for the CTIO and Landolt filters cuts off in the blue at 3200Å. Blueward of this cutoff we extrapolate that the transmission is constant, rendering the transmitted spectrum too blue and deriving $\Delta m_b/E(B-V)_{\rm SFD}$ somewhat too large. This affects only the CTIO and Landolt U bands.

Table 3.6. F99 Reddening in Different Bandpasses

Bandpass	$\lambda_{\rm eff}$	R_V				Bandpass	$\lambda_{\rm eff}$	R_V			
		2.1	3.1	4.1	5.1			2.1	3.1	4.1	5.1
Landolt U	3508.2	5.614	4.334	3.773	3.460	WFPC2 F300W	3087.6	6.777	4.902	4.127	3.710
Landolt B	4329.0	4.355	3.626	3.290	3.096	WFPC2 F450W	4587.0	4.014	3.410	3.132	2.971
Landolt V	5421.7	2.953	2.742	2.645	2.589	WFPC2 F555W	5439.4	2.976	2.755	2.653	2.594
Landolt R	6427.8	2.124	2.169	2.189	2.201	WFPC2 F606W	5984.8	2.469	2.415	2.389	2.375
Landolt I	8048.4	1.410	1.505	1.548	1.573	WFPC2 F702W	6887.9	1.850	1.948	1.994	2.020
CTIO U	3733.9	5.170	4.107	3.628	3.355	WFPC2 F814W	7940.0	1.452	1.549	1.594	1.620
CTIO B	4308.9	4.382	3.641	3.300	3.104	WFC3 F105W	10438.9	0.981	0.969	0.964	0.961
CTIO V	5516.6	2.857	2.682	2.600	2.553	WFC3 F110W	11169.7	0.907	0.881	0.870	0.863
CTIO R	6520.2	2.055	2.119	2.149	2.166	WFC3 F125W	12335.5	0.778	0.726	0.701	0.687
CTIO I	8006.9	1.420	1.516	1.561	1.587	WFC3 F140W	13692.3	0.672	0.613	0.586	0.570
UKIRT J	12482.9	0.764	0.709	0.684	0.669	WFC3 F160W	15258.3	0.570	0.512	0.485	0.469
UKIRT H	16588.4	0.502	0.449	0.425	0.411	WFC3 F200LP	5515.2	3.457	2.958	2.743	2.625
UKIRT K	21897.7	0.331	0.302	0.288	0.280	WFC3 F218W	2248.3	12.405	7.760	5.956	5.027
UKIRT L'	37772.5	0.159	0.153	0.150	0.148	WFC3 F225W	2394.0	10.907	6.989	5.458	4.666
Gunn g	5200.0	3.225	2.914	2.770	2.687	WFC3 F275W	2742.5	7.986	5.487	4.488	3.963
Gunn r	6628.5	1.959	2.055	2.099	2.125	WFC3 F300X	2934.5	7.437	5.228	4.331	3.854
Gunn i	7898.6	1.454	1.555	1.601	1.628	WFC3 F336W	3366.4	5.835	4.453	3.853	3.519
Gunn z	9050.1	1.188	1.234	1.255	1.267	WFC3 F350LP	5877.1	2.876	2.624	2.509	2.443
Spinrad R_S	6927.3	1.810	1.921	1.972	2.002	WFC3 F390W	3994.8	4.803	3.896	3.481	3.244
Strömgren u	3510.0	5.539	4.305	3.759	3.452	WFC3 F438W	4335.3	4.347	3.623	3.288	3.095
Strömgren b	4670.5	3.916	3.350	3.089	2.938	WFC3 F475W	4785.0	3.755	3.248	3.013	2.878
Strömgren v	4119.2	4.619	3.793	3.411	3.191	WFC3 F475X	4969.7	3.548	3.116	2.917	2.803
Strömgren β	4861.3	3.655	3.183	2.966	2.840	WFC3 F555W	5302.8	3.135	2.855	2.726	2.652
Strömgren y	5478.9	2.862	2.686	2.605	2.557	WFC3 F600LP	7362.3	1.688	1.781	1.824	1.849
SDSS u	3586.8	5.419	4.239	3.715	3.419	WFC3 F606W	5868.5	2.581	2.488	2.445	2.421
SDSS g	4716.7	3.843	3.303	3.054	2.910	WFC3 F625W	6225.8	2.230	2.259	2.273	2.281
SDSS r	6165.1	2.255	2.285	2.300	2.308	WFC3 F775W	7630.9	1.533	1.643	1.694	1.724
SDSS i	7475.9	1.583	1.698	1.751	1.782	WFC3 F814W	7983.1	1.441	1.536	1.580	1.605
SDSS z	8922.9	1.211	1.263	1.286	1.300	WFC3 F850LP	9149.7	1.168	1.208	1.226	1.237

Table 3.6—Continued

Bandpass	$\lambda_{\rm eff}$	R_V 2.1	3.1	4.1	5.1	Bandpass	$\lambda_{\rm eff}$	R_V 2.1	3.1	4.1	5.1
DSS-II g	4620.6	3.970	3.381	3.110	2.954	ACS clear	6211.1	2.612	2.436	2.356	2.309
DSS-II r	6545.5	1.991	2.088	2.133	2.159	ACS F435W	4348.3	4.330	3.610	3.278	3.087
DSS-II i	8111.0	1.396	1.487	1.530	1.554	ACS F475W	4760.3	3.787	3.268	3.028	2.890
PS1 g	4876.7	3.634	3.172	2.958	2.835	ACS F550M	5581.0	2.754	2.620	2.558	2.522
PS1 r	6200.1	2.241	2.271	2.284	2.292	ACS F555W	5361.3	3.031	2.792	2.682	2.618
PS1 i	7520.8	1.568	1.682	1.734	1.765	ACS F606W	5901.0	2.555	2.471	2.431	2.409
PS1 z	8665.3	1.258	1.322	1.352	1.369	ACS F625W	6298.1	2.171	2.219	2.241	2.254
PS1 y	9706.3	1.074	1.087	1.094	1.097	ACS F775W	7673.5	1.520	1.629	1.679	1.708
PS1 w	6240.8	2.425	2.341	2.302	2.280	ACS F814W	8012.4	1.432	1.526	1.569	1.594
LSST u	3693.2	5.243	4.145	3.652	3.373	ACS F850LP	9007.5	1.196	1.243	1.265	1.277
LSST g	4797.3	3.739	3.237	3.006	2.872	DES g	4796.6	3.739	3.237	3.006	2.872
LSST r	6195.8	2.245	2.273	2.286	2.294	DES r	6382.6	2.113	2.176	2.205	2.221
LSST i	7515.3	1.571	1.684	1.737	1.767	DES i	7769.0	1.490	1.595	1.644	1.672
LSST z	8664.4	1.259	1.323	1.353	1.370	DES z	9108.2	1.175	1.217	1.236	1.247
LSST y	9710.3	1.075	1.088	1.094	1.098	DES Y	9850.4	1.051	1.058	1.061	1.063

Note. — $A_b/E(B-V)_{\rm SFD}$ in different bandpasses b, evaluated according to an F99 reddening law with normalization $N = 0.78$ and $R_V = 2.1$, 3.1, 4.1, and 5.1, using a 7000 K source spectrum. The column $\lambda_{\rm eff}$ gives the throughput-weighted mean wavelength in the bandpass. When used with $R_V = 3.1$, these give the coefficients to use with $E(B-V)_{\rm SFD}$ to get reddenings consistent with the results of this work and Schlafly et al. (2010). The values for other R_V are provided only for convenience.

Chapter 4

Photometric Calibration of the Pan-STARRS1 Survey

This chapter presents Schlafly et al. (2012), which describes the photometric calibration of the Pan-STARRS1 survey. We achieve about 1% calibration accuracy over the survey footprint in all bands, enabling a variety of Pan-STARRS1 science. For our purposes, it enables three-dimensional studies of the dust in the Galactic plane, which we discuss in §5.

4.1 Introduction

A central problem in astronomy is relating the number of photons recorded at a detector to the physical flux of photons emitted from a source. This relation depends on important astrophysical parameters, like the distance and Galactic extinction to the source, as well as more ephemeral, local phenomena like the weather at the telescope and the sensitivity of the detector. The problem of photometric calibration is to characterize these latter phenomena to render more universal the detected astronomical phenomena.

Current surveys require photometric calibration as accurate as possible, ideally better than the percent level. Uncertainties in the photometric calibration can prove

a limiting factor in our understanding of the clustering of galaxies on large angular scales (Ross et al., 2011) and in our knowledge of the Galactic extinction at high Galactic latitudes (Schlafly & Finkbeiner, 2011).

The photometric calibration of optical data is often performed by comparing multiple observations of the same sources for large sets of sources and demanding that their fluxes not change over time. This is the same technique used to calibrate cosmic microwave background and radio data, and it has been extensively used in optical astronomy, e.g. Maddox et al. (1990), Honeycutt (1992), Fong et al. (1992, 1994), Glazebrook et al. (1994), and Magnier et al. (1992). In the Sloan Digital Sky Survey (York et al., 2000, SDSS), Padmanabhan et al. (2008) applied this technique and achieved a photometric calibration accurate at the 1% level.

Often surveys and observations have been calibrated using repeat observations of a small number of fields of standard stars, e.g., the 2 Micron All Sky Survey (Skrutskie et al., 2006). These calibration observations determine the relation between flux and photon-count when the fields are observed, and the relation during science observations is extrapolated from them. In the SDSS, however, each set of observations was made to slightly overlap other observations, and the network of these overlaps was used to simultaneously calibrate all of the SDSS observations. Upcoming optical wide-area surveys like PS1, DES, and LSST plan to improve upon this technique by tremendously increasing the number of multiply-observed stars; each plans to image their entire survey area several times. The dense overlapping regions of these upcoming surveys should yield a much more tightly constrained photometric calibration.

In this work, we describe our application of the Padmanabhan et al. (2008) photometric calibration algorithm to the first 1.5 years of PS1 survey data. This paper is organized as follows: in Section §4.1.1, we describe the PS1 survey and its

current status. Section §4.2 describes the photometric calibration algorithm and its application to PS1 data. Section §4.3 gives the results of our calibration of the PS1 data, and the results of the tests used to verify the calibration. In §4.4, we discuss the stability of the PS1 system and the atmosphere in light of these results. Finally, in Section §4.5 we summarize, mention prospects for the future, and conclude.

4.1.1 The Pan-STARRS1 System and Surveys

The Pan-STARRS1 system is a wide-field optical imager devoted to survey operations (Kaiser et al., 2010). The telescope has a 1.8 meter diameter primary mirror, located on the peak of Haleakala on Maui (Hodapp et al., 2004). The site and optics deliver a point spread function with a full-width at half-maximum (FWHM) of about one arcsecond, over a seven square degree field of view. The focal plane of the telescope is equipped with the Gigapixel Camera 1 (GPC1), an array of 60 4800×4800 orthogonal transfer array (OTA) CCDs (Tonry & Onaka, 2009; Onaka et al., 2008). Each OTA CCD is further subdivided into an 8×8 array of independently-addressable detector regions which are individually read out by the camera electronics through their own on-chip amplifier.

Most of the PS1 observing time is dedicated to two surveys: the 3π survey, a survey of the entire sky north of declination $-30°$, and the medium-deep (MD) survey, a deeper, many-epoch survey of 10 fields, each 7 deg^2 in size (Chambers, in preparation). Each survey is conducted in five broadband filters, denoted $g_{\rm P1}$, $r_{\rm P1}$, $i_{\rm P1}$, $z_{\rm P1}$, and $y_{\rm P1}$, that together span 4000–10500Å. These filters are similar to those used in the SDSS, except the $g_{\rm P1}$ filter extends 20 nm redward of $g_{\rm SDSS}$ while the $z_{\rm P1}$ filter is cut off at 920 nm. The $y_{\rm P1}$ filter covers the region from 920nm to 1030nm with the red limit largely determined by the transparency of the silicon in the detector. These filters, and the absolute calibration of the PS1 system using these

filters, are described in Stubbs et al. (2010b) and Tonry et al. (in preparation).

The PS1 images are processed by the Pan-STARRS1 Image Processing Pipeline (IPP) (Magnier, 2006). This pipeline performs automatic bias subtraction, flat fielding, astrometry (Magnier et al., 2008), photometry (Magnier, 2007), and image stacking and differencing for every image taken by the system. The approximately one trillion pixels per night are processed in a massively parallel fashion at the Maui High Performance Computer Center.

The 3π survey is executed so that each time a patch of sky is visited, it is observed for about 40 seconds twice, at times separated by an interval of about 15 minutes (Chambers, in preparation). The two observations make a transit-time-interval (TTI) pair. These observations are used primarily to search for high proper-motion Solar System objects. Each year, the field is then observed a second time in the same filter with an additional TTI pair of images, making for four images of each part of the sky, per year, in each of the 5 PS1 filters. The MD observations consist of 8, much longer, ~ 200 second exposures, dithered in both position and position angle.

The data used in this analysis were taken primarily between February 12, 2010 and June 19, 2011, though a small amount of data from as early as June 20, 2009 is included. Figure 4.1 shows the number of times each part of the sky was observed during this period. The left panel gives the total number of times the sky was observed, while the right panel gives the number of times the sky was observed in photometric conditions (§4.2.3). The median number of times each part of the sky was observed in photometric weather is 4 in each band. This makes for two independent TTI pairs of observations, on average, of each part of the sky, though Figure 4.1 makes clear that this coverage is variable, and the sky around right ascension 100° is covered only by one TTI pair of observations or not at all in $gri_{\rm P1}$. The MD fields have been observed much more often; 100–300 times in $griz_{\rm P1}$, and

about 100 times in $y_{\rm P1}$.

4.2 Methods

Like all CCD-equipped telescopes, PS1 ultimately records the number of photons received from objects it targets[1]. The number of photons recorded depends on:

1. the transparency of the night sky toward the object,
2. the throughput of the detector, filter, and optics, and
3. the size and reflectivity of the telescope mirror.

The object of the photometric calibration is to convert the measurements of the number of photons recorded by the system to measurements of the incident flux from the object, eliminating the signatures of the instrument and atmosphere. The calibration can be divided into two separate procedures, as described in Padmanabhan et al. (2008): the relative photometric calibration, in which the differences in system throughput from observation to observation are removed, and the absolute photometric calibration, in which the number of photons recorded for some particular configuration of the telescope is converted to a magnitude on the AB magnitude system, which is based on physical units of flux (Oke & Gunn, 1983). This paper presents the relative calibration of the Pan-STARRS1 system; the absolute calibration is described in Tonry et al. (in preparation). Given an absolute flux calibration for a single star, the relative calibration transfers this absolute calibration over every observation of the survey.

In this section, we describe the method used to perform the relative calibration of the Pan-STARRS1 data. First, in §4.2.1, we describe the general problem of the

[1]The gain of the GPC1 camera is nearly 1 ADU/electron, and we include the quantum efficiency (electrons per photon) in the detector throughput, so we do not distinguish between ADUs and photons in this discussion

Figure 4.1 *(following page)* Map of the number of times the sky has been observed by Pan-STARRS1, overall (left panels) and in photometric weather (right panels) (see §4.2.3). The x-axes give right ascension and the y-axes give declination, both in degrees. White to black spans 0 to 16. The ten black circles are the locations of the 10 medium-deep fields, which are observed more frequently than the rest of the survey area. In the winter of 2010, the combination of bad weather and the malfunction of the Pan-STARRS1 shutter suspended operations, leading to an area of poor coverage in *gri* around right ascension 100°.

Figure 4.1 (continued)

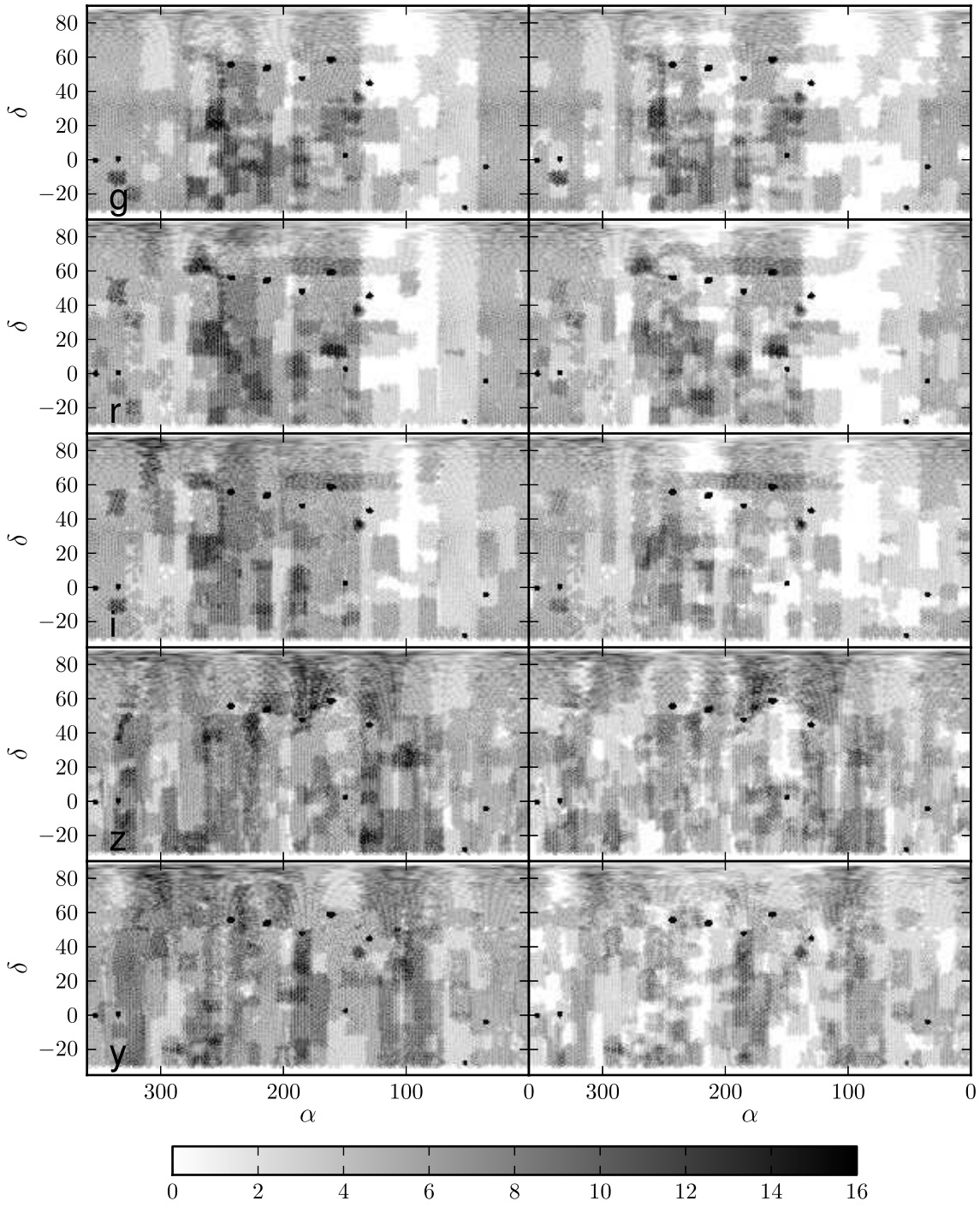

photometric calibration of optical data. In §4.2.2, we describe the algorithm used to perform the relative calibration of the survey, that of Padmanabhan et al. (2008). In §4.2.3, we then describe the details of the implementation of the algorithm for processing PS1 data.

4.2.1 The Goal of Photometric Calibration

The quantities of scientific interest in an imaging survey are usually the astrometry and photometry of objects as a function of time. The photometry of an object gives the flux from that object reaching the earth within a filter bandpass. For linear detectors like the PS1 CCDs, instead the number of photons per second N reaching the detectors is directly measured, which is simply related to the flux f by

$$N = Kf \tag{4.1}$$

if noise is ignored. The task of the photometric calibration is to solve for the throughput K.

Conventionally, the photometry of an object is given in magnitudes m, with $m = -2.5 \log f/f_0$, where f_0 gives the AB magnitude reference flux (Oke & Gunn, 1983). Then Equation 4.1 becomes $m_{\rm inst} + Z = m$, with the instrumental magnitude given by $m_{\rm inst} = -2.5 \log N$ and the zeropoint given by $Z = 2.5 \log Kf_0$. We work in these logarithmic variables for the rest of this work, and so seek to determine the zero points Z of each observation in the survey.

The zero points Z are determined by the light collecting efficiency of all of the components of the system. At a particular wavelength λ, Z can be decomposed into a

number of factors describing the system:

$$Z = 2.5 \log A T_a T_o T_f T_d f_0 \tag{4.2}$$

Here A gives the collecting area of the telescope, and T_a, T_o, T_f, and T_d the throughputs of the atmosphere, optics, filter, and detector, respectively. In principle, Z can be different for each star in each exposure, if, for instance, the filter throughput or detector efficiency varies over the focal plane.

The relative calibration of the survey is concerned only with how Z varies from object to object in the survey. We can then separate Z into two terms, $Z = Z_a + Z_r$, where Z_a is a constant giving the absolute zero point of the survey in a particular situation, and Z_r gives the relative change in zero point from Z_a. Unchanging components of Z, like the reference flux f_0 and mirror area A, affect only Z_a and are independent of Z_r. The model for Z_r must be simple enough to allow its components to be constrained, but flexible enough to capture the variation in Z_r.

For a system like PS1, where the optical system, filter, and detector are essentially unchanged over the course of the night, we can suppose that A, T_o, T_f, and T_d are constant over the course of the night. We can then encapsulate the effect of all these terms on the zero point as a single term, a, for that night, with $a = 2.5 \log A T_o T_f T_d$, and seek to measure how a varies over the course of the survey.

We must also account for T_a, the variation in the transparency of the atmosphere. We model the atmospheric transparency simply as

$$2.5 \log T_a = -kx \tag{4.3}$$

where k describes the effectiveness of the atmosphere at extinguishing light, and x is the airmass of the observation (Padmanabhan et al., 2008). The survey is executed so

that all observations have low airmass; the largest airmass included is 2.7 and the vast majority of images have airmass less than 1.6. Equation 4.3 strictly holds only for monochromatic light, or when the atmospheric extinction does not vary with wavelength. This assumption is violated in the $y_{\rm P1}$ band, where there are strong water absorption features in the atmospheric extinction (see §4.4 and Tonry et al. (in preparation)). Moreover, k will only be constant over a night if the atmosphere is isotropic and unchanging in time, an assumption clearly violated when clouds are present. Still, we find that for most of the nights of the survey, the simple model $2.5 \log T_a = -kx$ is largely satisfactory (but see §4.4.2 for more details).

We therefore present as a starting point for our photometric model the simple expression $Z = a - kx$, consistent with the above discussion. We ultimately adopt a more complicated variation of this function in §4.2.3. The problem of photometric calibration then becomes to determine the parameters a and k of such a model for each night of the survey. We perform this calibration following the algorithm of Padmanabhan et al. (2008), finding the parameters that minimize the variance of repeat observations of each star.

4.2.2 Algorithm

An optical survey provides instrumental magnitudes $m_{\rm inst}$ of objects in the sky. We may have several repeated observations of the same object, $m_{{\rm inst},o,i}$ with uncertainties $\sigma_{o,i}$, where o labels an object and i labels its observations. We are ultimately interested in the calibrated magnitude m of the object, with $m = m_{\rm inst} + Z_a + Z_r$, where Z_a and Z_r are defined in §4.2.1. We find Z_r by minimizing

$$\sum_o \sum_i (m_{o,i} - \overline{m_o})^2 / \sigma_{o,i}^2 \tag{4.4}$$

where $\overline{m}_o$ is the average of $m_{o,i}$ over all observations of object o. The absolute zero point Z_a cancels out of this expression.

Letting $\mathbf{m}$ be a vector with every observation of every object in the survey, and using a linear model for Z, then $\mathbf{m} = \mathbf{m}_{\rm inst} + \mathbf{A}\mathbf{p}$, where $\mathbf{A}$ is the design matrix for Z and $\mathbf{p}$ contains the parameters of the model for Z. For the simple model for Z described in §4.2.1, $\mathbf{p}$ is a vector containing a parameter a and k for each night of the survey. The vector $\mathbf{m}$ has length $n_{\rm obs}$, the total number of observations of all objects in the survey. The matrix A has dimensions $n_{\rm obs} \times n_{\rm par}$, where $n_{\rm par}$ is the number of parameters in the model. Furthermore, let $\mathbf{W}$ be the $n_{\rm obs} \times n_{\rm obs}$ matrix of weights, such that if $\mathbf{m}_j$ corresponds to an observation of object o, then

$$\sum_i W_{i,j} m_i = \overline{m}_o \tag{4.5}$$

We then want to solve

$$0 = \mathbf{m} - \mathbf{W}\mathbf{m} \tag{4.6}$$

in a least-squares sense. Expanding $\mathbf{m}$ in terms of $\mathbf{m}_{\rm inst}$, and rearranging, we obtain

$$(1 - \mathbf{W})\mathbf{A}\mathbf{p} = (\mathbf{W} - 1)\mathbf{m}_{\rm inst} \tag{4.7}$$

We solve this in a least-squares sense using a simple diagonal covariance matrix $\mathbf{C}$, with diagonal elements equal to the photometric variance in measurement i. We impose an error floor of 0.01 mags on the photometric variances, to prevent a few bright stars from dominating the fit. Letting $\mathbf{A}' = (1 - \mathbf{W})\mathbf{A}$ and $\mathbf{b} = (\mathbf{W} - 1)\mathbf{m}_{\rm inst}$, this is an ordinary linear least squares problem with solution

$$\mathbf{p} = (\mathbf{A}'^{\intercal}\mathbf{C}^{-1}\mathbf{A}')^{-1}\mathbf{A}'\mathbf{C}^{-1}\mathbf{b} \tag{4.8}$$

We solve this equation directly to find $\mathbf{p}$ and hence Z_r, the relative photometric calibration of the survey.

The structure of $\mathbf{A}'$ is illustrated in more detail in Padmanabhan et al. (2008). We mention one appealing feature of the structure of the problem, however: if $\mathbf{A}'$, $\mathbf{W}$, and $\mathbf{m}_{\rm inst}$ are written as sums of $\mathbf{A}'_i$, $\mathbf{W}_i$, and $\mathbf{m}_{{\rm inst},i}$, where the terms in these sums contain only rows corresponding to observations of object i and are otherwise 0, then likewise $\mathbf{A}'^{\intercal}\mathbf{C}^{-1}\mathbf{A}'$ and $\mathbf{A}'\mathbf{C}^{-1}\mathbf{b}$ split into sums of terms involving only observations of a single object each. This simplifies the computation of the matrices $\mathbf{A}'^{\intercal}\mathbf{C}^{-1}\mathbf{A}'$ and $\mathbf{A}'\mathbf{C}^{-1}\mathbf{b}$ and allows the terms contributing to them to be computed in parallel without ever requiring the matrix $\mathbf{A}'$ to be built. This is critically important because $\mathbf{A}'$ has size $n_{\rm obs} \times n_{\rm par}$, which for a survey of a billion observations and a model containing thousands of parameters contains trillions of elements. Because of the intrinsic parallelism of the problem, only $\mathbf{A}'^{\intercal}\mathbf{C}^{-1}\mathbf{A}'$ needs to be built, which is of manageable size. Likewise, the parallelism means that only the observations of a single object, and not the observations of the entire survey, need to be simultaneously read into memory.

The matrix $\mathbf{A}'^{\intercal}\mathbf{C}^{-1}\mathbf{A}'$, computed as described above, is necessarily singular. The singularity occurs because inevitably, for any solution Z_r, the solution $Z_r + c$ is equally good for any c. The constant c is degenerate with the absolute calibration of the survey. Depending on the model for Z_r, other singularities may exist. Accordingly, we perform a singular value decomposition of $\mathbf{A}'^{\intercal}\mathbf{C}^{-1}\mathbf{A}'$. Eigenvectors of $\mathbf{A}'^{\intercal}\mathbf{C}^{-1}\mathbf{A}'$ below a certain threshhold are fixed using priors, as described in Padmanabhan et al. (2008). The singularities affecting the PS1 calibration are described in §4.2.3.

This method correctly derives best-fit parameters $\mathbf{p}$ describing the relative photometric calibration. The above discussion has described the photometric

calibration algorithm in general terms. We now describe the details of the calibration as applied to the PS1 survey.

4.2.3 Details for Pan-STARRS1

The most important question to be answered in applying the photometric calibration algorithm to a particular survey is the choice of model for Z_r. The simplest reasonable model uses $-2.5 \log Z_r = a_n - k_n x$, where a_n describes the throughput of the optics, filters, and detector on a night n, and k_n describes the transparency of the atmosphere on that night, as described in §4.2.1. We need to refine this model slightly for PS1.

In wide-field surveys, frequently the system response depends on the position of the star in the focal plane, for example, because of the need for an illumination correction (Hogg et al., 2001). The raw Pan-STARRS1 images are already corrected for non-uniform detector throughput across the field of view according to a static flat field derived from the combination of dome flats and stellar photometry. We nevertheless solve for a new flat field using the wealth of data taken since the beginning of the survey. Comparison between SDSS and PS1 data indicated that the flat field changed abruptly three times during the survey (Finkbeiner et al., 2012). We accordingly fit for separate flat fields $f_{i,j}$ for the four different "seasons" to account for this behavior, so that $Z = a_n - k_n x + f_{i,j}$. Here i indexes over locations in the focal plane, which we take to be the four quadrants of each of the 60 CCDs in the PS1 focal plane, and j indexes over the four seasons (Table 4.1).

Analysis of Z derived for images taken as part of the medium-deep survey revealed that the amount of flux registered by the PS1 system systematically varied depending on the image quality of the individual images, in the sense that flux is lost for images with a very small or, especially, very large FWHM. To account for this variation, we

Table 4.1. Flat Field Seasons

Season	Begin Date	End Date
Season 1	—	10 April 2010
Season 2	10 April 2010	11 May 2010
Season 3	11 May 2010	11 April 2011
Season 4	11 April 2011	—

Note. — The dates marking the boundaries of the different time periods for which independent flat fields are used in the photometric model, from Finkbeiner et al. (2012). Season 1 includes all data taken before 10 April 2010, while season 4 includes all data taken after 10 April 2010.

include in our model for Z a quadratic w in FWHM, leaving us with the model

$$Z = a_n - k_n x + f_{i,j} + w(F) \tag{4.9}$$

where F is the FWHM of the image in which the observation was made. This model is summarized in Table 4.2, and is the final model we adopt to derive the Pan-STARRS1 zero points.

We have experimented with fitting only a single k term for the entire survey, rather than fitting one k term for each night. However, the best fit values of k can vary from night to night, by about 0.05 mags/airmass (§4.4.3). That said, the median standard deviation in airmass x for all observations on a given night is only about 0.1, leading to an induced uncertainty of about 5 mmag from ignoring the variation in k. Nevertheless, because the extreme edges in declination of the survey, the north celestial pole and declination $-30°$, must be observed at relatively high airmass, neglecting the variation in k leads to errors in the photometric calibration of the survey on large angular scales. For this reason, we fit a k term for each night of the

Table 4.2. Parameters of the Photometric Model

Parameter	Number	Note
a	~ 200	system (nightly)
k	~ 200	atmosphere (nightly)
f	$4 \times 60 \times 4$	illumination correction
w	2	FWHM correction (quadratic)

Note. — The parameters of the photometric model used in this work. The calibration is performed independently in each of the 5 Pan-STARRS1 filters. Observations have been performed on about 200 nights in each filter, though the exact number ranges from 293 in $z_{\rm P1}$ to 190 in $y_{\rm P1}$. The illumination correction has one parameter describing each of the four quadrants of the 60 PS1 CCDs, over four time periods. The constant term of the quadratic in w is not fit, because it is completely degenerate with a.

survey.

For the photometric calibration we use only observations taken at times when we believe the night to be photometric. We define "photometric" here to mean that the simple model for Z described above is satisfied on that night to within about 20 mmag. In cloudy weather the Z behave erratically; when we find evidence for clouds greater than 20 mmag in Z, we manually flag that portion of the night as non-photometric. We flag about 25% of the images taken as non-photometric. We are able to recognize exposures as taken in non-photometric conditions only when they are discrepant with other overlapping Pan-STARRS1 exposures, or when they overlap the SDSS. As the Pan-STARRS1 survey continues, our ability to flag non-photometric exposures will improve, though the analysis of §4.3 indicates that our performance is already good.

We wish to use only secure observations of typical stars in the calibration, to avoid any bias in the calibration from anomalous measurements. We therefore use only

objects for which at least one detection had estimated uncertainty less than 30 mmag. We also exclude any objects for which any measurement of that object had an instrumental magnitude less than -14.25, to avoid any detector saturation effects. We finally exclude any detections on images with FWHM greater than four arcseconds.

We use techniques for measuring $m_{\rm inst}$ that assume that the object being measured is a point source (i.e., PSF mags). Accordingly, we wish to include only point sources in the calibration. For this purpose, we exclude any object for which more than 25% of the detections of that object have PSF magnitude minus aperture magnitude greater than 0.1 mags. We also exclude any objects for which more than 10% of the detections of that object have $m > c$, with c equal to 19 mag in $g_{\rm P1}$ and $r_{\rm P1}$, 18.75 in $i_{\rm P1}$, and 18 in $z_{\rm P1}$ and $y_{\rm P1}$. These correspond approximately to the magnitudes at which the SDSS finds that the number density of galaxies exceeds the number density of stars, and so these cuts further reduce the galaxy contamination in our analysis.

We iterate the photometric calibration several times and clip discrepant observations and images on each iteration, reducing the clipping threshhold by a factor of two on each iteration until reaching 3σ, as described below. This reduces the sensitivity of the algorithm to outliers. In clipping detections, we compute $\Delta = m - \overline{m}$ for each detection. For each image i, we find the mean μ_Δ and standard deviation σ_Δ of Δ on that image. An image is clipped if μ_Δ or σ_Δ is inconsistent with their respective distributions for all images at the clipping threshhold. About 3% of images are clipped in this process; most periods of non-photometric conditions have already been flagged by hand. A detection on an image is clipped if $|\Delta/\sigma|$ is greater than the clipping threshhold for that detection, where σ is the sum in quadrature of the photometric uncertainty for that detection and σ_Δ for that image. About 4% of detections are clipped. These include detections with problematic photometry and variable stars.

We modified the algorithm of Padmanabhan et al. (2008) slightly to incorporate including an external source of photometry in the calibration. When enabled, if external photometry for an object is available, we set $\overline{m}$ for that object to be that given by the external photometry, so that for these objects the best fit solution simply minimizes the difference between the external and internal photometry. We can then add, for instance, all of the photometry from the SDSS matching PS1 objects into the photometric calibration. We have experimented with both including and excluding the SDSS photometry. In the final photometric calibration we currently use for PS1, we include the SDSS photometry, in order to improve our ability to detect non-photometric conditions. The derived zero points vary only slightly depending on whether or not the SDSS is included as an external reference in the calibration, by about 5 mmag rms §4.3.2.

We impose Gaussian priors on the parameters of the photometric model when the photometry poorly constrains them, as described in Table 4.3. We take the set of poorly constrained eigenvectors of the solution and find the best fit parameters for those eigenvectors such that the priors are satisfied, as described in Padmanabhan et al. (2008). The priors serve three primary functions. The first is to set the absolute calibration of the survey; the second is to resolve the degeneracy between the a and f terms; and the third is to resolve the degeneracy between the a and k terms on nights when the range of airmasses probed is small.

We impose a prior for the absolute calibration of the survey based on the work of Tonry et al. (in preparation), which uses photometry from standard stars and the Hubble Space Telescope to determine the absolute calibration of Pan-STARRS1. We choose a prior for the a terms to agree with the results of that work. When using the SDSS as a reference, we impose this prior by using the color transformations of Tonry et al. (in preparation) to transform the SDSS magnitudes into the

Table 4.3. Priors

Parameter	Prior	σ	Parameter	Prior	σ
a_g	24.408	1	k_g	0.147	0.05
a_r	24.679	1	k_r	0.085	0.03
a_i	24.556	1	k_i	0.044	0.02
a_z	24.218	1	k_z	0.033	0.02
a_y	23.237	1	k_y	0.073	0.03
f	0	0.02	w	0	0.1

Note. — The Gaussian priors for the parameters in the photometric model. The priors on w are irrelevant as w is always well constrained by the data. The priors on f serve only to break the degeneracy between a and f. The priors on a set the absolute calibration of the survey, and are tuned to match the SDSS with the color transformations of Tonry et al. (in preparation). The priors on k constrain k on nights when the range of airmasses probed by the survey is small, causing k and a to be degenerate.

Pan-STARRS1 bandpasses, and then the absolute calibration is fixed directly by the photometric solution by reference to the color-corrected SDSS.

The a and f terms in the photometric model have an exact degeneracy, in that Z is unchanged if all of the a are increased and f is decreased. This degeneracy is removed by enforcing a prior on all of the f to be zero, with an uncertainty of 20 mmag.

The a and k terms are degenerate if the range of airmass probed on a night is small. This degeneracy is obviously exact on a night consisting of a single image. Then kx is just a constant for the night, and so any change in a can be canceled with a change in k. These degeneracies are removed by setting a prior on k to be equal to the value of k on a typical night.

After we obtain an iterated photometric solution, we perform a final adjustment to the derived Z for each image. We can robustly compute $\mu_{\Delta,i}$ for each image i in the survey. Ordinarily we use $\mu_{\Delta,i}$ to clip images that are discrepant from the rest of the

photometric solution. Having obtained a photometric solution, however, we use the $\mu_{\Delta,i}$ to improve the calibration of the survey by adjusting the photometric solution Z_i for image i by $\mu_{\Delta,i}$. This induces no changes in the photometric calibration on large spatial scales, but does clean up the light curves of bright objects slightly. The standard deviation of $\mu_{\Delta,i}$ is about 5 mmag (§4.3).

4.3 Results

We compute the PS1 photometric calibration using about one billion observations in each filter, solving for about a thousand parameters for each filter. These parameters describe the system zeropoint a, atmospheric transparency k, and flat field, as well as an image quality correction as described by Equation 4.9. We perform the computation in parallel over the available cores in our system, using the inherent parallelization described in §4.2.2. The computation time is dominated by reading data from disk for processing, and takes about two days. The parallelization of the computation and the database operations more generally were greatly simplified by the Large Survey Database software (Jurić, in preparation).

We find that the results of the photometric calibration account for variations in the mean zero point per exposure of the Pan-STARRS1 system to better than 10 mmag rms, albeit with some areas of worse calibration. We demonstrate this accuracy, checking the internal consistency of the solution (§4.3.1), the consistency with the SDSS (§4.3.2), and the consistency of the colors of stars in different parts of the sky (§4.3.3).

4.3.1 Internal Consistency

We first test the internal consistency of the photometric calibration in three ways: by using simulated data, by examining the residuals from our photometric model over the sky, and by comparing with an alternative method for calibrating the MD fields.

Tests with simulated data indicate that errors due to the statistical uncertainty of the observations are negligible. In these simulations, which do not include clouds, we take the actual set of observations of all of the stars used in this analysis. For each star, we then declare its true magnitude for the purposes of the simulation to be equal to the mean of all measurements of that star. We then convert these true magnitudes to instrumental magnitudes, using our adopted model for the zero points, with parameters drawn at random from the distributions given in Table 4.3. Noise is then added to these simulated measurements consistent with estimates from the actual Pan-STARRS1 data, to produce a set of simulated Pan-STARRS1 observations.

These simulated observations are then photometrically calibrated, and the recovered zero points for each observation are compared with the true zero points. The standard deviation in the difference between the recovered magnitudes and true magnitudes is less than 0.2 mmag when using a simulated external reference catalog designed to match the SDSS. If this simulated external reference catalog is not used, the standard deviation remains less than 0.2 mmag, though a small number of observations have zero points off by as much as 6 mmag in the $y_{\rm P1}$ band.

These simulations do not include systematic errors caused by deviations in the system throughput from our model (for instance, clouds). However, they verify that the data have the signal-to-noise necessary to constrain the model, and that the algorithm accurately recovers the photometric model parameters when given good data.

We perform an internal test of the size of the deviations from our photometric model using $\Delta = m - \overline{m}$. For each exposure, we compute μ_Δ and σ_Δ, the mean and standard deviation of Δ for all observations on a single exposure. When an individual exposure has a zero point inconsistent with our photometric model, μ_Δ will depart from zero. Exposures with highly variable point spread functions or other problems with the photometry will have large σ_Δ. The typical size of σ_Δ will depend on the brightness of the stars used in the calibration; here we are interested only in verifying that the σ_Δ are homogeneous over the survey. Figure 4.2 shows a map of $|\mu_\Delta|$ and σ_Δ in each of the PS1 bands, using a PS1 calibration that does not include the SDSS as an external reference. The maps of $|\mu_\Delta|$ are fairly uniform over the sky; a few isolated areas are slightly problematic, but no large scale trends are obvious and the Galactic plane makes no appearance. The maps of σ_Δ are somewhat patchier and the Galactic center appears as an area of only slightly increased σ_Δ, a testament to the performance of the IPP in crowded fields. The σ_Δ have the tendency to be larger in areas with more observations, despite correction of σ_Δ by $\sqrt{N/(N-1)}$, where N is the number of observations of the sky. This is likely because exposures taken as part of TTI pairs are especially photometrically consistent; the two exposures are taken only fifteen minutes apart with a common position angle, and so each detection lands on nearly the same pixels in the focal plane, and the point spread function has had little time to change.

Figure 4.3 shows the same information as in Figure 4.2 as a histogram, giving the distribution of μ_Δ and σ_Δ. Unsurprisingly, $\overline{\mu_\Delta}$ is near zero. The scatter in μ_Δ is only about 3 mmag. This is a lower bound on the actual uncertainty in our photometric calibration. The σ_Δ are about 12 mmag, except in $y_{\rm P1}$, where the photometric scatter is about 17 mmag.

The scatter in μ_Δ will be lower than the true uncertainty in the calibration because

Figure 4.2 *(following page)* Maps of $|\mu_\Delta|$ (left panels) and σ_Δ (right panels) in $grizy_{\rm P1}$. The x-axes give right ascension and the y-axes give declination, both in degrees. These give the consistency of the zero points and the scatter in the photometry over the sky. White to black is 0–10 mmag for the left panels and 5–25 mmag for the right panels. The Galactic center is barely visible as a region of increased σ_Δ near $(266^\circ, -29^\circ)$. The σ_Δ are substantially larger in the $y_{\rm P1}$ band than in the other bands.

Figure 4.2 (continued)

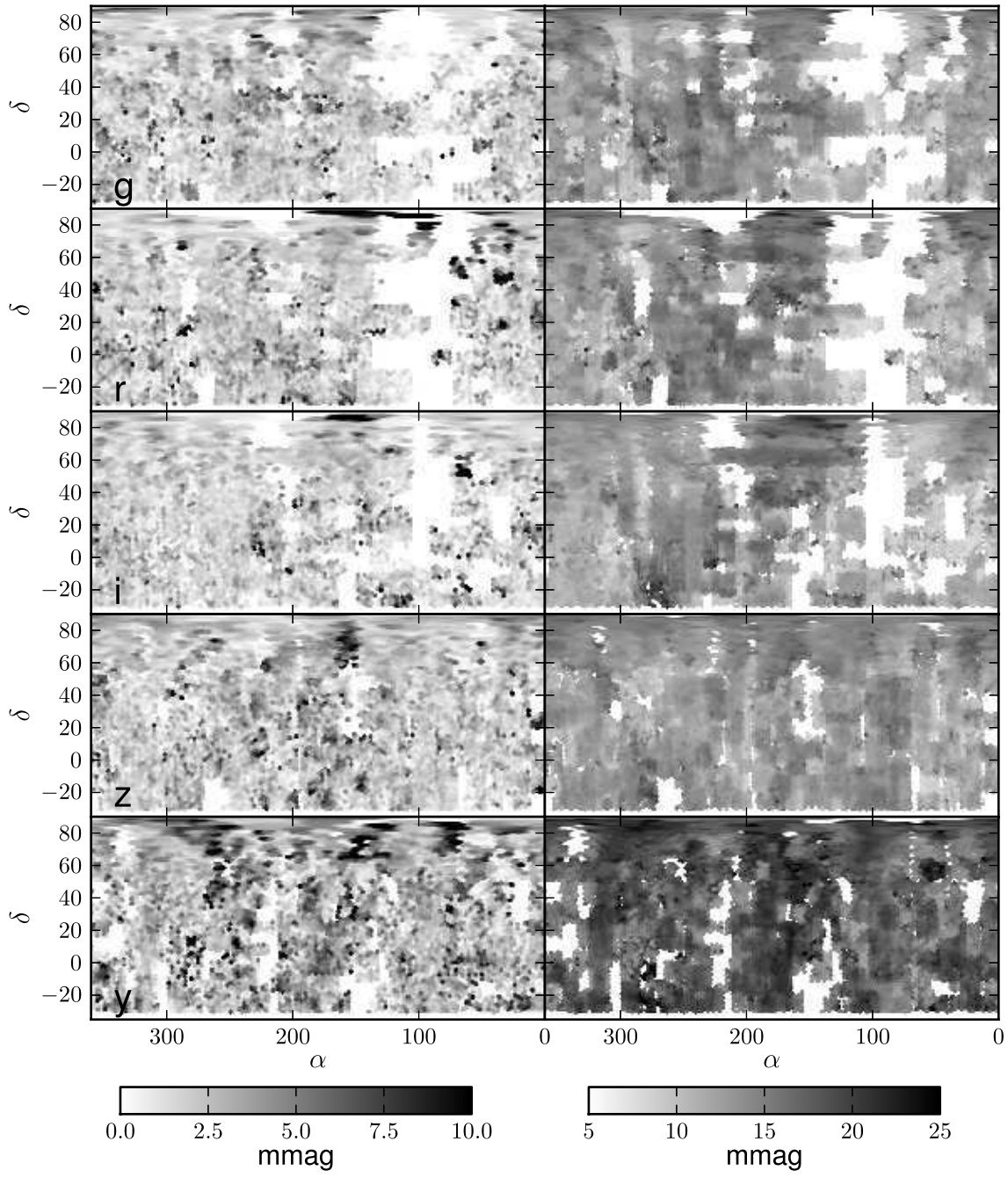

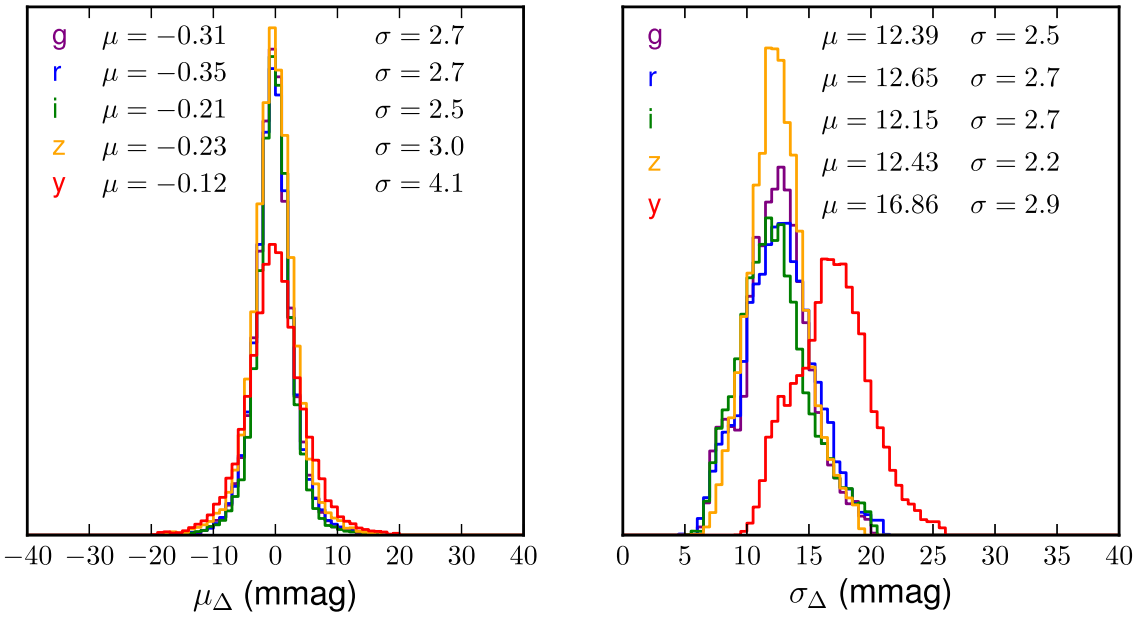

Figure 4.3 Histograms of μ_Δ (left) and σ_Δ (right) in $grizy_{\rm P1}$. The mean μ and standard deviation σ of μ_Δ and σ_Δ are labeled for each filter. The scatter in μ_Δ represents a lower bound on the uncertainty in our photometric calibration (§4.3.1). The σ_Δ are quite similar among the various bands, except in $y_{\rm P1}$, which has 50% more scatter than the other bands.

many stars have only been observed a few times, and often as part of correlated TTI pairs. We can eliminate this problem by limiting the exposures used to compute μ_Δ to exposures on MD fields. In this case, the scatter in μ_Δ goes up to 5 mmag, while σ_Δ remains about the same. This scatter in μ_Δ is more realistic, and represents the accuracy of the photometric calibration that we could expect after covering the sky many times. However, sparsely covered portions of the sky may have photometric calibration errors much larger than found in these well-covered MD fields.

As a final internal consistency check, we compare the zero points generated by the photometric calibration algorithm with the zero points for the MD fields of Finkbeiner et al. (2012). In that work, a very loose photometric model is adopted, which allows completely independent zero points for each exposure and a separate flat field for each night. We find that the zero points of this work agree with those of Finkbeiner et al. (2012) to about 5 mmag, consistent with our expectations from our internal tests of the model residuals on the MD fields.

4.3.2 Consistency with the SDSS

We can also verify the results of the photometric calibration by comparing our zero points with those we would derive by forcing the photometry to match an external reference as closely as possible. The SDSS has observed about one third of the sky, about half of the area that Pan-STARRS1 has observed. We find zero points $Z_{\rm SDSS}$ for individual PS1 exposures that overlap the SDSS. We compare these zero points with the zero points obtained from the photometric calibration algorithm, performed without using the SDSS as a reference.

We compute $Z_{\rm SDSS}$ by transforming the SDSS magnitudes of stars onto the Pan-STARRS1 system using the color transformations of Tonry et al. (in preparation). For each PS1 exposure, $Z_{\rm SDSS} = \langle m_{\rm SDSS} - m_{\rm inst} \rangle$. We use only SDSS

stars with $m_{\rm SDSS} < 18$ in the computation of $Z_{\rm SDSS}$.

The results of the comparison are shown in Figure 4.4. The internal Pan-STARRS1 zero points agree with the SDSS-based zero points to about 10 mmag in all bands, ranging from 7 mmag in $r_{\rm P1}$ to 13 mmag in $y_{\rm P1}$. There are slight offsets in the mean zero point between the internal and SDSS zero points. These means are determined by the absolute calibration of the survey, and are fixed by a prior; they provide no information about the relative calibration that is the focus of this work. A small number of large photometric outliers do exist, and may be removed as the number of overlapping observations in the survey increases.

The spatial structure of the differences between the internal and SDSS-based zero points is of particular interest. Figure 4.5 shows maps of the mean difference between the calibrated PS1 magnitudes of objects used in the photometric calibration and their color-transformed SDSS magnitudes, in pixels 0.2° on a side. The maps clearly show signs of errors in both the PS1 and SDSS photometric calibration, suggesting that a simultaneous PS1-SDSS calibration would be valuable. The SDSS scan pattern is visible as narrow 3° stripes, approximately in right ascension, while the PS scan pattern is seen as rectangles in right ascension and declination. The largest problems with the SDSS involve runs poorly connected to the main body of the SDSS; runs around $\alpha = 300°$ differ between PS1 and the SDSS by about 40 mmag. The internal PS1 calibration shows clear ~ 25 mmag problems in $g_{\rm P1}$ at (170°, 5°) and in $z_{\rm P1}$ at (25°, 10°), to name a few, probably due to unrecognized cloudy weather. Moreover, in $z_{\rm P1}$ and $y_{\rm P1}$ especially, parts of the maps are mottled at the 3° scale of the PS1 focal plane, indicating a problem with the PS1 photometry. Despite these problems, the overall agreement between the two sets of measurements is remarkable; the rms of these maps is about 11, 10, 11, 12, and 16 mmag in $grizy_{\rm P1}$. The results presented in Figure 4.4 are slightly better than these, because for that figure zero points were

Figure 4.4 *(following page)* Comparisons between the zero points of this work and zero points derived relative to the SDSS, for the filters $grizy_{\mathrm{P1}}$ (rows). The left column gives the zero points of this work relative to the zero points derived from the SDSS, both in magnitudes. It also gives the number N of images used in the comparison. The middle column gives the difference in mmag between the two zero points with the SDSS zero points, in magnitudes. The third column gives a histogram of the differences in mmag, along with their mean μ and standard deviation σ. Unrecognized non-photometric conditions lead to points with low SDSS-derived zero points and large positive differences between SDSS- and PS-derived zero points.

Figure 4.4 (continued)

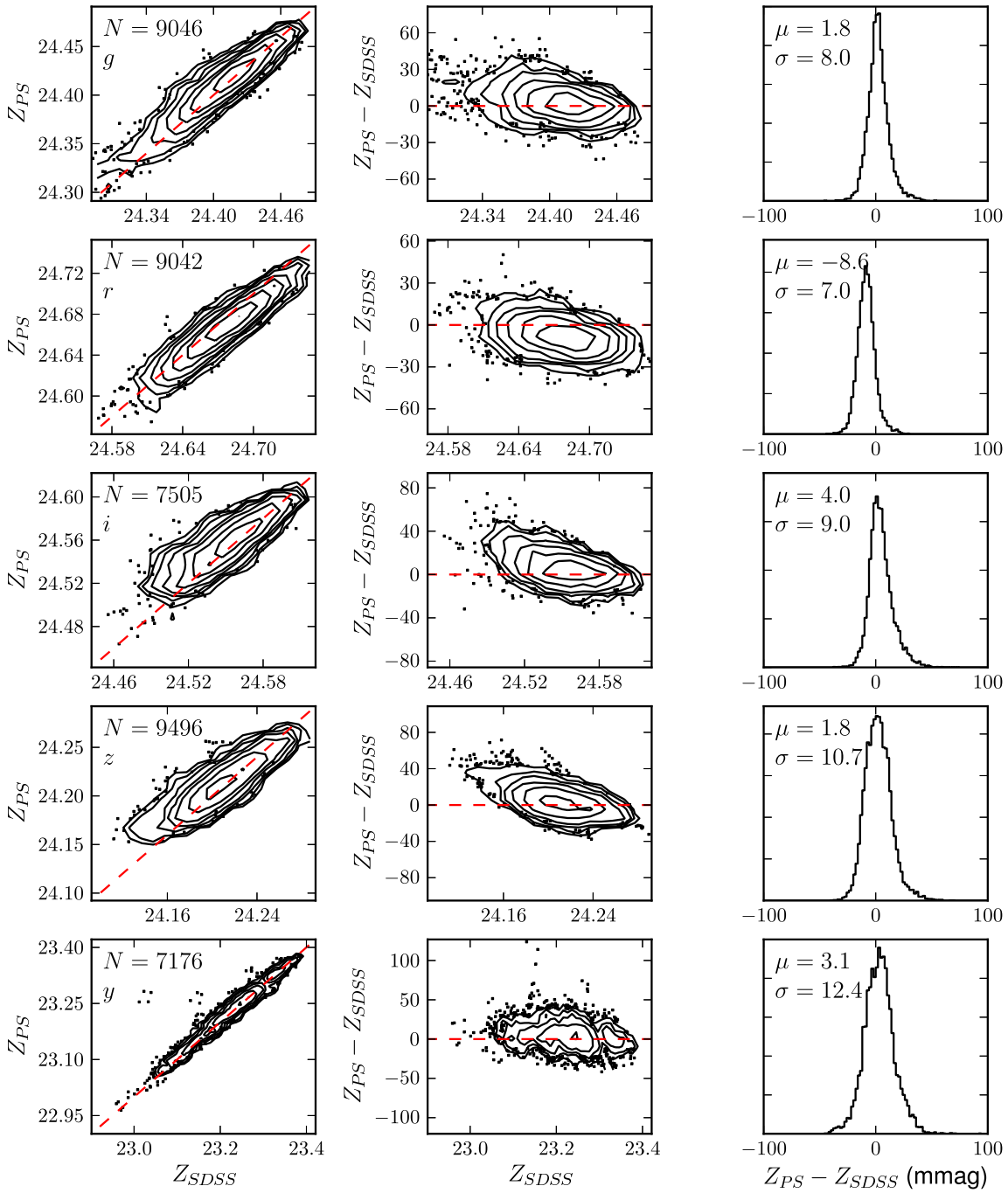

calculated for individual PS1 images, averaging over multiple SDSS runs and over the PS1 photometric nonuniformity in the focal plane.

4.3.3 Consistency of Stellar Colors

We can additionally check the accuracy of the photometric calibration by testing the consistency of the stellar locus over the sky. This technique has the advantage over comparison with the SDSS that it can be applied over the entire sky. However, the presence of dust and intrinsic variations in stellar populations can cause the colors of the stellar locus to vary, limiting the effectiveness of this technique.

We measure the color of main-sequence turn-off stars over the sky to test the consistency of the stellar locus, following the technique of Schlafly et al. (2010). This is one of a number of related techniques; we could alternatively have used the principal color analysis of Ivezić et al. (2004) or the stellar locus regression of High et al. (2009). Figure 4.6 shows maps of the color of the blue tip of the stellar locus in the PS1 bands $grizy_{\rm P1}$.

The dominant signal in Figure 4.6 is clearly from the interstellar dust. After removing the dust according to Schlegel et al. (1998) and Schlafly & Finkbeiner (2011), at high Galactic latitudes most of the signal comes from problems with the photometric calibration. The most egregious example is in the $y_{\rm P1}$ band at (25°, -25°), of 40 mmag. Over most of the sky, calibration errors are consistent with expectations from the comparison with the SDSS, ~ 15 mmag.

4.4 Discussion

We interpret these results in the context of the stability of the Pan-STARRS1 system. The system stability divides naturally into four different components: the

Figure 4.5 *(following page)* Maps of the difference between the color-corrected SDSS magnitudes of stars and the internally-calibrated Pan-STARRS1 magnitudes of the same stars in the filters $grizy_{\rm P1}$ (rows). The x-axes give right ascension and the y-axes give declination. The rms of the maps is about 10 mmag. Narrow stripes in right ascension are symptomatic of problems with the SDSS photometric calibration, while rectangles in right ascension and declination indicate problems with the PS1 calibration. The filter used for each map is indicated in the lower left, while the rms of the map is indicated in the lower right.

Figure 4.5 (continued)

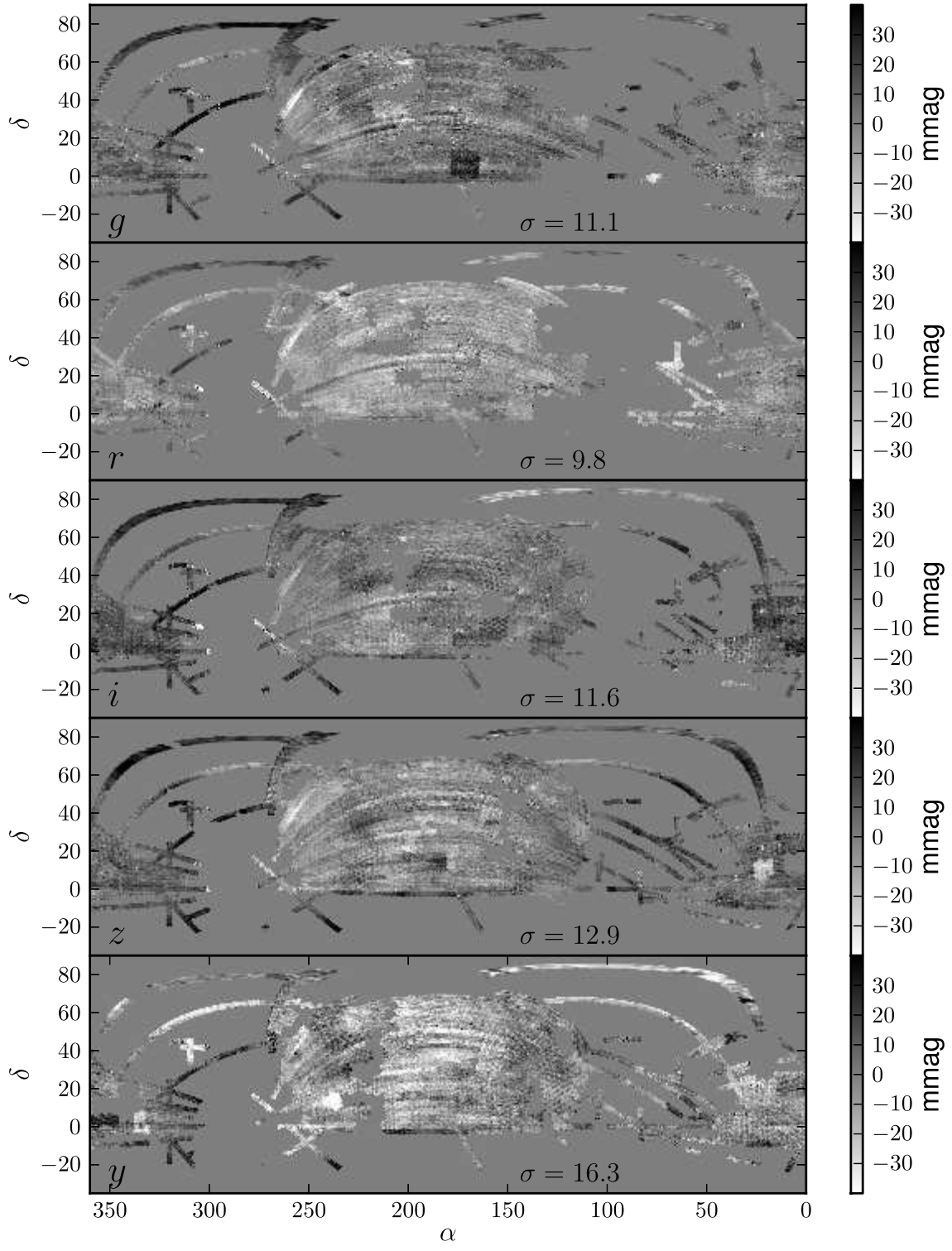

Figure 4.6 *(following page)* Maps of the color of the main-sequence turn-off (MSTO) stars observed by Pan-STARRS1. The four rows give the colors $g-r$, $r-i$, $i-z$, and $z-y$. The left column gives the observed MSTO color, while the right column gives the color corrected for dust according to Schlegel et al. (1998) and Schlafly & Finkbeiner (2011). Clearly the dust accounts for most of the signal in these maps, but problems with the photometric calibration are also evident, for example, in $y_{\rm P1}$ at (25°, −25°). Blank areas have no Pan-STARRS1 observations in photometric weather in one of the two bands making up the relevant color. Black and white are ±0.1 mag of the median color of each map.

Figure 4.6 (continued)

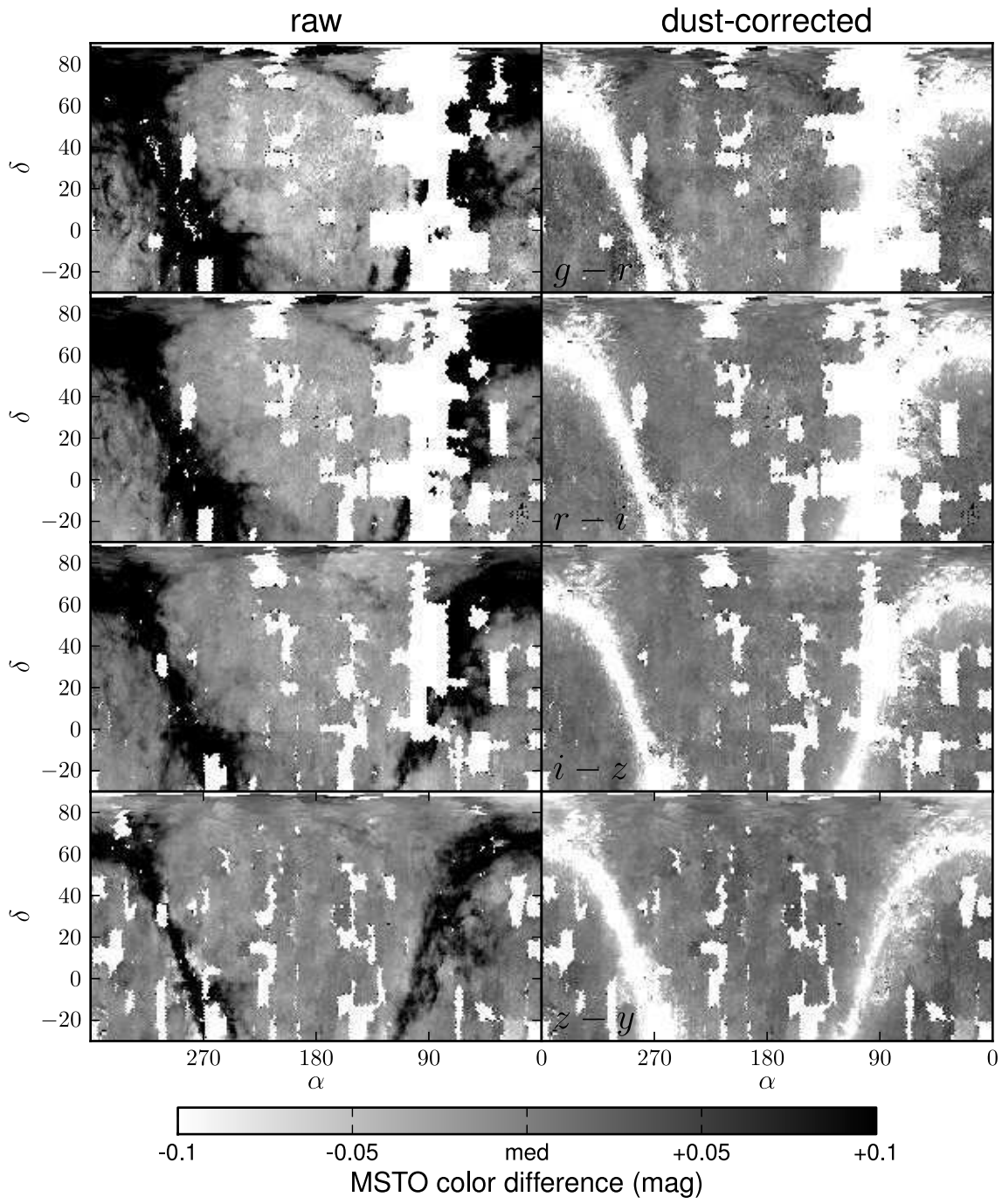

photometric stability over a single night (§4.4.1), the stability of the detector and optics over the course of the survey (§4.4.2), the stability of the atmosphere over the course of the survey (§4.4.3), and the stability of the flat field over the survey (§4.4.4).

4.4.1 Nightly Photometric Stability of PS1

The photometric model we have adopted to calibrate the survey assumes that the throughput of the system and atmosphere do not vary substantially over the course of a night. This assumption is occasionally violated, leading us to remove about 25% of the nights on which survey data are taken. The stability of the system on the remaining nights is excellent. Figure 4.3 showed that the typical model residuals are less than 5 mmag. However, the nightly stability can be shown more explicity in a plot of model residual as a function of time of night. Figure 4.7 shows a variety of plots of data taken on February 13, 2010, during the first month of full science operation of the survey. The first panel shows a density plot giving the distribution of Δ in mmag for each star in each image as a function of the hour in the night, with contours marking the mean and $\pm 1\sigma$ of Δ for each image. Dashed blue lines mark ± 20 mmag. The crosses indicate the fraction of the detections clipped from each image in the photometric calibration, and their color indicates the band that each image was taken in, using the same colors as in Figure 4.8. The photometric stability on this night is very good; the majority of images have $|\mu_\Delta| < 5$ mmag. The $g_{\rm P1}$ images taken around 14 hours, however, are discrepant at the 20 mmag level; this is the source of the clear Pan-STARRS1 calibration error evident at (170°, 10°) in the g band in Figure 4.5, and seems to be one of the largest calibration errors remaining in the data.

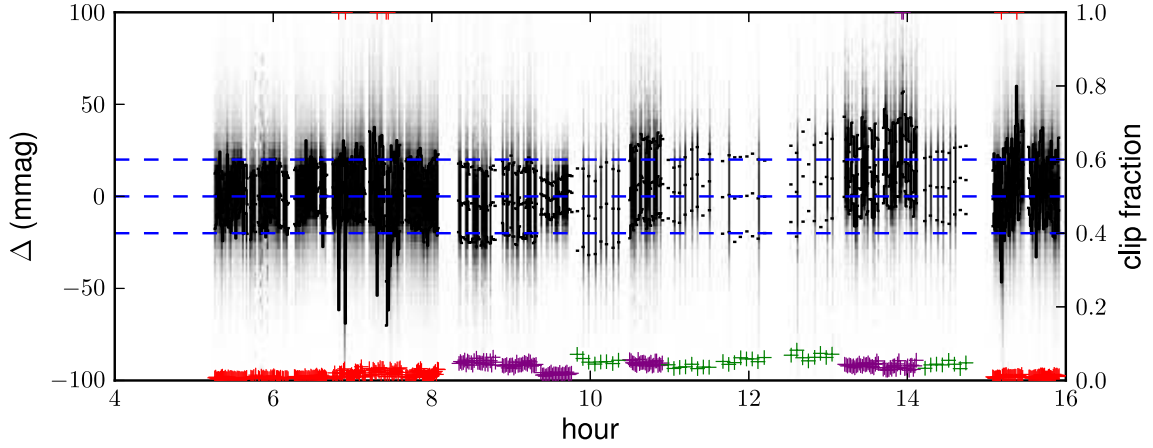

Figure 4.7 The performance of the Pan-STARRS1 photometry on 13 February 2010. The figure gives the distribution of residuals Δ, in mmag, of magnitudes of stars as observed on this night from the mean magnitudes of these stars, as a function of hour during the night. Each column in the figure corresponds to an image. The contours give the mean and $\pm 1\sigma$ of Δ for each image. Crosses give the fraction of observations in each image clipped from the calibration, with 0% corresponding to the bottom of the plot and 100% the top of the plot. The colors of the crosses give the band the image was taken in; the colors are the same as in Figure 4.8. The mean of Δ for each image is small throughout the night, except for a 20 mmag deviation around hour 14. This is one of the largest remaining photometric calibration errors in the survey. See §4.4.1 for details.

4.4.2 System Stability

The scatter in the zero-point residuals from the simple nightly photometric model we adopt is about 5 mmag, showing that the system is stable over the course of a night. However, this stability is not simply a nightly phenomenon; the system has been very stable over the whole course of the survey.

Ideally, we would measure the stability of the system as the scatter in the a-terms derived by the photometric calibration. This procedure can overestimate the true scatter in the system throughput, however, because of the degeneracy between the a- and k-terms on nights when the range of airmass probed by the survey is small. The median standard deviation of airmass in images taken in a single filter on a single

night is only 0.1, rendering a and k substantially degenerate on most nights. Accordingly, we instead test the stability of the system by looking at the scatter in the zero points Z at 1.2 airmasses, which is close to the average airmass of the survey. We ignore the dependence of Z on w and f; the former could contribute slightly to the scatter in Z, but should play only a minor role, while the latter is required to have mean zero. This combination of a and k is well-constrained, but includes variation both from a and from kx. The scatter from kx at 1.2 airmasses is $1.2\sigma_k$. We find in §4.4.3 that σ_k is less than about 0.05, so the atmosphere should contribute less than 60 mmag scatter to the zero points.

Figure 4.8 shows the zero points $a - kx$ at airmass 1.2 for each photometric night of the survey in the 5 Pan-STARRS1 bands. The $y_{\rm P1}$ bands have been offset by 0.7 mags for clarity. The zero points are extraordinarily stable, except in $y_{\rm P1}$. In the other bands, the intrinsic throughput of the Pan-STARRS1 system has varied by less the 20 mmag rms. A change in the system throughput near Modified Julian Day 55524 of 20 mmag is obvious in $griz$. This stability is surprising given that we expect as much as 60 mmag scatter in zero point from the airmass term alone, and requires that the scatter in k is actually less than 0.02 in $griz_{\rm P1}$.

The $y_{\rm P1}$ band has by far greater scatter in its nightly zero points than the other bands. This is presumably the result of two factors, both owing to the presence of strong water vapor absorption bands that overlap $y_{\rm P1}$ (Tonry et al., in preparation). First, because the atmospheric absorption is not approximately constant over $y_{\rm P1}$, modeling the $y_{\rm P1}$ zero point simply as linear in airmass is not appropriate. Second, the depth of the absorption bands varies with the amount of precipitable water vapor in the air, leading to varying zero points. An improved photometric calibration would then include more freedom in the $y_{\rm P1}$ zero points, potentially incorporating additional information about water vapor in the air, as has been proposed in a number of works

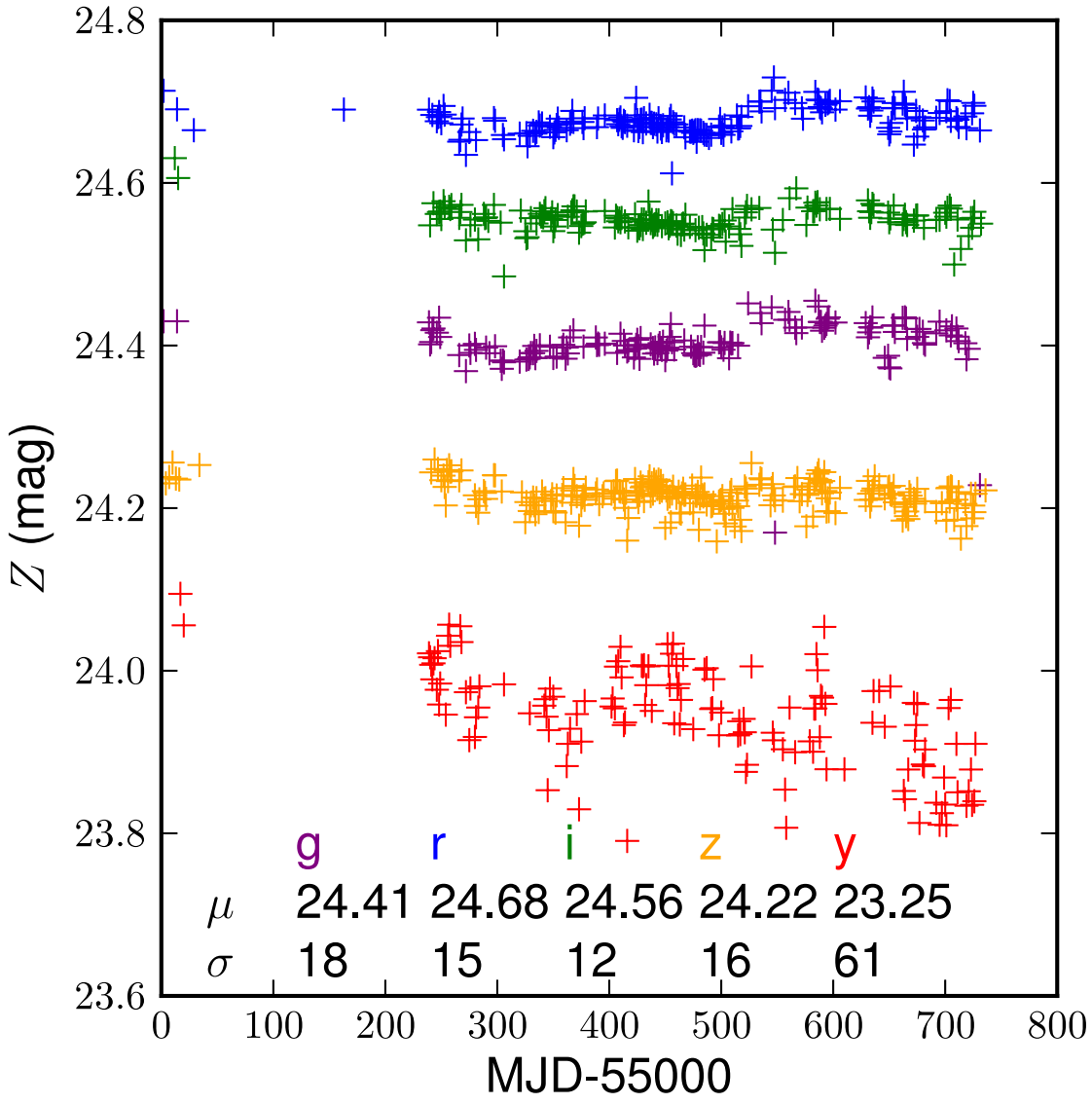

Figure 4.8 The system zero point $a - kx$ at airmass 1.2 derived by the photometric calibration for each night of the Pan-STARRS1 survey. The mean μ (in mag) and standard deviation σ (in mmag) of the zero points is given for each band. The $y_{\rm P1}$zero points have been offset by 0.7 mags for legibility. The intrinsic system stability is better than 20 mmag in *griz*. The $y_{\rm P1}$ band is by far less stable than the other bands, with 61 mmag of scatter in zero point, presumably owing to the sensitivity of $y_{\rm P1}$ to water in the atmosphere (see §4.4.2).

(Stubbs et al., 2007; Burke et al., 2010; Blake & Shaw, 2011), and adding color-airmass and color-water vapor terms to the photometric model.

The work of Tonry et al. (in preparation) considers the dependence of zero point on airmass in more detail. In particular, that work finds that adopting

$$2.5 \log T_a = -kx^{0.68} \tag{4.10}$$

more accurately describes the relation between zero point and airmass in the $y_{\rm P1}$ band. However, we find that owing to the small range of airmass probed on a single night, adopting this relation alters the zero points derived in this work only negligibly (~ 1 mmag). Even so, we note that extrapolating the PS1 magnitudes of stars to the magnitudes that would be observed above the atmosphere requires taking the nonlinearity into account. That problem is one of absolute calibration; in this work we consider only the relative calibration of the survey.

4.4.3 Atmospheric Stability

The stability of the atmosphere over Haleakala places a fundamental limit on the stability of the Pan-STARRS1 system. The atmospheric transparency, however, can only be separated reliably from the system throughput when a wide range of airmass is probed over the course of a night. On the typical night, however, the standard deviation in airmass of all observations in a single filter is less than 0.1. In the $i_{\rm P1}$ and $z_{\rm P1}$ bands, this corresponds to less than 5 mmag of atmospheric extinction, comparable in size to the typical model residuals, making it impossible to reliably measure the airmass term k in the photometric model for that night.

The problem is further complicated by the fact that the photometric calibration has access only to the differences in magnitudes of observations of the same stars.

Even when a night covers a wide range of airmass, if on another night the same stars were observed at the same airmasses, the calibration could reliably determine that those nights had the same k-term but not what that k-term was.

We use two techniques to test the variation in k from night to night. We limit ourselves to nights where σ_x, the standard deviation in airmass examined on that night, is greater than 0.1, and then look at the standard deviation in k for those nights. We determine k from our photometric model, as well as using only zero points derived from the SDSS (§4.3.2).

Measurements of k-terms derived from PS1-SDSS comparisons on nights with $\sigma_x > 0.1$ indicate that σ_k is 0.03, 0.04, 0.03, 0.07, and 0.07 in $grizy_{\rm P1}$. These results are sensitive to the limit on σ_x; taking $\sigma_x > 0.2$ results in σ_k equal to 0.03, 0.03, 0.03, 0.04, 0.09, though only about ten nights of the survey have σ_x that large. Reducing σ_x increases σ_k in all bands, presumably because σ_k becomes dominated by slight deviations from the photometric model. These estimates of σ_k all exceed our estimates for σ_k based on the stability of the total throughput at 1.2 airmass (§4.4.2), suggesting that the 20 mmag of scatter in zero points is dominated by atmospheric variations rather than variations in the PS1 system, and that the SDSS-based σ_k are overestimates.

We can repeat this analysis using k-terms derived directly from the photometric calibration. Because the PS1 survey region covers a larger range of declination than the SDSS covers, this allows more high-airmass observations to be included. Using nights with $\sigma_x > 0.1$ indicates that σ_k is 0.02, 0.02, 0.02, 0.04, and 0.05 in $grizy_{\rm P1}$. Using only nights with $\sigma_x > 0.2$ gives σ_k equal to 0.02, 0.02, 0.02, 0.02, and 0.04, which is consistent with our constraint from §4.4.2. If σ_k in $y_{\rm P1}$ is in fact about 0.04, then both the Pan-STARRS1 system and atmosphere are less stable in $y_{\rm P1}$ than in $griz_{\rm P1}$.

4.4.4 Detector Stability

The stability of the Pan-STARRS1 detector can be tested independently from the atmosphere. The raw PS1 images are flat-fielded with a single, static flat field derived from dome flats and stellar photometry taken early in the survey. The photometric calibration derives four independent flat fields for different time periods in the survey (Table 4.1). The time variation in these flat fields tests the stability of the detector.

Figure 4.9 shows the mean flat field and the difference from the mean flat field for the four flat field seasons in $grizy_{\rm P1}$. Each image consists of 16×16 pixels, describing the four quadrants of each of the 60 OTA CCDs composing the PS1 focal plane. The mean absolute difference of the flat for each season from the mean flat field is less than 5 mmag in all of the filters. Likewise, the standard deviation of the differences of the flat fields from the mean is less than 6 mmag in all of the filters. The bright ring present in the flat fields from the first season indicates that the edge of the focal plane in the first season was too faint and required correction. This may be due to problems with the photometry in images with poor image quality, which was especially problematic early in the survey and around the edge of the focal plane.

The mean flat has a scatter of about 10 mmag in all of the filters. Some striping in the mean flat suggests that one side of the PS1 OTA CCDs has a ~ 10 mmag different throughput from the other side. These variations should have been removed by the static PS1 flat field, yet are nevertheless robustly present in the photometric calibration and in comparison with the SDSS. This may point to an anomaly occuring during the observations of the stars used to construct the static PS1 flat field.

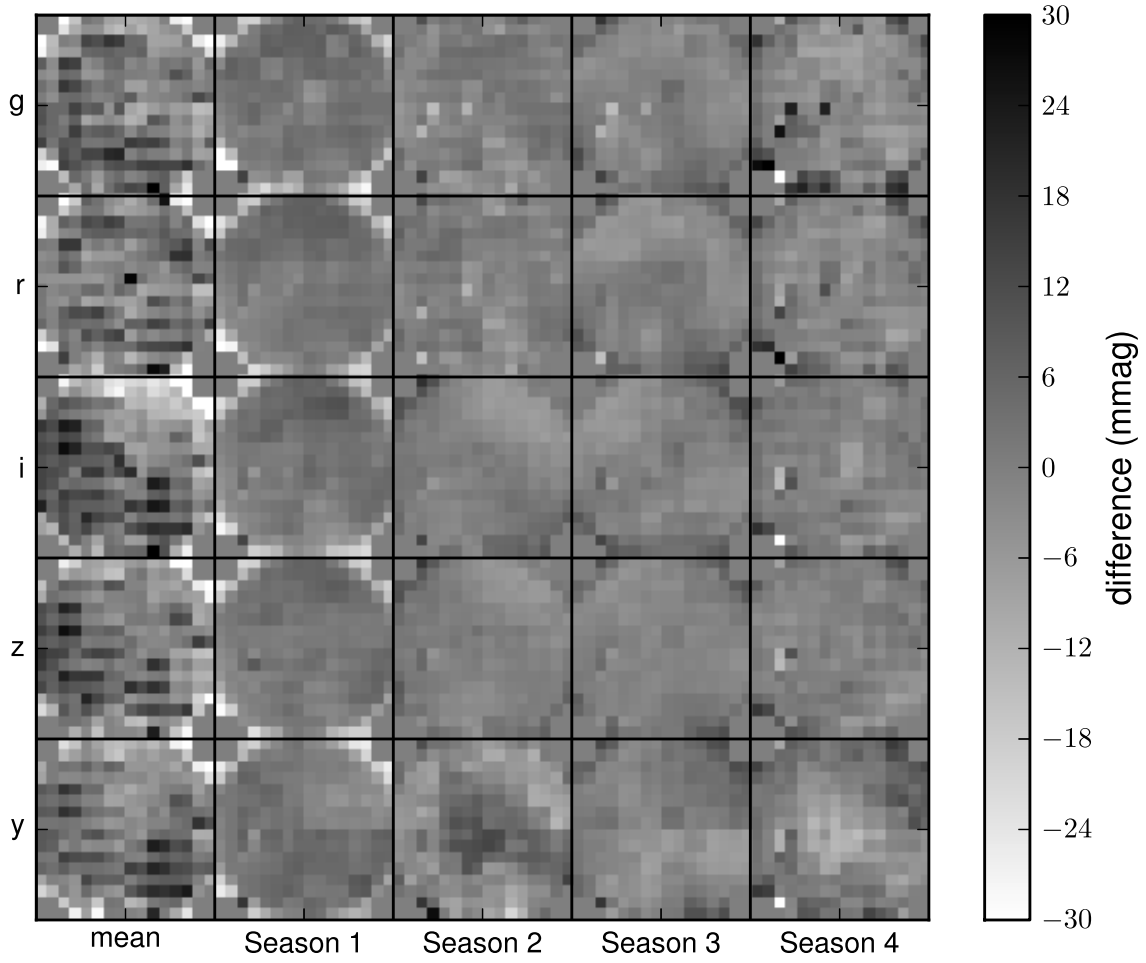

Figure 4.9 The flat fields, in mmag, derived by the photometric calibration, in the $grizy_{\rm P1}$ filters. The first column gives the mean flat field for the survey in each filter, while the later columns give the difference between the flat field for that season (Table 4.1) and the mean flat field. The standard deviation in the mean flat is about 10 mmag, and the mean absolute residual of the difference between this mean flat and four flat seasons is less than 5 mmag, in all of the filters.

4.5 Conclusion

We present the photometric calibration of the first 1.5 years of Pan-STARRS1 survey data. The per-image zero points we measure agree with those computed independently relative to the SDSS with rms scatter of 8.1, 7.1, 9.0, 11.5, and 12.7 mmag in $grizy_{\rm P1}$. This indicates that both surveys have zero points accurate at that

level, when averaged over the 3° field of view of PS1. On smaller scales, photometric nonuniformities over the PS1 field of view and striping in the SDSS start to contribute, but the rms scatter remains only 11, 10, 11, 12, and 16 mmag. We anticipate that as the PS1 survey continues, the accuracy of this calibration will improve as repeat observations reveal slight deviations from the simple photometric model we adopt. Internal tests of the calibration indicate that we may be able to achieve overall image zero point accuracy as good as 5 mmag.

This accuracy renders the photometric calibration a minor source of systematic error in the PS1 photometry. Finkbeiner et al. (2012) has discovered a non-linearity in the PS1 photometry that can bias the photometry of faint sources by a few hundredths when image quality is poor. Likewise, poor image quality in some PS1 images lead to systematics in the PSF magnitudes that dominate the photometric calibration errors.

This photometric calibration demonstrates that 10 mmag calibration accuracy is possible using the survey strategies typical of major upcoming surveys, like the SkyMapper (Keller et al., 2007), the Dark Energy Survey (Flaugher, 2005, DES), the Hyper Suprime-Cam Survey (Takada, 2010, HSC), and the Large Synoptic Survey Telescope (Tyson, 2002, LSST). These surveys operate in a mode much like PS1, repeatedly imaging the sky one filter at a time. This is in contrast to the SDSS, which operated in a drift-scanning mode and nearly-simultaneously imaged the sky in each of its filters. We note, however, that the simultaneous five-color imaging of the SDSS leads to the SDSS having better color accuracy than magnitude accuracy, and that it makes detecting non-photometric weather easier.

The calibration also demonstrates the possibility of photometrically calibrating the $y_{\rm P1}$ band, which includes a strong water vapor absorption feature at about 940 nm. Despite the variability of this feature, we still achieve zero point accuracy of 13 mmag

in this band. This figure may be further improved by including the amount of precipitable water vapor in the air into the calibration. SkyMapper, DES, HSC, and the LSST all also intend to observe in filters including this same feature.

The zero points achieved by this work show that the PS1 system is photometrically stable. Zero points extrapolated to 1.2 airmasses every photometric night have rms scatter of less than 20 mmag in $griz_{\rm P1}$, over the course of the survey. Moreover, these 20 mmag of scatter are dominated by the variability of the atmosphere. The stability of the PS1 optical system and detector is particularly impressive given the continuous improvements to the system over its first 1.5 years of operation, to reduce sky brightness, improve image quality, and defeat camera artifacts.

The level of calibration accuracy we have achieved will enable many PS1 survey goals. The discovery of satellites of the Milky Way, cosmological investigations of supernovae and galaxy clustering, and studies of interstellar reddening all require accurate photometric calibration. When the PS1 data become public, this calibration will provide another benefit to the community: a set of well-calibrated observations of stars covering most of the sky. Together with the absolute calibration of the PS1 data as described in Tonry et al. (in preparation), this work provides an absolutely calibrated set of standard stars over the entire sky north of declination $-30°$, going much fainter than current data sets.

Chapter 5

Future Work: the Three-Dimensional Distribution of the Dust

In this chapter we present work using the calibrated Pan-STARRS1 data of §4 to study the three-dimensional distribution of the dust. This work is currently ongoing and the results of this section are preliminary. However, they showcase the power of Pan-STARRS1 to better understand the Galaxy.

5.1 Introduction

Dust is composed of solid grains of heavy elements in the interstellar medium. The heavy elements are fused in stars from hydrogen and helium and expelled into the interstellar medium in winds and explosions. The dust scatters and absorbs light in the ultraviolet through the infrared, and reemits absorbed starlight in the infrared through microwave. Dust therefore plays an important role in the Galaxy and is pervasive in astronomical measurements.

The spatial distribution of the dust is complicated. In two-dimensional projection, dust clouds are full of complex filamentary, condensed, and evacuated structures. This structure depends on dust and star formation and the dust environment, and is

therefore intimately connected with the physics of the Galaxy. Accordingly, maps of the three-dimensional distribution of the dust would be valuable. Moreover, optical photometric studies of objects in the plane of the Galaxy would be enormously facilitated by such maps.

Nevertheless, the three-dimensional structure of the dust is elusive. The diffuse nature of the dust prevents measuring its distance directly by parallax. The absence of strong, sharp lines in the dust makes studies of the dust distribution through the Galactic rotation curve difficult. We present here a study of the three-dimensional distribution of dust in which we infer the distance to dust clouds through the photometric parallaxes of stars reddened by the dust.

Our objective is to extend the techniques used to study the stellar halo in the SDSS to study the dust and stars in the Galactic disk. The SDSS has performed a number of detailed studies of the halo (Jurić et al., 2008; Belokurov et al., 2006; Bell et al., 2008), but these techniques cannot be applied to the plane because they require reddening estimates to their stars. This is particularly unfortunate given that most of the stars and dust are in the disk.

We solve simultaneously for both the distance and reddening to stars, removing this constraint. The technique used is very similar to that proposed by Sale et al. (2009), Bailer-Jones (2011), and Berry et al. (2011). We apply the technique to data from the Pan-STARRS1 survey. This survey is now in its third year of operation, and has five-band photometry of three quarters of the sky, as well as two-thirds of the Galactic plane, including both the Galactic center and anticenter.

We use this data to map the three-dimensional structure of the dust and stars in the Galactic disk. Section §5.2 presents the Pan-STARRS1 survey, which provides the data used in this work. Section §5.3 presents the technique used to infer the distances and reddenings to individual stars, and our method for inferring the three-dimensional

distribution of dust from these data. Section §5.4 presents the results of our technique as applied to simulated data, to high Galactic latitude stars, to the cloud Monoceros R2, and to a slice through the Galaxy. We are presently working on extending this work to the whole Galaxy observed by Pan-STARRS1. Section §5.5 concludes.

5.2 Data

We study the dust using five-band optical data from Pan-STARRS1. Pan-STARRS1 is a wide-field optical imager that surveys the sky primarily in five bands, $grizy_{\rm P1}$, spanning 4000–10500Å (Kaiser et al., 2010; Chambers, in preparation). The telescope is located on Haleakala in Maui, and routinely delivers arcsecond seeing (Hodapp et al., 2004). Images are recorded by the Gigapixel Camera 1 (Tonry & Onaka, 2009; Onaka et al., 2008), an array of CCDs containing more than a billion pixels.

Pan-STARRS1 images are processed by the Image Processing Pipeline, which automatically performs bias and dark subtraction, flat fielding, astrometry, and photometry (Magnier, 2006; Magnier et al., 2008; Magnier, 2007). The data have been carefully photometrically calibrated, both absolutely and relatively over the survey footprint (Tonry et al., in preparation; Stubbs et al., 2010b; Schlafly et al., 2012).

In this work we are interested in stars observed by Pan-STARRS1, and not galaxies. Accordingly, all objects used here must have AP_MAG − PSF_INST_MAG < 0.1. Because we are ultimately limited in our ability to measure reddening and distance by the difficulty separating variation in stellar type from reddening, we also require that the object be observed in each of the five Pan-STARRS1 bands.

5.3 Methods

Our objective is to measure the distribution of stars and dust in the Galaxy using Pan-STARRS1 data. The process for making these measurements divides naturally into three parts. First, we describe in §5.3.1 the general method by which parameters describing a star can be inferred from that star's photometry. Second, we describe in §5.3.2 how those parameters can be combined to infer the distribution of the dust along a line of sight. Finally, we describe our implementation of this technique for Pan-STARRS1 data in §5.3.3

5.3.1 Inferring the Distance and Reddening to a Star

The broadband colors of a star are almost completely determined by the star's temperature, metallicity, and gravity. Among these, gravity affects colors only slightly. Metallicity, on the other hand, makes a significant impact in the bluer bands, but has little effect on bands redward of about 400 nm. Accordingly, in the Pan-STARRS1 colors, the intrinsic colors of stars lie along a nearly one-dimensional locus, with a star's position on that locus determined by its temperature.

The observed colors of a star depend both on its intrinsic colors and the reddening to the star. Accordingly, the observed Pan-STARRS1 stellar colors lie on a two-dimensional surface. Determining the stellar type and reddening to a star is a matter of finding where on that surface each star lies. Because Pan-STARRS1 provides four independent colors, in principle we can extract the temperature and reddening to each star.

The problem is complicated by the fact that the reddening vector—the direction in color-color space along which dust reddens starlight—is nearly parallel to the stellar locus, the line on which the intrinsic colors of stars fall. Accordingly, the

two-dimensional surface is very skewed and small uncertainty in the colors of a star result in large covariant uncertainties in the star's reddening and stellar type. Nevertheless, by properly treating these uncertainties the reddening and stellar types of stars can be inferred from the star's photometry.

We use a straight-forward Bayesian framework to infer the reddening and distance to stars from their photometry. The technique is essentially the same as that proposed by Sale et al. (2009), Bailer-Jones (2011), and Berry et al. (2011). Specifically, suppose we have measured magnitudes $\mathbf{M}$ for a star, and are interested in inferring some parameters $\mathbf{T}$ describing that star. In the case described above, $\mathbf{T}$ might be the distance, reddening, and stellar type of the star, though more parameters could in principle be inferred. Any particular set of stellar parameters $\mathbf{T}$ imply a set of intrinsic magnitudes $\mathbf{M}_{\rm int}(\mathbf{T})$. The probability of observing the magnitudes $\mathbf{M}$ is then Gaussian

$$P(\mathbf{M}|\mathbf{T}) \propto \exp((\mathbf{M} - \mathbf{M}_{\rm int})^2/\sigma^2) \tag{5.1}$$

where it is assumed that the errors in the magnitudes $\mathbf{M}$ are Gaussian and uncorrelated. We are however interested in the parameters $\mathbf{T}$ given $\mathbf{M}$, which is obtained by Bayes' theorem,

$$P(\mathbf{T}|\mathbf{M}, G) \propto P(\mathbf{M}|\mathbf{T})P(\mathbf{T}|G) \propto \exp((\mathbf{M} - \mathbf{M}_{\rm int})^2/\sigma^2)P(\mathbf{T}|G) \tag{5.2}$$

where we have additionally introduced some prior G on the parameters $\mathbf{T}$. This may include any prior information we have as to the distribution of stars in the Galaxy, for instance.

In this work we are interested foremost in the reddening and distances to stars. This is obtained by marginalizing out all other parameters $\mathbf{T}$ to obtain $P(A, \mu|\mathbf{M}, G)$,

the probability that a given star is seen through reddening A and is at distance modulus μ given its observed magnitudes $\mathbf{M}$ and some prior G.

The primary caveat to this approach is that it ignores the problem of blended and binary stars. In principle we can introduce additional free parameters into the model including these effects, and then marginalize them out of the fit. However, we have not explored that approach here, and instead acknowledge that our fits will fail badly for a small minority of objects.

5.3.2 Inferring the Distribution of Dust

Given only the photometry for a single star, $P(A, \mu|\mathbf{M}, G)$ fully describes our knowledge about its reddening and distance. However, in any direction in the sky, we have observations of many stars. A priori, the distances and stellar types of these stars are unrelated. However, the reddenings to these stars are closely coupled, because if one star is behind another star, light traveling to us from the far star must pass through the dust between the two stars, as well as the dust between us and the near star. Simply, distant stars in a direction must be more reddened than nearby stars. We can also choose to relax this constraint, and require only that stars in the same place be reddened equally. In either case, the reddening to one star informs the reddening to other stars.

We can easily incorporate this requirement into the formalism introduced in §5.3.1. Let the reddening in some direction on the sky be described by some function $A(\mu; \alpha)$, where μ is the distance modulus in that direction and α are some parameters determining A. Then our knowledge of the distribution of dust is given by $P(\alpha|\vec{\mathbf{M}}, G)$, where $\vec{\mathbf{M}}$ includes the measured photometry for all of the stars along a line of sight. Letting $\vec{\mu}$ be a vector of the distance moduli to each of N stars in a

direction, we can rewrite this as

$$P(\alpha|\vec{\mathbf{M}}, G) = \int d^N \vec{\mu} P(\alpha, \vec{\mu}|\vec{\mathbf{M}}, G) \tag{5.3}$$

By Bayes theorem, this is proportional to

$$P(\alpha|\vec{\mathbf{M}}, G) \propto \int d^N \vec{\mu} P(\vec{\mathbf{M}}|\alpha, \vec{\mu}) P(\alpha, \vec{\mu}|G) \tag{5.4}$$

Having specified α and $\vec{\mu}$, we have specified the reddenings to each of the stars, $A(\vec{\mu}; \alpha)$. Accordingly, the factor $P(\vec{\mathbf{M}}|\alpha, \vec{\mu})$ is just the product of $P(\mathbf{M}|A, \mu)$ over each of the stars. If we assume additionally that the dust distribution and distances to the individual stars are all independent of one another, then

$$P(\alpha, \vec{\mu}|G) = P(\alpha|G) \prod_i P(\mu_i|G) \tag{5.5}$$

This means that our knowledge of the dust distribution factors

$$P(\alpha|\vec{\mathbf{M}}, G) \propto P(\alpha|G) \prod_i \int d\mu_i P(\mathbf{M}_i|A(\mu_i, \alpha), \mu_i) P(\mu_i|G) \tag{5.6}$$

so that our knowledge of the dust distribution depends only on $P(\mathbf{M}|A, \mu)P(\mu|G)$ for each star individually. By Bayes' theorem, moreover, that quantity is proportional to $P(A, \mu|\mathbf{M})$, up to a prior on reddening. This is exactly what we computed in §5.3.1.

The point is that the three-dimensional distribution dust along a line of sight is simply related to the estimates of the reddening and distances to individual stars. Moreover, all of the information about the dust distribution can be inferred after $P(A, \mu)$ have been computed for individual stars. Finding the best fit dust distribution then requires only a few parameter fit to each star individually along a

line of sight, and then the resulting fits can be combined to fit the distribution of the dust, making the problem easily tractable.

5.3.3 Details for Pan-STARRS1

We apply the techniques above to Pan-STARRS1 data to infer the reddenings and distances to individual stars, and to infer from these the three-dimensional distribution of the dust. We adopt in this first study a minimal model for individual stars like that of Berry et al. (2011).

This minimal model assumes that the intrinsic colors of stars form a one-parameter family parameterized by the intrinsic stellar $r - i$ color. These colors may be reddened by a dust column described by $E(B - V)$ and a reddening vector R, which we take from Schlafly & Finkbeiner (2011). The star also has some distance modulus μ. We assume, for the moment, that all stars are dwarfs, and we assume also the photometric parallax relation of Jurić et al. (2008), which gives $M_r(r - i)$, the r band absolute magnitude of a star as a function of its $r - i$ color. Then our model for the observed photometry of a star is

$$\mathbf{M} = \mathbf{C}(r - i) + M_r(r - i) + \mathbf{R}E(B - V) + \mu \tag{5.7}$$

where $\mathbf{C}(r - i)$ gives the magnitudes $\mathbf{M}$ for a star with intrinsic color $r - i$ and $\mathbf{M}_r = 0$.

The function $\mathbf{C}(r - i)$ is determined by the shape of the stellar locus. We find the function $\mathbf{C}$ by fitting a spline to the Pan-STARRS1 stellar locus at high-Galactic latitudes. Figure 5.1 shows the stellar locus and the resulting fit.

This model is simple. In addition to ignoring binarity and blending, it ignores the fact that stars have different metallicities and that not all stars are main-sequence

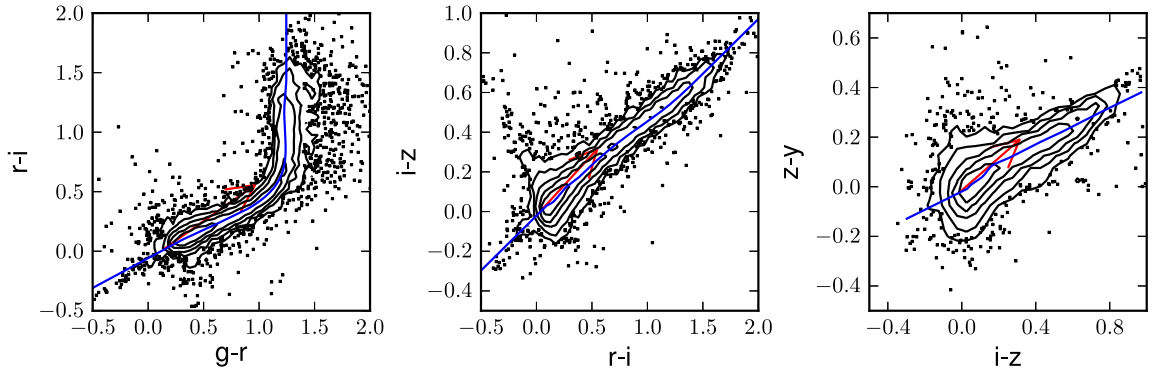

Figure 5.1 The Pan-STARRS1 $grizy_{\rm P1}$ stellar locus for stars within 3 degrees of the North Galactic Pole. Overplotted in blue is our spline fit to the locus. The red arrow gives the affect of $E(B-V)=1$ on a main-sequence star with color $r-i=0$. Note that the reddening vector and the stellar locus are closely aligned.

dwarfs. Accordingly, the derived best fit parameters $r-i$, $E(B-V)$, and μ will occasionally be catastrophically wrong. However, we have found using simulations that this model predicts accurate parameters for most stars (§5.4.1).

That said, our simulations did not include blended stars or binary stars, so those effects have yet to be explored. The insignificant effect of metallicity is easily explained, however. The Pan-STARRS1 survey includes no bands blueward of 4000Å, rendering the observed colors mostly insensitive to metallicity. That said, metal-rich stars of a given temperature are larger and more luminous than metal poor ones, so in principle M_r should depend on both $r-i$ and $[Fe/H]$. Since Pan-STARRS1 has no information about $[Fe/H]$, marginalizing over $[Fe/H]$ amounts to increasing the uncertainty in μ by about 0.15 mags, which we determined by reference to simulation. Because this discussion ignores metallicity gradients in the Galaxy, our distance estimates will be slightly biased. However, as most of the stars of interest are very near the plane we expect this bias to be small.

We ignore in our model the possibility that a star is not on the main-sequence, the same choice made by Berry et al. (2011). This leads to distant giants being modeled

as nearby dwarfs. It is easy, however, to incorporate giants at least roughly into this framework; we need only include another photometric parallax relation $M'_r(r-i)$ for giants.

Because of the simplifying assumptions we have made, we can substantially underestimate the uncertainties in the derived reddening and distance. We add 0.025 magnitudes in quadrature to the uncertainties in the magnitudes estimated from the Pan-STARRS1 pipeline to mitigate this effect.

Armed with Equation 5.7, we compute $P(A, \mu|M)$ for stars observed by Pan-STARRS1. We then use these results to compute $P(\alpha|M)$, describing the distribution of dust in a given direction. For this latter step we need to choose how to parameterize $A(\mu)$. We choose to make $A(\mu)$ piecewise linear. We also optionally require that $A(\mu)$ be an increasing function, reflecting the physical requirement that reddening increase along a line of sight.

We compute $P(A, \mu|M)$ over a surface with $-0.4 < A < 2$ and $5 < \mu < 15$. This fails to capture stars in the most reddened areas. Stars with $E(B-V) > 2$ have 6 magnitudes of g band extinction and start to become rarely detected in g. At present we require a g band detection because the g band photometry is best at breaking the degeneracy between stellar type and reddening. The range of μ encompasses essentially all of the unsaturated dwarfs detected by Pan-STARRS1 in at least four bands. We choose not to use stars detected in only three bands, since then there are no degrees of freedom and our ability to detect poor fits is limited.

5.4 Results

We present here the results from four applications of the technique. First, we show in §5.4.1 that we can recover the reddening and distances of observations of stars in a

simulation. Second, we show in §5.4.2, that, using Pan-STARRS1 data, we can recover the reddening to stars near the North Galactic cap, which we know a priori to be negligibly reddened. Third, we show in §5.4.3 that we can measure the reddening and distances to known dust clouds, recovering the Lombardi et al. (2011) distance to the cloud Monoceros R2. Finally, in §5.4.4 we apply the technique to measure the 3D distribution of dust to a slice through the Galaxy with $b = 5°$.

5.4.1 Simulation

We test our algorithm by using it to recover the reddenings and distances of simulated stars. We simulate observations of the Galaxy using $galfast$, producing simulated photometric stellar catalogs with realistic temperature, metallicity, luminosity, and spatial distributions (Jurić et al., 2008; Juric et al., 2010; Bond et al., 2010; Ivezić et al., 2008). The $galfast$ simulation also includes a mock three-dimensional dust map. We add 20 mmag of photometric noise to the true photometry to simulate observed photometry. We then try to recover the input distances and reddenings to each of the simulated stars.

Figure 5.2 shows the results of this analysis, for stars for which the recovered $P(A, D)$ has only a single mode. These stars account for about half of the stars. The other stars are positioned in color space such that they could plausibly be either intrinsically blue, but reddened stars, or intrinsically red, but unreddened stars. We are able to recover the distances to these stars to within about 25% (top left panel). There is a tendency to underestimate the distance by about seven percent, and the distribution of distance errors is skewed toward large underestimates. This effect comes from assuming that all stars are dwarfs. Stars beginning to turn off the main sequence have slightly underestimated distances, while red giants have catastrophically underestimated distances. The uncertainties in the distances to these

stars are closely recovered, so that χ has a standard deviation of close to one (0.93, lower left panel). The reddening, and the uncertainty in the reddening, are also accurately recovered (right panels). The scatter in the reddening estimates are about 50 mmag per star, and the distribution is Gaussian and unbiased.

We can also try to back out the three-dimensional dust map used in $galfast$. Figure 5.3 shows the result of our fit (§5.3.2) to the three-dimensional distribution of dust in this direction. The grayscale shows the sum of $P(A, D)$ for all of the stars on the sight line, normalized so that each distance bin is assigned the same amount of weight. This illustrates the distribution of $P(A, D)$ for the stars. The purple points show the distances and reddenings to the stars from the simulations. The blue points show the maximum likelihood distances and reddenings to the stars from the fits. The lines show the fits to the three-dimensional distribution of the dust. The blue and red lines are guesses used to compute the green and cyan lines, respectively. The green and cyan line both use §5.3.2 to obtain the three-dimensional dust distribution, with the cyan line incorporating a positivity constraint, and the green line eschewing it. The fits closely match the truth, as indicated by the purple points, over $8 < \mu < 14.5$. At larger distances than this the sample becomes dominated by giants that are mismodeled as dwarfs. At distances with $\mu < 8$, there are few stars, and many stars the fit deems as nearby are in fact giants. Nevertheless, over a broad range of distances the reddening with distance is accurately recovered.

5.4.2 High Galactic Latitudes

We would like to test the technique using actual Pan-STARRS1 data in addition to simulated data. However, because we do not have the true distances and reddenings to large numbers of stars observed by Pan-STARRS1 we cannot repeat §5.4.1 with real data. However, since many parts of the high Galactic latitude sky are essentially

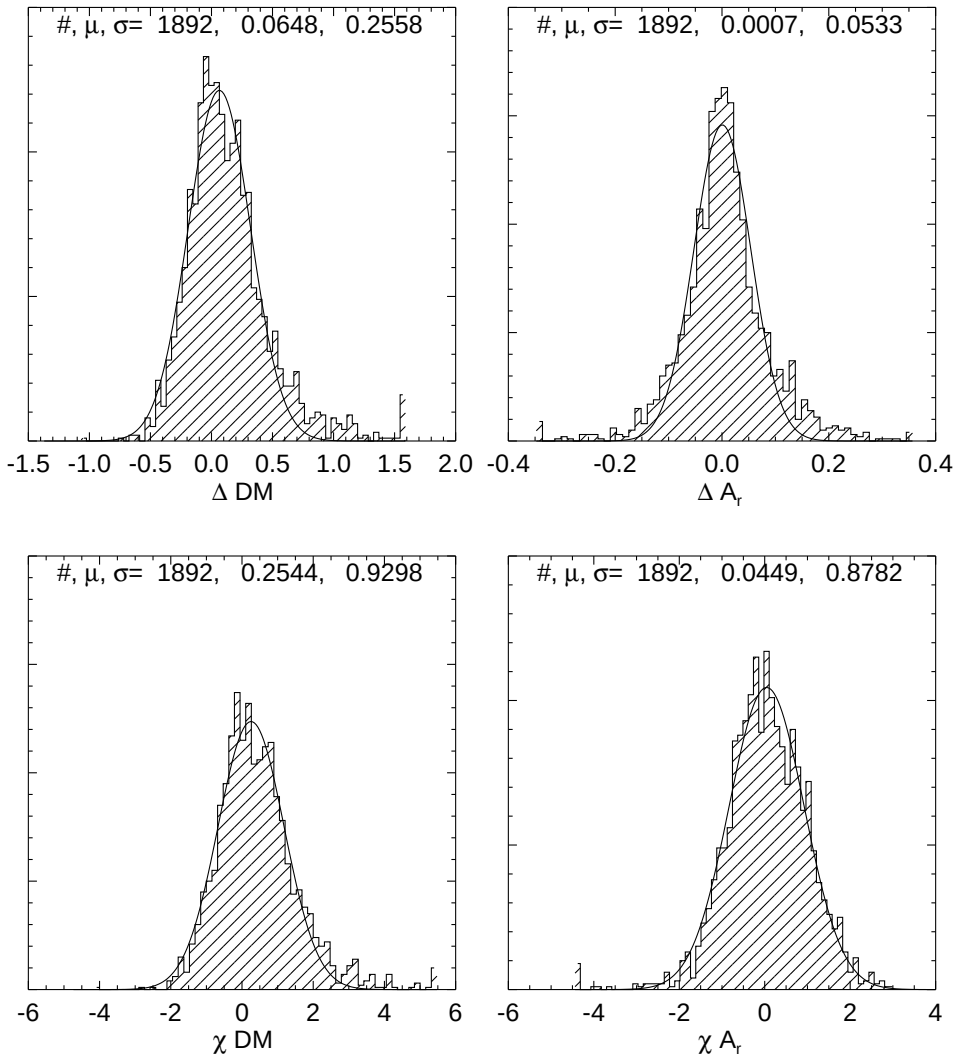

Figure 5.2 We attempt to recover the input reddening and distance modulus to stars generated by *galfast*, using simulated photometry with 20 mmag of uncorrelated Gaussian noise in each band. We show the histograms of the difference between the input and recovered distance modulus (ΔDM) and reddening (ΔA_r), as well as the corresponding quantities scaled by the estimated uncertainties (χDM and χA_r), for stars with only one plausible peak in the fit $P(A, D)$. See §5.4.1 for details.

unreddened, there are many stars for which we have very good reddening estimates, but no distance estimates.

Accordingly we find the estimated reddenings to stars within one degree of the

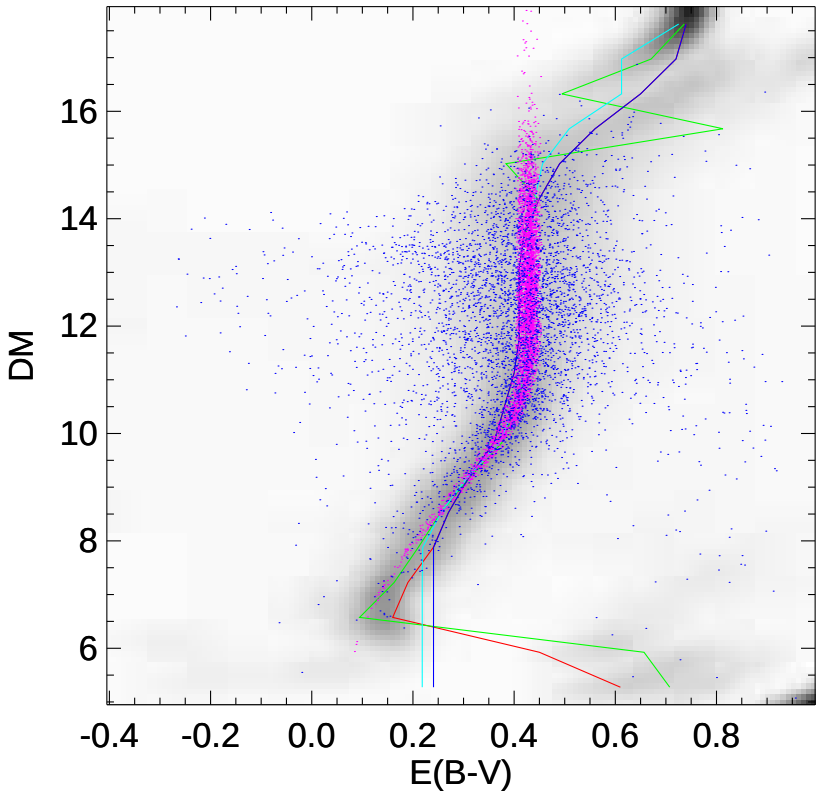

Figure 5.3 Recovering the three-dimensional distribution of dust along a line of sight with simulated data. We recover the input $A(\mu)$ closely, except for $\mu < 8$ and $\mu > 14.5$. For $\mu > 15$, the simulated catalog is dominated by giants, which we do not model. For $\mu < 8$, the few stars are contaminated by distant giants, which are modeled as nearby dwarfs. The purple points give the simulated distances and reddenings, while the blue points give the best fit locations. The cyan line gives the best fit $A(\mu)$ when including a positivity constraint, while the green line give the best fit without this constraint.

North Galactic Pole observed by Pan-STARRS1. The results are shown in Figure 5.4. The top left panel shows the recovered distribution of reddenings $E(B-V)$. The distribution has a mean of 10 mmag, comparable to the SFD-predicted extinction in

this region of about 12 mmag. The standard deviation is 121 mmag. This is substantially larger than the scatter in our simulated data of about 50 mmag. However, because $E(B-V)/\sigma$ has a scatter of about one, this is presumably because of the different distribution of uncertainties going into the observations than went into the simulation, which just used 20 mmag of uncertainty for all stars in all bands. The distribution is approximately Gaussian. In the lower panels we have plotted grayscales illustrating the distribution of $P(A, D)$ for the stars in this direction, as we did for the simulated results in §5.4.1. We have also overplotted the line corresponding to zero reddening. Stars near the North Galactic Pole of most distances are consistently found to have basically zero reddening, as shown in the lower left panel. The lower right panel normalizes the lower left panel so that each bin in distance receives the same amount of ink, highlighting regions where few stars are likely to be found. This panel demonstrates that at the largest distances, stars are expected to be redder than elsewhere. This is because, given observed magnitudes, a more reddened star is intrinsically bluer, and hence more luminous and distant, provided it is on the main sequence. At the largest distances, this wing of $P(A, D)$ is highlighted.

This analysis demonstrates that we can recover the reddening to stars. Because the fitting technique is linear in reddening and has no reason to prefer zero reddening, we can expect the technique to equally well measure the reddening of reddened sources, at least until $E(B-V)$ of a few when observed magnitudes cease to be linear in $E(B-V)$.

5.4.3 Monoceros R2

We can demonstrate that we can measure both reddening and distance, and recover the three-dimensional distribution of dust by analyzing a line of sight through a

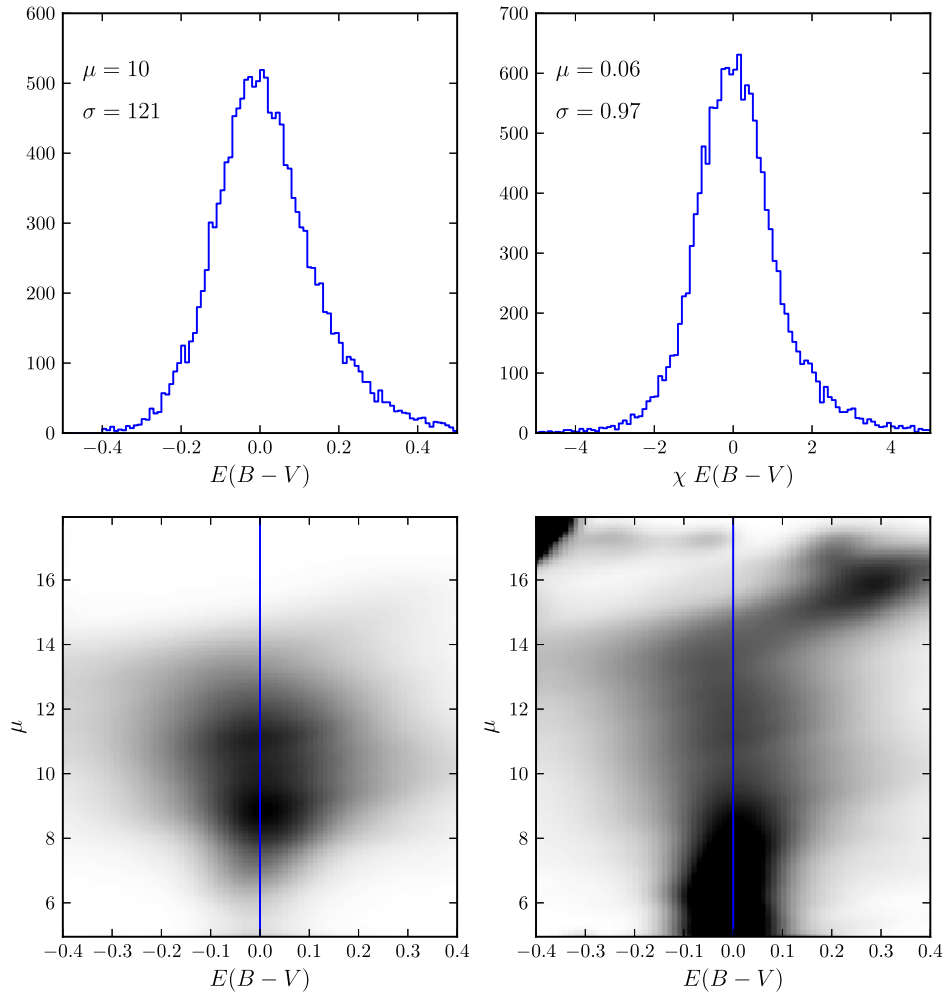

Figure 5.4 The reddening toward observed stars within one degree of the North Galactic Pole. Consistent with SFD, the reddening is about 12 mmag (top left). The scatter is 121 mmag, similar to the expected uncertainties (top right). The lower left panel shows the sum of $P(A, D)$ for each star. The stars at different distances all have reddening about zero (the blue line). The lower right panel repeats the lower left panel, except normalized so that the same amount of ink is used in each distance bin. At large distances, reddening is overestimated, because the given observed magnitudes, reddened stars are bluer, and so are more intrinsically luminous and distant stars.

known dust cloud. Most of the commonly studied dust clouds and star formation regions are very nearby, so that the main-sequence turn-off stars in front of those clouds are saturated in Pan-STARRS1 observations. The Pan-STARRS1 observations

are best suited to clouds at a distance of about 1 kpc. Accordingly, we choose to test our pipeline on the cloud Monoceros R2, which has recently been studied by Lombardi et al. (2011), who report a distance of 905 pc.

We use all of the stars in the neighborhood with $220.5 < l < 221.5$ and $-8.7 < b < -8$, selecting a rectangle around one cloud included in Monoceros R2. We infer the reddenings and distances to these stars. Figure 5.5 shows the results. The top left panel gives the SFD-predicted reddening in the region. The top right panel gives the mean of the best fit reddening for all of the stars in each pixel for our fit. Of course, this mixes stars of different distances together and so provides a biased result—but it at least illustrates that the SFD-predicted reddening and our measured reddenings are highly correlated. White to black ranges from 0 to 1 mag in $E(B-V)$. Overplotted are two red crosses, one at (α, δ) of $(99, -10.8)$ intended to go through the dust cloud, and the other at $(99, -11.3)$ intended to avoid the cloud.

Plots analogous to those in Figures 5.3 and 5.4 are shown in the bottom panels, illustrating the distribution of $P(A, D)$ for the stars within 0.1° of the off-cloud direction (bottom left) and 0.2° of the on-cloud direction (bottom right). The distance to the cloud from Lombardi et al. (2011) is also overplotted as a horizontal line. The blue line gives the mean of the $P(A, D)$ in each distance bin, while the green line gives the fit result of § 5.3.2. In the off-cloud region (bottom left panel), there is no sign of a feature at the distance to the cloud, though the reddening does increase somewhat from μ of 8 to 14, perhaps due to a more diffuse component of the Galactic dust. In the on cloud region, however, there is a sharp increase in the amount of dust at the distance to the cloud (bottom right panel). The distance of the cloud, moreover, is correctly identified by the fit, as shown by the marked increase of the green line where it intersections the horizontal line from Lombardi et al. (2011). A few giants are visible as a highly reddened group of stars identified as more nearby

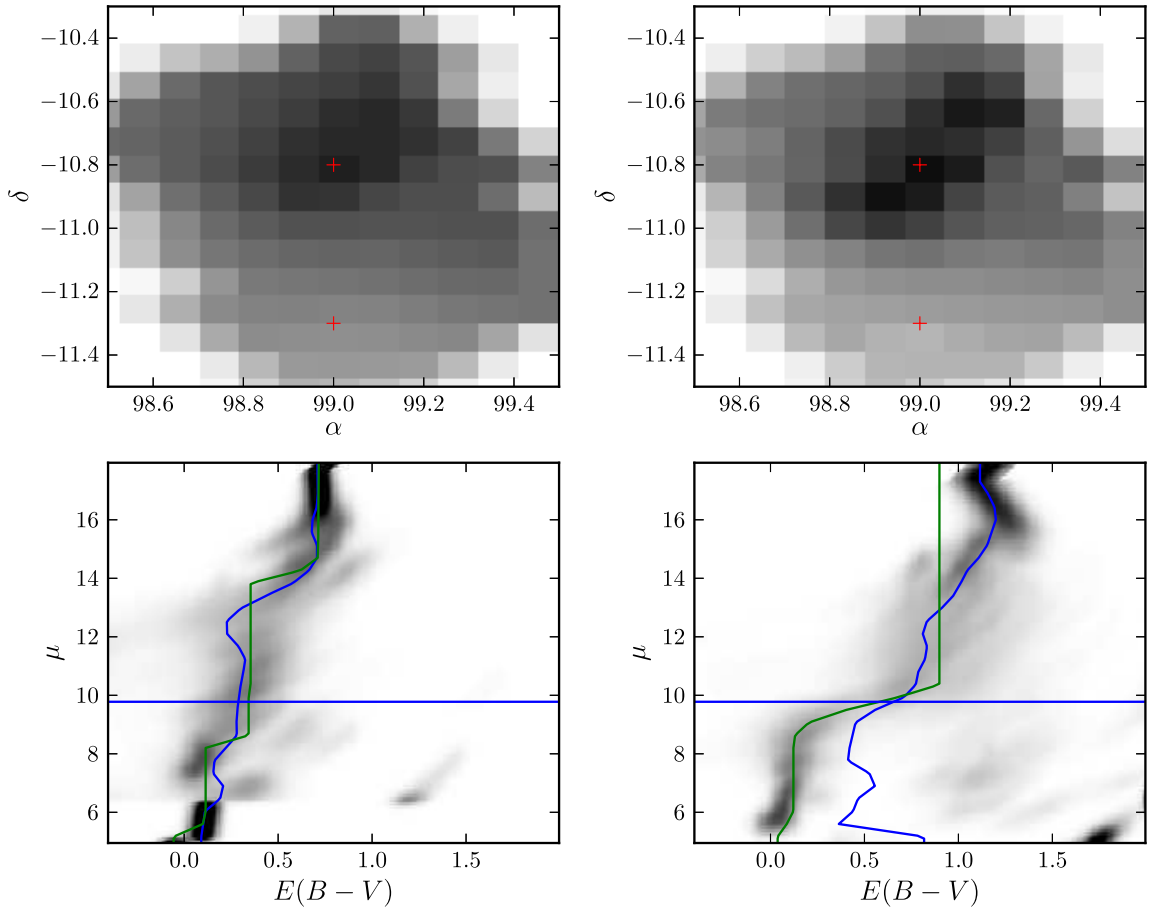

Figure 5.5 The reddening toward the cloud Monoceros R2. The top left panel shows the SFD reddening prediction in this direction, with color scale going from $E(B-V)$ of 0 to 1 (black). The top right panel shows the average reddening for stars in each pixel from our fits. Two directions are highlighted by red crosses: an "on cloud" direction at (α, δ) of $(99, -10.8)$ and an "off cloud" direction of $(99, -11.3)$. The lower left plot shows the resulting three dimensional dust fits for the "off cloud" region, with a grayscale as in Figure 5.4. The blue line gives the weighted average of the reddening in each distance bin, while the green line gives the results of the fit described in §5.3.2. The bottom right panel is the analogous plot for the "on cloud" region. The horizontal blue line shows the distance to the cloud from Lombardi et al. (2011), and is well recovered.

than the cloud by the fit.

This result is heartening because it shows that we can recover the distances to known clouds. Moreover, the technique used to measure the distance here is

completely different from that used by Lombardi et al. (2011). In that work, Lombardi et al. (2011) take advantage of the large reddening through Monoceros R2 to reliably separate stars in front of the cloud from stars behind the cloud on the basis of their colors. They then use the areal number density of foreground stars in concert with the predictions of a Galactic model to infer the distance to the cloud. Here we infer the distance to the cloud through the photometric distances to stars behind and in front of the cloud. The agreement of these independent techniques gives further weight to the result.

5.4.4 The Galactic Plane

We have shown that we can accurately recover the reddening to stars using a high Galactic latitude sample of stars for which we can assume the reddening is small and near the SFD prediction. We have further shown that we can reproduce the known distance to the dust cloud Monoceros R2. We now use this technique to study a narrow slice through the Galaxy, from $l = 90^\circ$ to $l = 270^\circ$ and $4.95^\circ < b < 5.05^\circ$. We repeat the analysis of §5.4.3, except fitting all of the stars in this region. We further fit the $A(\mu)$ for all stars in 0.1° by 0.1° pixels in Galactic latitude and longitude. The result is a two-dimensional slice through the Galaxy analogous to the longitude-velocity diagrams used to study the H I in the interstellar medium. Figure 5.6 shows the longitude-distance extinction map we obtain.

The top panel of Figure 5.6 shows the inferred $E(B-V)$ to each pixel in longitude and distance modulus space. Black to white spans 2 mags $E(B-V)$. We show the results of the fits for which we enforce the requirement that $E(B-V)$ increase along a line of sight. As required, the top panel shows that at each Galactic longitude, the extinction increases as the distance modulus increases. In many directions dust clouds are immediately apparent as sudden increases in extinction at a specific

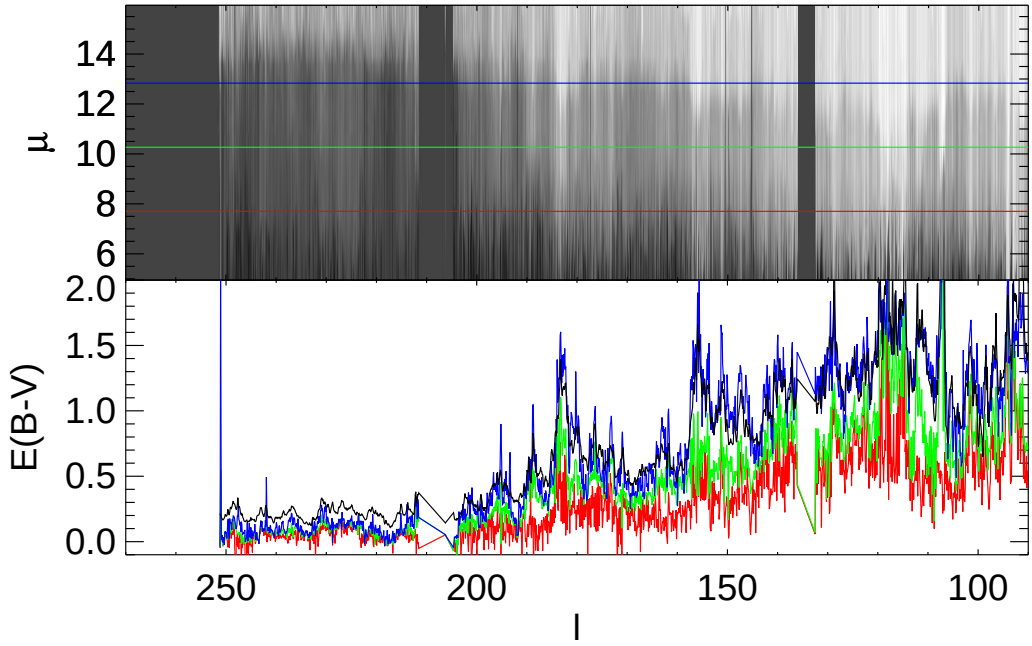

Figure 5.6 A cross section of the Galactic Plane in extinction. The top panel gives the extinction with Galactic latitude and distance modulus μ. White corresponds to an $E(B-V)$ of 2 mags, while black implies no dust. Pixels are 0.1° wide in Galactic longitude and latitude. The data here come from a 0.1° high ring from $l = 270°$ to $l = 90°$ at $b = 5°$. In the lower panel we have plotted the extinction as a function of l for three distance slices, as marked by the horizontal lines in the upper panel. The black line gives the SFD prediction. SFD is seen to closely track the extinction at 3.7 kpc (blue line). Areas where insufficient Pan-STARRS1 data are available are shown in black.

distance modulus. Among these, the cloud at $l = 107°$ is perhaps the most striking. For $\mu < 10$, $E(B-V)$ is about 0.4 mags in this direction, but for $\mu > 10$, $E(B-V)$ jumps suddenly to greater than 2 mags. This sudden jump is moreover consistent between several adjacent, independent pixels. The bottom panel of Figure 5.6 shows $E(B-V)$ at three different distances, which have been indicated on the top panel with horizontal lines. We have also plotted in the lower panel the reddening from SFD with a solid black line. SFD confirms that, indeed, at $l = 107°$ there is a cloud, and the SFD predicted reddening and our predicted reddening at $\mu \approx 13$ closely agree.

Another immediately salient feature of Figure 5.6 is the "ridge" at $\mu \approx 13$, where, beyond which, along all sight lines, the reddening suddenly increases. While we are tempted to associate this feature with spiral arms, the more likely explanation is that the feature is related to our overpredicting the reddening of distant stars (§5.4.2). At high Galactic latitudes we start to run out of stars at around $\mu = 14$. The ridge moves to closer μ in dustier regions, presumably because the extinction from dust shifts the completeness limit to more nearby stars. We are actively trying to better understand the provenance of this feature.

5.5 Conclusion

We have shown that we can recover the reddening for individual stars to within about 0.1 mag on average using Pan-STARRS1 data. We have further shown that at least in simulations we can recover distances to about 25% accuracy. We have demonstrated that we can use these estimates reproduce the accepted distance to the cloud Monoceros R2. Finally, we find that the dust column we estimate at 3.7 kpc closely tracks the SFD-predicted dust column over a long slice through the Galactic plane. Unsurprisingly, the dust column to nearby stars is dramatically smaller than that predicted by SFD. We have mapped the extinction in a slice through the Galaxy, and the resulting map clearly shows a number of clouds for which we can measure distances.

This is convincing evidence that we are able to map the three-dimensional structure of dust in the Galaxy. We are preparing to apply this technique to the entire sky observed by Pan-STARRS1, to produce a wide-field three-dimensional map of the dust in the Galaxy.

The resulting maps will have broad applications. They will allow us to better

understand the distribution of dust in the Galaxy and its relation to the Galactic H I. The clumpiness of the dust may inform models for Galaxy and star formation and stellar feedback. The maps will also enable more accurate correction for dust in the Galactic plane, and will open the Galactic plane to new optical studies of the distribution of stars in the Galaxy.

Chapter 6

Conclusion

Dust research has a bright future. Upcoming photometric surveys like DES, LSST, and Euclid will continue to demand ever improved dust maps. Likewise, further improving the accuracy of supernova cosmology will demand a better understanding of the dust reddening law.

Dust will also remain critical to understanding the physics of the Galaxy. Simulations of the Galactic interstellar medium are now beginning to be able to capture the complex filimentary and bubbly structure that qualitatively matches observations.

The work presented here provides a foundation for enabling both these avenues of research. Our detailed study of the two-dimensional, high Galactic latitude reddening law in the SDSS serves as a large, accurate library of reddening measurements against which improved reddening laws and reddening maps may be tested. These maps will be enabled not only by photometric surveys like Pan-STARRS1, but also by data from Planck, WISE, and AKARI (The Planck Collaboration, 2006; Wright et al., 2010; Murakami et al., 2007). These satellites provide a high-resolution view of dust emission over a broad range of frequencies, far surpassing the data used to construct the SFD dust map. However, calibrating these data into maps of dust extinction will

require high quality extinction measurements like those we provide.

Similarly, our work on revealing the three-dimensional structure of the Galactic dust will enable comparison between the Galactic H I and the dust, informing the chemistry of the Galaxy and the processes that shape the interstellar medium. It will allow for improved comparison between models of the Galactic interstellar medium and data, potentially shedding light on star formation and feedback. More generally, the maps will open a new window onto a large part of our Galaxy. The new three-dimensional maps will also enable more accurate estimates of the reddening and distance to the nearby objects in the Galaxy.

For these reasons, we look forward to continuing developments in dust research for the forseeable future.

6.1 Acknowledgements

D.F. and E.S. acknowledge support of NASA grant NNX10AD69G for this research. M.J. acknowledges support by NASA through Hubble Fellowship grant #HF-51255.01-A awarded by the Space Telescope Science Institute, which is operated by the Association of Universities for Research in Astronomy, Inc., for NASA, under contract NAS 5-26555. Ž.I. acknowledges support by NSF grant AST 07-07901, and Ž.I. and R.G. acknowledge support by NSF grant AST 05-51161 to LSST for design and development activity. NFM acknowledges funding by Sonderforschungsbereich SFB 881 "The Milky Way System" (subproject A3) of the German Research Foundation (DFG).

Funding for SDSS-III has been provided by the Alfred P. Sloan Foundation, the Participating Institutions, the National Science Foundation, and the U.S. Department of Energy. The SDSS-III web site is http://www.sdss3.org/.

SDSS-III is managed by the Astrophysical Research Consortium for the Participating Institutions of the SDSS-III Collaboration including the University of Arizona, the Brazilian Participation Group, Brookhaven National Laboratory, University of Cambridge, University of Florida, the French Participation Group, the German Participation Group, the Instituto de Astrofisica de Canarias, the Michigan State/Notre Dame/JINA Participation Group, Johns Hopkins University, Lawrence Berkeley National Laboratory, Max Planck Institute for Astrophysics, New Mexico State University, New York University, Ohio State University, Pennsylvania State University, University of Portsmouth, Princeton University, the Spanish Participation Group, University of Tokyo, University of Utah, Vanderbilt University, University of Virginia, University of Washington, and Yale University.

The Pan-STARRS1 Survey has been made possible through contributions of the Institute for Astronomy, the University of Hawaii, the Pan-STARRS Project Office, the Max-Planck Society and its participating institutes, the Max Planck Institute for Astronomy, Heidelberg and the Max Planck Institute for Extraterrestrial Physics, Garching, The Johns Hopkins University, Durham University, the University of Edinburgh, Queen's University Belfast, the Harvard-Smithsonian Center for Astrophysics, and the Las Cumbres Observatory Global Telescope Network, Incorporated, the National Central University of Taiwan, and the National Aeronautics and Space Administration under Grant No. NNX08AR22G issued through the Planetary Science Division of the NASA Science Mission Directorate.

References

Abazajian, K., Adelman-McCarthy, J. K., Agüeros, M. A., et al. 2004, AJ, 128, 502

Abazajian, K. N., Adelman-McCarthy, J. K., Agüeros, M. A., et al. 2009, ApJS, 182, 543

Aihara, H., Allende Prieto, C., An, D., et al. 2011, ApJS, 193, 29

Allende Prieto, C., Sivarani, T., Beers, T. C., et al. 2008, AJ, 136, 2070

Amôres, E. B., & Lépine, J. R. D. 2005, AJ, 130, 659

Arce, H. G., & Goodman, A. A. 1999, ApJ, 512, L135

Bailer-Jones, C. A. L. 2011, MNRAS, 411, 435

Barnard, E. E. 1919, ApJ, 49, 1

Bell, E. F., Zucker, D. B., Belokurov, V., et al. 2008, ApJ, 680, 295

Belokurov, V., Zucker, D. B., Evans, N. W., et al. 2006, ApJ, 642, L137

Berry, M., Ivezić, Ž., Sesar, B., et al. 2011, ArXiv e-prints

Blake, C. H., & Shaw, M. M. 2011, ArXiv e-prints

Boggess, N. W., Mather, J. C., Weiss, R., et al. 1992, ApJ, 397, 420

Bond, N. A., Ivezić, Ž., Sesar, B., et al. 2010, ApJ, 716, 1

Burke, D. L., Axelrod, T., Blondin, S., et al. 2010, ApJ, 720, 811

Burstein, D., & Heiles, C. 1978, ApJ, 225, 40

Cambrésy, L., Boulanger, F., Lagache, G., & Stepnik, B. 2001, A&A, 375, 999

Cardelli, J. A., Clayton, G. C., & Mathis, J. S. 1989, ApJ, 345, 245

Castelli, F., & Kurucz, R. L. 2004, ArXiv Astrophysics e-prints

Chambers, K. C. in preparation

Chen, B., Figueras, F., Torra, J., et al. 1999, A&A, 352, 459

Dobashi, K., Uehara, H., Kandori, R., et al. 2005, PASJ, 57, 1

Doi, M., Tanaka, M., Fukugita, M., et al. 2010, ArXiv e-prints

Draine, B. T. 2003, ARA&A, 41, 241

—. 2009, ArXiv e-prints

—. 2011, Physics of the Interstellar and Intergalactic Medium (Princeton University Press)

Draine, B. T., & Lazarian, A. 1998, ApJ, 508, 157

Eddington, A. S. 1926, Royal Society of London Proceedings Series A, 111, 424

Edvardsson, B. 2008, Physica Scripta Volume T, 133, 014011

Faber, S. M., Wegner, G., Burstein, D., et al. 1989, ApJS, 69, 763

Finkbeiner, D. P., Davis, M., & Schlegel, D. J. 1999, ApJ, 524, 867

Finkbeiner, D. P., Magnier, E. A., Schlafly, E. F., & Jurić, M. 2012

Fitzpatrick, E. L. 1999, PASP, 111, 63

Fitzpatrick, E. L., & Massa, D. 2005, AJ, 129, 1642

Flaugher, B. 2005, International Journal of Modern Physics A, 20, 3121

Fong, R., Hale-Sutton, D., & Shanks, T. 1992, MNRAS, 257, 650

Fong, R., Metcalfe, N., & Shanks, T. 1994, in IAU Symposium, Vol. 161, Astronomy from Wide-Field Imaging, ed. H. T. MacGillivray, 295–+

Fukugita, M., Ichikawa, T., Gunn, J. E., et al. 1996, AJ, 111, 1748

Glazebrook, K., Peacock, J. A., Collins, C. A., & Miller, L. 1994, MNRAS, 266, 65

Gunn, J. E., Carr, M., Rockosi, C., et al. 1998, AJ, 116, 3040

Gustafsson, B., Edvardsson, B., Eriksson, K., et al. 2008, A&A, 486, 951

Herschel, W. 1785, Royal Society of London Philosophical Transactions Series I, 75, 213

High, F. W., Stubbs, C. W., Rest, A., Stalder, B., & Challis, P. 2009, ArXiv e-prints

Hodapp, K. W., Kaiser, N., Aussel, H., et al. 2004, Astronomische Nachrichten, 325, 636

Hogg, D. W., Finkbeiner, D. P., Schlegel, D. J., & Gunn, J. E. 2001, AJ, 122, 2129

Honeycutt, R. K. 1992, PASP, 104, 435

Ivezić, Ž., Lupton, R. H., Schlegel, D., et al. 2004, Astronomische Nachrichten, 325, 583

Ivezić, Ž., Sesar, B., Jurić, M., et al. 2008, ApJ, 684, 287

Jones, D. O., West, A. A., & Foster, J. B. 2011, ArXiv e-prints

Jurić, M. in preparation

Juric, M., Cosic, K., Vinkovic, D., & Ivezic, Z. 2010, in Bulletin of the American Astronomical Society, Vol. 42, American Astronomical Society Meeting Abstracts #215, #401.25

Jurić, M., Ivezić, Ž., Brooks, A., et al. 2008, ApJ, 673, 864

Kaiser, N., Aussel, H., Burke, B. E., et al. 2002, in Society of Photo-Optical Instrumentation Engineers (SPIE) Conference Series, Vol. 4836, Society of Photo-Optical Instrumentation Engineers (SPIE) Conference Series, ed. J. A. Tyson & S. Wolff, 154–164

Kaiser, N., Burgett, W., Chambers, K., et al. 2010, in Society of Photo-Optical Instrumentation Engineers (SPIE) Conference Series, Vol. 7733, Society of Photo-Optical Instrumentation Engineers (SPIE) Conference Series

Kalberla, P. M. W., & Kerp, J. 2009, ARA&A, 47, 27

Keller, S. C., Schmidt, B. P., Bessell, M. S., et al. 2007, PASA, 24, 1

Kurucz, R. 1993, ATLAS9 Stellar Atmosphere Programs and 2 km/s grid. Kurucz CD-ROM No. 13. Cambridge, Mass.: Smithsonian Astrophysical Observatory, 1993., 13

Lee, Y. S., Beers, T. C., Sivarani, T., et al. 2008a, AJ, 136, 2022

—. 2008b, AJ, 136, 2050

Li, A., & Greenberg, J. M. 2003, in Solid State Astrochemistry, ed. V. Pirronello, J. Krelowski, & G. Manicò, 37–84

Lombardi, M., Alves, J., & Lada, C. J. 2011, A&A, 535, A16

Maddox, S. J., Efstathiou, G., & Sutherland, W. J. 1990, MNRAS, 246, 433

Magnier, E. 2006, in The Advanced Maui Optical and Space Surveillance Technologies Conference

Magnier, E. 2007, in Astronomical Society of the Pacific Conference Series, Vol. 364, The Future of Photometric, Spectrophotometric and Polarimetric Standardization, ed. C. Sterken, 153–+

Magnier, E. A., Lewin, W. H. G., van Paradijs, J., et al. 1992, A&AS, 96, 379

Magnier, E. A., Liu, M., Monet, D. G., & Chambers, K. C. 2008, in IAU Symposium, Vol. 248, IAU Symposium, ed. W. J. Jin, I. Platais, & M. A. C. Perryman, 553–559

Ménard, B., Scranton, R., Fukugita, M., & Richards, G. 2010, MNRAS, 405, 1025

Munari, U., Sordo, R., Castelli, F., & Zwitter, T. 2005, A&A, 442, 1127

Murakami, H., Baba, H., Barthel, P., et al. 2007, PASJ, 59, 369

Neugebauer, G., Habing, H. J., van Duinen, R., et al. 1984, ApJ, 278, L1

Newberg, H. J., Yanny, B., Rockosi, C., et al. 2002, ApJ, 569, 245

O'Donnell, J. E. 1994, ApJ, 422, 158

Oke, J. B., & Gunn, J. E. 1983, ApJ, 266, 713

Onaka, P., Tonry, J. L., Isani, S., et al. 2008, in Society of Photo-Optical Instrumentation Engineers (SPIE) Conference Series, Vol. 7014, Society of Photo-Optical Instrumentation Engineers (SPIE) Conference Series

Padmanabhan, N., Schlegel, D. J., Finkbeiner, D. P., et al. 2008, ApJ, 674, 1217

Peek, J. E. G., & Graves, G. J. 2010, ArXiv e-prints

Pirronello, V., Manicó, G., Roser, J., & Vidali, G. 2004, in Astronomical Society of the Pacific Conference Series, Vol. 309, Astrophysics of Dust, ed. A. N. Witt, G. C. Clayton, & B. T. Draine, 529

Plez, B. 2008, Physica Scripta Volume T, 133, 014003

Re Fiorentin, P., Bailer-Jones, C. A. L., Lee, Y. S., et al. 2007, A&A, 467, 1373

Ross, A. J., Ho, S., Cuesta, A. J., et al. 2011, ArXiv e-prints

Rowles, J., & Froebrich, D. 2009, MNRAS, 395, 1640

Rudnick, J. 1936, ApJ, 83, 394

Sale, S. E., Drew, J. E., Unruh, Y. C., et al. 2009, MNRAS, 392, 497

Schlafly, E. F., & Finkbeiner, D. P. 2011, ApJ, 737, 103

Schlafly, E. F., Finkbeiner, D. P., Schlegel, D. J., et al. 2010, ApJ, 725, 1175

Schlafly, E. F., Finkbeiner, D. P., Juric, M., et al. 2012, ArXiv e-prints

Schlegel, D. J., Finkbeiner, D. P., & Davis, M. 1998, ApJ, 500, 525

Skrutskie, M. F., Cutri, R. M., Stiening, R., et al. 2006, AJ, 131, 1163

Smolinski, J. P., Lee, Y. S., Beers, T. C., et al. 2010, ArXiv e-prints

Stanek, K. Z. 1998, ArXiv Astrophysics e-prints

Stubbs, C. W., Doherty, P., Cramer, C., et al. 2010a, ArXiv e-prints

—. 2010b, ApJS, 191, 376

Stubbs, C. W., High, F. W., George, M. R., et al. 2007, PASP, 119, 1163

Su, D. Q., Cui, X., Wang, Y., & Yao, Z. 1998, in Society of Photo-Optical Instrumentation Engineers (SPIE) Conference Series, Vol. 3352, Society of Photo-Optical Instrumentation Engineers (SPIE) Conference Series, ed. L. M. Stepp, 76–90

Takada, M. 2010, in American Institute of Physics Conference Series, Vol. 1279, American Institute of Physics Conference Series, ed. N. Kawai & S. Nagataki, 120–127

The Planck Collaboration. 2006, ArXiv Astrophysics e-prints

Tonry, J., & Onaka, P. 2009, in Advanced Maui Optical and Space Surveillance Technologies Conference,

Tonry, J. L., Stubbs, C. W., Lykke, K. R., et al. in preparation

Trumpler, R. J. 1930, PASP, 42, 214

Tyson, J. A. 2002, in Society of Photo-Optical Instrumentation Engineers (SPIE) Conference Series, Vol. 4836, Society of Photo-Optical Instrumentation Engineers (SPIE) Conference Series, ed. J. A. Tyson & S. Wolff, 10–20

Wakker, B., Howk, C., Schwarz, U., et al. 1996, ApJ, 473, 834

Weinberg, D. H., Beers, T., Blanton, M., et al. 2007, in Bulletin of the American Astronomical Society, Vol. 38, Bulletin of the American Astronomical Society, 963–+

Wolf, M. 1923, Astronomische Nachrichten, 219, 109

Wright, E. L., Eisenhardt, P. R. M., Mainzer, A. K., et al. 2010, AJ, 140, 1868

Yanny, B., Rockosi, C., Newberg, H. J., et al. 2009, AJ, 137, 4377

Yasuda, N., Fukugita, M., & Schneider, D. P. 2007, AJ, 134, 698

York, D. G., Adelman, J., Anderson, Jr., J. E., et al. 2000, AJ, 120, 1579